

1-1-2014

Using Large-Angle Beamstrahlung To Detect And Diagnose Colliding Beams For Luminosity Optimization

Hussein Farhat
Wayne State University,

Follow this and additional works at: http://digitalcommons.wayne.edu/oa_dissertations

Recommended Citation

Farhat, Hussein, "Using Large-Angle Beamstrahlung To Detect And Diagnose Colliding Beams For Luminosity Optimization" (2014).
Wayne State University Dissertations. Paper 1047.

This Open Access Dissertation is brought to you for free and open access by DigitalCommons@WayneState. It has been accepted for inclusion in Wayne State University Dissertations by an authorized administrator of DigitalCommons@WayneState.

**USING LARGE-ANGLE BEAMSTRAHLUNG TO DETECT AND DIAGNOSE
COLLIDING BEAMS FOR LUMINOSITY OPTIMIZATION**

by

HUSSEIN A. FARHAT

DISSERTATION

Submitted to the Graduate School

of Wayne State University,

Detroit, Michigan

in partial fulfillment of the requirements

for the degree of

DOCTOR OF PHILOSOPHY

2014

MAJOR: PHYSICS

Approved by:

Advisor

Date

ACKNOWLEDGEMENTS

I would like to thank my advisor Professor Giovanni Bonvicini for teaching me principles of High Energy Physics during the four years of my PhD courses. Additionally, I greatly appreciate his support during my whole research program and his efforts in editing my thesis. I would also like to thank Ryan Gillard for being such a good friend and colleague to work with step by step throughout the whole research process. In addition, I would like to thank all of my family members for supporting and celebrating this moment in heart. Lastly, a big thank to my wife for her patience and for staying by my side the whole time.

TABLE OF CONTENTS

Acknowledgments.....	ii
List of Tables.....	vi
List of Figures	vii
Chapter 1 : Introduction.....	1
1.1 The Standard Model.....	1
1.2 Elementary Particles.....	1
1.2.1 Elementary Fermions.....	2
1.2.2 Bosons	4
1.3 Weak Interaction and the CKM Matrix	5
Chapter 2 Belle II Experiment and Beamstrahlung.....	10
2.1 Introduction.....	10
2.2 Beam Accelerators	10
2.3 The KEKB and SuperKEKB	11
2.3.1 SuperKEKB Upgrades.....	13
2.3.2 LINAC of the SuperKEKB	15
2.4 Storage Rings.....	18
2.5 Luminosity	22
2.6 The Belle II detector	23
2.7 Large Angle Beamstrahlung	25
Chapter 3 : Designing the Beamstrahlung Detector.....	29
3.1 An overview on the large beamstrahlung detector:	29
3.2 Beam pipe and its components.....	31
3.3 Before Primary Elbow	32
3.4 Primary Elbow: Purpose, Components Design, and Production.....	34
3.4.1 The Primary Mirror	36
3.4.2 The 45 ⁰ Mounting Adapter:	37
3.4.3 Mirror Mount and Its Studs:	38
3.4.4 Square Brass Rods:	39
3.4.5 Stepper Motors and Their Mount:	40
3.4.6 Circular Window:	42
3.4.7 Back Plate:	42
3.4.8 Primary Elbows Production and Hardware:	43

3.5 Piping	44
3.6 Manual Elbows Design, Production, Sandblasting and Anodizing	44
3.7 Optics Box.....	47
3.7.1 Wollaston Prisms.....	48
3.7.2 Ruled Diffraction Gratings	50
3.7.3 Optical Benches.....	52
3.7.4 Light Collectors Motivation, Design, and Failure	54
3.7.5 Prisms-Lenses system:.....	55
3.7.6 Conveyor belt and its stepper motor.....	61
3.7.7 Photomultipliers Definition and Applications	62
3.7.8 Electronics and Back plate	63
3.8 The Old Electronics Setup.....	64
3.9 Anodized Aluminum Box	66
Chapter 4 : Tests and results.....	67
4.1 Introduction.....	67
4.2 Optics Box Composites Testing	67
4.3 Wollaston Prisms	69
4.4 Elliptical Flat Mirrors	74
4.1 Ruled Diffraction Gratings	79
4.2 Light Collectors.....	80
4.3 Prisms-Lenses Arrays.....	82
4.4 PMTS Testing and Calibrations	84
4.5 Conveyor belt tests and controls:	89
4.6 Primary Elbow Control.....	91
4.7 Wiring	92
4.8 Electronics Cards	93
4.9 Aligning Manual Elbows and Mirrors Adjustments	93
4.10 Wollaston Prism alignment	95
4.11 Polarization Tests.....	97
4.12 Mirrors and Grating Alignments	98
Chapter 5 : Conclusion	102
References	103
Abstract.....	104

Autobiographical Statement.....105

LIST OF TABLES

Table 1: Machine Parameters of SuperKEKB and KEKB	15
Table 2: Beamstrahlung Detector Parameters.....	26
Table 3: Beamstrahlung Parameters.	27
Table 4: Eight Light Collectors and Their Corresponding Bandwidths	55
Table 5: Various Prisms Angles vs. Different Angles of Incidence	58
Table 6: Total Transmitted Coefficient of All Prisms-Lenses.....	60
Table 7: Measured Angle Spread of Four Wollaston Prisms at Different Wavelengths ..	70
Table 8: A Wollaston Efficiency Behavior vs. Polarization and Frequency	73
Table 9: Two Wollaston Average Efficiencies vs. Frequency	74
Table 10: Efficiencies of Multiple Elliptical Mirrors Using Three Different Sources	77
Table 11: Two Identical 600grooves/mm Gratings Efficiencies	80
Table 12: Polarized Prisms Efficiencies within the Expected Light Cone	83
Table 13: Experimental Coefficients vs. Theoretical	83
Table 14: Twelve Necessary Programs to Interchange PMTs Locations	90

LIST OF FIGURES

Figure 1.1: Fundamental Particles of the Standard Model	2
Figure 1.2: Interaction of the Standard Model.....	5
Figure 1.3: Weak Decay Mechanism of Fermions in the Standard Model.....	6
Figure 1.4: Hadronic Cross Section in the Υ Mass Region as a Function of Energy	9
Figure 2.1: Aerial Picture of KEKB	11
Figure 2.2: Diagram of the Future SuperKEKB	12
Figure 2.3: New Beam Pipe	13
Figure 2.4: New Beam Pipe at the Interaction Region	14
Figure 2.5: LINAC of the KEKB.....	16
Figure 2.6: Operational Principle of RF Cavities	16
Figure 2.7: Beam Kicker Schematic	18
Figure 2.8: SuperKEKB Dipole Magnet.....	19
Figure 2.9: Left: Quadrupole Magnet Oriented at 45deg, Right: Magnetic Field Lines ..	20
Figure 2.10: Quadrupole Focusing Principles	20
Figure 2.11: LEFT A Sextupole Design, Right: Magnetic Lines of a Sextupole	21
Figure 2.12: Electrons-Positrons Beams at KEKB (Left) and SuperKEKB (Right)	22
Figure 2.13: The Belle Detector.....	24
Figure 2.14: Normalized beamstrahlung Powers vs. the Collisions Types	28
Figure 3.1: Schematic of the Beamstrahlung Detector That Will Be Used at BELLE II.	29
Figure 3.2: LABM Light Extraction Element in the Beam Pipe.	32
Figure 3.3: The Front Adaptor Tube That Connects Primary Elbow to the Beam Pipe adapter.....	32

Figure 3.4: Primary Elbow Top Adaptor (left), Aluminum Tube (middle).....	33
Figure 3.5: The Primary Elbow to Beam Pipe Connector	33
Figure 3.6: L-R Diffuser and LED Strip at the Center of Adapter Tube	34
Figure 3.7: Primary Elbow Design and Its Constituents.....	36
Figure 3.8: An Elliptical Primary Mirror and Its Mounting Disk.....	37
Figure 3.9: 45deg Aluminum Adapter (left) With the Mirror (right)	38
Figure 3.10: Mirror Mount Schematics	38
Figure 3.11: Mirror's Mount Connection to the Primary Elbow	39
Figure 3.12: Square Brass Rods Schematics.....	40
Figure 3.13: 12V-2A Electric Motor Design.	41
Figure 3.14: Mounting the Motors on Their Mount inside Primary Elbow.....	41
Figure 3.15: A Primary Elbow and Its Circular Window to Viewing the Brass Rods	42
Figure 3.16: Back Plate That Covers a Primary Elbow and Allows Motors Wiring.....	43
Figure 3.17: Primary Elbow.....	43
Figure 3.18: A 12V Driver Used to Control a Stepper Motor	44
Figure 3.19: Back, Front cover, and Two Different Adapter Tubes That Can be	45
Figure 3.20: An Elliptical Flat Mirror on a Mount inside a Manual Elbow Reflecting Light.....	46
Figure 3.21: A Sandblasted Manual Elbow (Left), A Black Anodized Finished Elbow (Right).....	47
Figure 3.22: The Optics Box and Its Constituents, Side View.	47
Figure 3.23: Front View of Optical Box.....	48
Figure 3.24: Wollaston Prism Splitting One Beam into Two Orthogonally Polarized Beams.....	49
Figure 3.25: In This Optics Box Side View Wollaston Are Symmetrically Installed.....	49

Figure 3.26: Ruled Diffraction Grating Schematic and Angle Definition.....	50
Figure 3.27: Efficiency Curves for Ruled Gratings at Various Wavelengths.....	51
Figure 3.28: Left: 600 Grooves/mm Ruled Diffraction Grating Design, Right: Photo of Gratings/Mount Assembly.	52
Figure 3.29: Elliptical Mirror Mount.....	53
Figure 3.30: Half Optical Bench Schematics.....	54
Figure 3.31: A Light Collector from Side (Left) and Front (Right) Views	55
Figure 3.32: Light Path through a Prism-Lens Optical System	56
Figure 3.33: Array of 8 Prisms-Lenses Collection Mounted in Their Frames and Facing PMTs.....	61
Figure 3.34: Front and Side Views of Conveyor Belt Carrying 16 PMTs	62
Figure 3.35: Photomultiplier and Photoelectric Effect Principle.....	63
Figure 3.36: Design of the Back Panel.	64
Figure 3.37: High Voltage Sockets (Left) and Rails (Right) on the Back Plate.....	64
Figure 3.38: Electronic setup	65
Figure 3.39: Anodized Assembled Optics Box Containing All Optical Components.....	66
Figure 4.1: Setup Used to Test Optical Components Using Three Different Sources of Light.....	67
Figure 4.2: Reflected and Transmitted Powers of Two Daughter Beams at Different Frequencies as a Function of one Polarizer's Angle.....	69
Figure 4.3: Wollaston Prism's Characterization Setup.....	69
Figure 4.4: Beam Angular Deviation by Wollaston Prism vs. Wavelength	71
Figure 4.5: Schematic of Measuring Incoming (Upper) and Output Beams (Bottom)	72
Figure 4.6: Wollaston Average Efficiency as a Function of Wavelength.	73
Figure 4.7: Elliptical Mirror's Efficiency vs. Incidence Angle	75

Figure 4.8: Polarized Efficiency of an Elliptical Mirror as a Function of Wavelength....	76
Figure 4.9: Elliptical Mirror Average Efficiency	77
Figure 4.10: Grating Efficiency Curves for Both Polarizations.	79
Figure 4.11: Efficiency of a Light Collector vs. Incidence Angle	81
Figure 4.12: Light Paths inside a Light Collector at an Angle of 15 degree	82
Figure 4.13: Prisms Efficiencies at Different Wavelengths.....	83
Figure 4.14: Wood Prototype Detector Built in 2010.....	85
Figure 4.15: PMTs Counts at Different High Voltages and Different Thresholds.....	87
Figure 4.16: Spectral Responses of Four Different PMTs vs. High Voltage	89
Figure 4.17: Two Ways of Connecting Pipes and Elbows in an Optical Channel.	94
Figure 4.18: Laser Alignment Intermediate Step.....	94
Figure 4.19: Next Step in Alignment Procedure.....	95
Figure 4.20: Two Views of a Plumb Line Used to Align a Wollaston.....	96
Figure 4.21: Left: Purple Laser Spots on a Plumb Line inside the Optics Box. Right: Green Laser Spots on a Plumb Line inside the Optics Box.	96
Figure 4.22: Green-Red Different Polarized Incoming Beams Striking a Wollaston	97
Figure 4.23: Combination of Three Different Sources Schematic	99
Figure 4.24: White-Like Laser's Separation through the Wollaston	100
Figure 4.25: Simulated Optimized Positions and Angles Orientations of Multiple Elements of Optics Box.....	101

Chapter 1 : Introduction

1.1 The Standard Model

It is believed that the universe we now know was contained in a very dense single particle that exploded 14 billion years ago and expanded out to form all subatomic particles known as protons, electrons, and neutrons. After a short time, these particles interacted with each other to form atoms, matter, stars, galaxies, and all what we see around us while the universe keeps expanding out and cooling down.

Physicists believe that even subatomic particles have many fundamental particles which, in a way or another, interact together to constitute subatomic particles. Therefore, they suggested a model or a theory that studies all interaction types including weak, electromagnetic, and strong nuclear interactions. This theory was developed throughout the years since 1960 starting with the quark model [1] until 2012 completed with the observation of the Higgs bosons; such a model is called the Standard Model.

The Standard Model is then a mathematical theory representing all particle interactions into groups called unitary groups as follows. The electromagnetic and the weak force are represented by a $SU(2) \times U(1)$ theory called Quantum Electrodynamics (QED) [2][3][4]. The strong nuclear force, however, is represented by the gauge group $SU(3)$ called Quantum Chromodynamics (QCD) [5][6].

1.2 Elementary Particles

The Standard Model includes elementary or fundamental particles that can be described as point-like particles and are the basics of any formation of other particles.

They are classified into two different groups according to their spins: fermions and bosons as shown in Figure 1.1.

			Fermions			Bosons	
mass →	$\approx 2.3 \text{ MeV}/c^2$	$\approx 1.275 \text{ GeV}/c^2$	$\approx 173.07 \text{ GeV}/c^2$	0	$\approx 126 \text{ GeV}/c^2$		
charge →	2/3	2/3	2/3	0	0		
spin →	1/2	1/2	1/2	1	0		
	u up	c charm	t top	g gluon	H Higgs boson		
QUARKS	$\approx 4.8 \text{ MeV}/c^2$	$\approx 95 \text{ MeV}/c^2$	$\approx 4.18 \text{ GeV}/c^2$	0			
	-1/3	-1/3	-1/3	0			
	1/2	1/2	1/2	1			
	d down	s strange	b bottom	γ photon			
	$0.511 \text{ MeV}/c^2$	$105.7 \text{ MeV}/c^2$	$1.777 \text{ GeV}/c^2$	0			
	-1	-1	-1	1			
	1/2	1/2	1/2	0			
	e electron	μ muon	τ tau	Z Z boson			
LEPTONS	$< 2.2 \text{ eV}/c^2$	$< 0.17 \text{ MeV}/c^2$	$< 15.5 \text{ MeV}/c^2$	± 1			
	0	0	0	1			
	1/2	1/2	1/2	0			
	ν_e electron neutrino	ν_μ muon neutrino	ν_τ tau neutrino	W W boson			
					GAUGE BOSONS		

Figure 1.1: Fundamental Particles of the Standard Model

1.2.1 Elementary Fermions

This blog of particles represents all fermions being arranged in a matrix of 3×4 . The former number indicates the number of the generations; the latter is for the charge type of elementary fermions in the Standard Model.

- The first generation includes up (u), down (d) quarks, leptons like the electron (e), and its related neutrino (ν_e). Such a generation contains the lightest fermions.

- The second generation includes charm (c), strong (s) quarks, leptons like the muon (μ), and its related neutrino (ν_μ). Fermions of this generation are relatively heavier than those of the first generation.
- The last type includes top (t), bottom (b) quarks, leptons like tauon (τ), and its related neutrino (ν_τ). Fermions of this generation are the heaviest.

In addition, fermions are grouped in such a way that all first row quarks have the same charge fraction of $+\frac{2}{3}e$ with an up isospin. However, others in the second row have a charge fraction of $-\frac{1}{3}e$ with a down isospin. All quarks carry quantum numbers that are not shown in the table called colors or flavor mainly red, blue, and green. Another important property quarks have is that each quark has an antiparticle called anti-quark and represented by the corresponding anti-color. For example, an up quark (u) having a red color has an antiparticle having the same mass and spin of (u) and can be represented by (\bar{u}) and carrying anti-red flavor.

Likewise, leptons in the same row have the same electronic charge, but unlike quarks they are colorless and carry an integer charge value of (e^-); all third row leptons carry a net charge of (-1). Leptons in the last row are massless and carry no net charge. Like quarks, leptons have their corresponding antiparticles having the same mass but opposite net charge. As an example, the antiparticle of the electron is called positron and represented by e^+ . Since neutrinos are neutral, their antiparticles can be represented by the bar on top of the neutrino particle (ν_μ and $\bar{\nu}_\mu$).

Finally, a plethora of sub particles such as Baryons and Mesons would be produced when a quark gets mixed with its antiquark or another quark type. When a quark is mixed

with an antiquark, they form what is called a meson which absolutely depends on the quarks type, thus a charm meson, a bottom meson, etc... can be formed. In our case, for instance, an admixture of (b, \bar{b}) produces a B-meson where all of its properties can be searched and studied at accelerators and colliders working at the energy field of B-meson mass energy and basing on smashing electrons and positrons.

1.2.2 Bosons

The second category of elementary particles shown in Figure 1.1 is bosons. Bosons interact with other particles including fermions, leptons, and even themselves to exhibit all kinds of interactions including the weak, strong, and electromagnetic forces. They are also divided into two different sorts: gauge bosons (red) and Higgs bosons (yellow).

Each gauge boson has an integer spin of 1. Some of them are like photons and gluons and are massless; others like Z and W bosons have masses, but they are not as massive as the Higgs boson. Not all bosons are neutral and have no antiparticles, but W^+ represents the W-boson particle and W^- represents the antiparticle. These bosons are the source of the electroweak force.

A Higgs boson is a massive but spineless boson that is believed to be responsible for the mass of other particles excluding photons and gluons because it mediates the electroweak force when it interacts with charged particles, and the weak force when interacts with uncharged particles. On the contrary, massless bosons like photons mediate the electromagnetic force and those like gluons mediate the strong force.

Interaction types between all fundamental particles of the Standard Model can be shown in Figure 1.2.

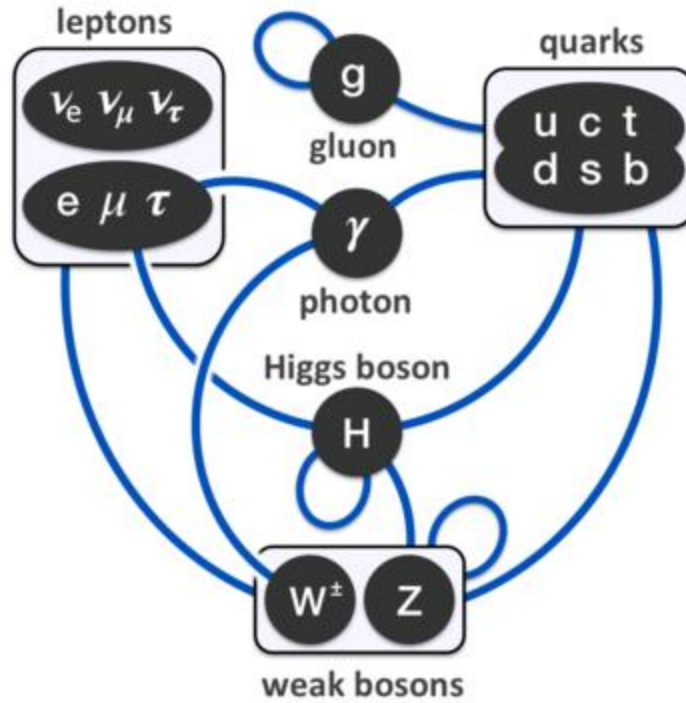


Figure 1.2: Interaction of the Standard Model

1.3 Weak Interaction and the CKM Matrix

According to the Standard Model, fermions of the same generation interact with themselves, their antiparticles, and with particles and antiparticles from other generations as long as charge conservation is preserved. Moreover, all generations of fermions can be always produced out of each other, for example decaying from the up to the down quarks through absorption of a W^- , or a W^+ when decaying from a down to an up quark. The diagram below (Fig 1.3) shows the Feynman diagram for a weak decay.

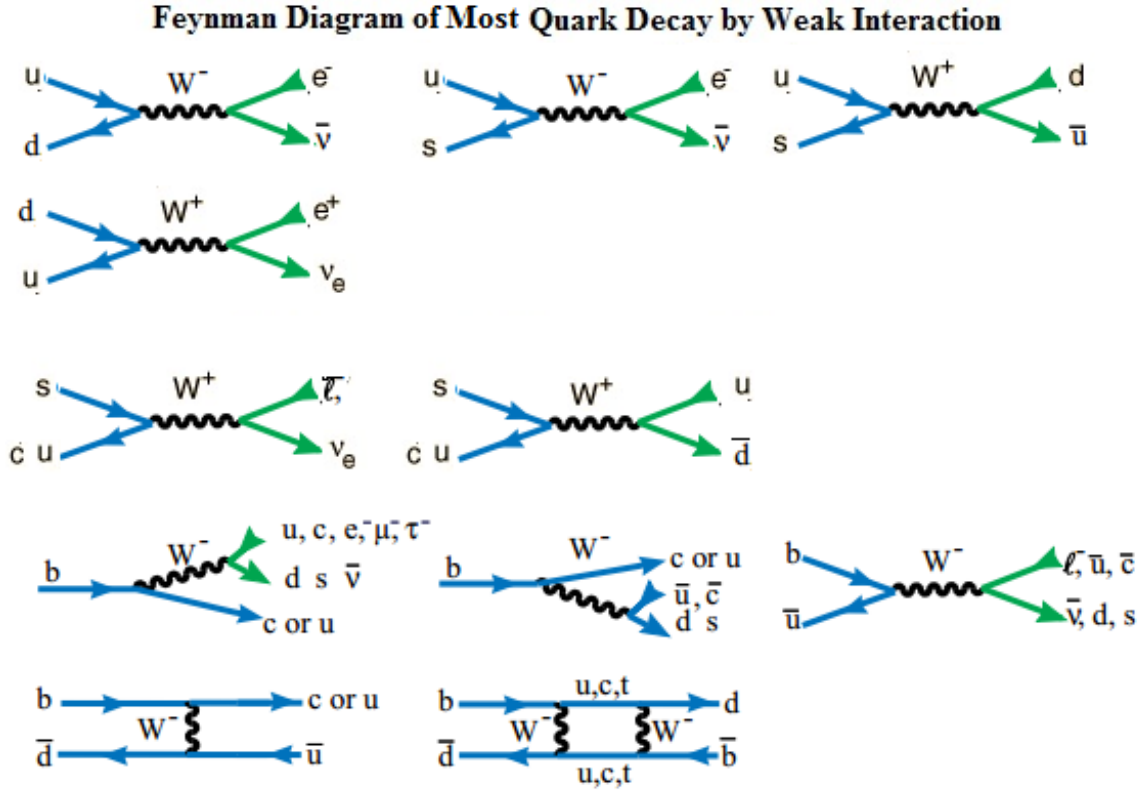


Figure 1.3: Weak Decay Mechanism of Fermions in the Standard Model

As shown in Figure 1.3, a quark decaying weakly does not simply decay into a quark of its own generation, but it will, with certain probabilities, couple to all quark generations. The Cabibbo-Kobayashi-Maskawa (CKM) matrix [7] describes the amplitude mixing. It states that weak eigenstates (d', s', b') are rotated with respect to the mass eigenstates (d, s, b). The CKM matrix is a unitary matrix 3×3 elements, each element providing the transition probability of a quark mass eigenstate i to another mass quark eigenstate j as shown below:

$$\begin{pmatrix} d' \\ s' \\ b' \end{pmatrix} = \begin{bmatrix} V_{ud} & V_{us} & V_{ub} \\ V_{cd} & V_{cs} & V_{cb} \\ V_{td} & V_{ts} & V_{tb} \end{bmatrix} \begin{pmatrix} d \\ s \\ b \end{pmatrix} \quad (1.1)$$

The $|V_{ij}|^2$ term represents the probability that the quark j decays to another quark i ; i and j can represent any quark. Unlike a 2×2 matrix, where each element has to be real up to an overall phase, it allows complex matrix elements, which can be represented in terms of the Wolfenstein parameters A , λ , ρ , and η [8], as follows:

$$V_{CKM} = \begin{bmatrix} 1 - \frac{\lambda^2}{2} & \lambda & A\lambda^3(\rho - i\eta) \\ -\lambda & 1 - \frac{\lambda^2}{2} & A\lambda^2 \\ A\lambda^3(1 - \rho - i\eta) & -A\lambda^2 & 1 \end{bmatrix} \quad (1.2)$$

Where i represents the complex value of $\sqrt{-1}$. The V_{ub} term is one of those which include an irreducible phase ($\rho - i\eta$) which is responsible for the sole known CP (charge parity) violating interaction in nature, and as such it holds great interest. The experimentally measured CKM elements magnitudes are [9][10]:

$$V_{CKM} = \begin{bmatrix} 0.97427 \pm 0.00015 & 0.22534 \pm 0.00065 & 0.00351^{+0.00015}_{-0.00014} \\ 0.22520 \pm 0.00065 & 0.97344 \pm 0.00016 & 0.0412^{+0.0011}_{-0.0005} \\ 0.00867^{+0.00029}_{-0.00031} & 0.0404^{+0.0011}_{-0.0005} & 0.999146^{+0.000021}_{-0.000046} \end{bmatrix} \quad (1.3)$$

In the case of a B-meson decaying to lighter particles, one can see that $|V_{ub}|^2 = 1.2 \times 10^{-5}$. Therefore, CP-violating effects are small and require a great number of events to be studied in detail.

If one desires to observe one event of this kind, given a perfect detector, the number of events N_{ev} should obviously be in the order of 10^5 . In practice, events of interest are detected with efficiencies ranging from 10^{-1} to 10^{-2} . Assuming that these phenomena be studied in detail, a 1% precision requires 10^4 events or more. With a simple calculation, one would obtain a total number of events of order:

$$N \sim 10^5 \times 10^2 \times 10^4 = 10^{11} \text{ events.}$$

In particle physics, the number of events, cross section (σ), and the luminosity L , which is defined as the overlapping of two colliding beams over space and time, are all connected as shown in Eq. (1.4):

$$\frac{dN_{ev}}{dt} = L\sigma \quad (1.4)$$

In the case of the Upsilon (4S), the cross section is about 1nb or $1 \times 10^{-33} \text{ cm}^2$ as shown in Figure 1.5 (the picture shows only four out of six cross section resonances that have been discovered so far). Using Eq. (1.4), one would integrate over time and eventually obtain the total number of events:

$$N_{ev} = \int L\sigma dt \quad (1.5)$$

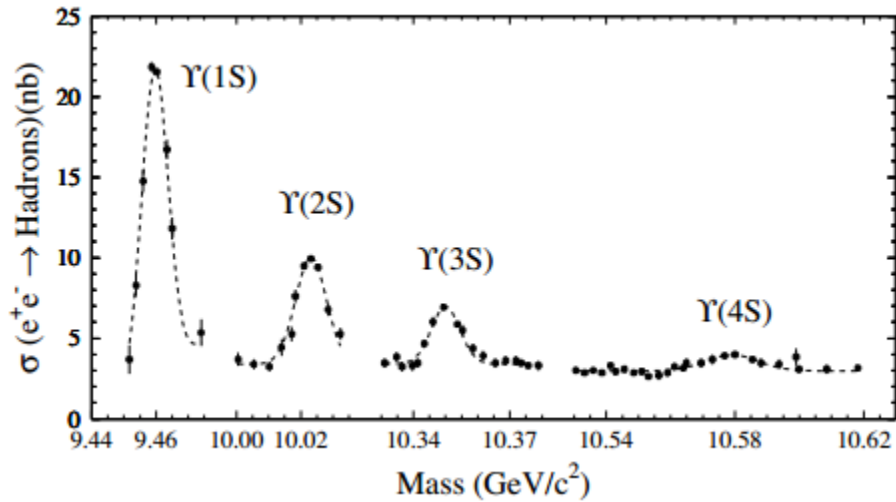


Figure 1.4: Hadronic Cross Section in the Υ Mass Region as a Function of Energy

If we want a number of events of 10^{11} in a ten years time period, the integrated luminosity can be found to be about (one machine year is only 10^7 seconds, as the machine does not run all the time):

$$L = \frac{N_{ev}}{\sigma T} = \frac{10^{11}}{10^{-33} \times 10 \times 10^7} = 10^{36} \text{cm}^{-2} \text{s}^{-1} \quad (1.6)$$

As a result, a new luminosity, higher than the $2.1 \times 10^{34} \text{cm}^{-2} \text{s}^{-1}$ obtained at KEKB, is expected to be obtained by building a new kind of accelerator working at the Upsilon (4S). This new B-factory is called the SuperKEKB and will be discussed in the next chapter.

Chapter 2 Belle II Experiment and Beamstrahlung

2.1 Introduction

As mentioned in the previous chapter, the physical properties of particles and the way they interact can be searched and studied at accelerators and colliders.

Some particle accelerators like SuperKEKB are based on a common concept which consists of accelerating a charged particle or an antiparticle (electron or positron) using electric and magnetic fields. They can be linear or circular, and they range from MeV to TeV kinetic energy according to the scientific fields that are designed to be used in.

On the other hand, colliders as their names suggest, are built to simply collide particles together which can be done in two different ways: fixed target colliders where an accelerated beam of particles strikes a stationary target, and beam-beam colliders where two beams of particles are accelerated in opposite directions in order to collide and eventually lead to the production and discovery of new particles.

2.2 Beam Accelerators

An accelerator can be thought of as an ensemble of multiple parts performing different tasks. Some of the tasks performed in an accelerator consist of generating, separating, forming, and accelerating beams of electrons and positrons. When parts are linearly arranged, the accelerator is called a LINAC; if they are arranged in an approximate circular ring, the accelerator is called a circular or ring accelerator.

We ask the following questions: how can particles be produced, what are the tools needed to separate and accelerate particles, and how can a bunch of particles be grouped

together? More than that, one could ask about specific details like what energy do particles have, what phenomena affect their stable orbits inside the beam pipe and what will happen after the beams collide?

2.3 The KEKB and SuperKEKB

One of the two original asymmetric colliders studying B-meson physics was the KEKB accelerator in Tsukuba, Japan. SuperKEKB is being built in the same tunnel to improve on the research done at KEKB, starting in 1999. The laboratory name is KEK, and its layout is shown in Figure 2.1.



Figure 2.1: Aerial Picture of KEKB

KEK stands for the High Energy Accelerator Research Organization. It conducts numerous experiments, including the Belle experiment at KEKB. The Belle collaboration

comprises more than 500 physicists and engineers from universities around the globe including Wayne State University.

KEKB consisted of two rings of a circumference of 3016 meters each and located underground at a depth of 10 meters. Both KEBK and SuperKEKB operate according to a similar scheme, but SuperKEKB has numerous upgrades to produce and maintain smaller beams, and cope with larger beam currents. The SuperKEKB schematic is shown in Figure 2.2.

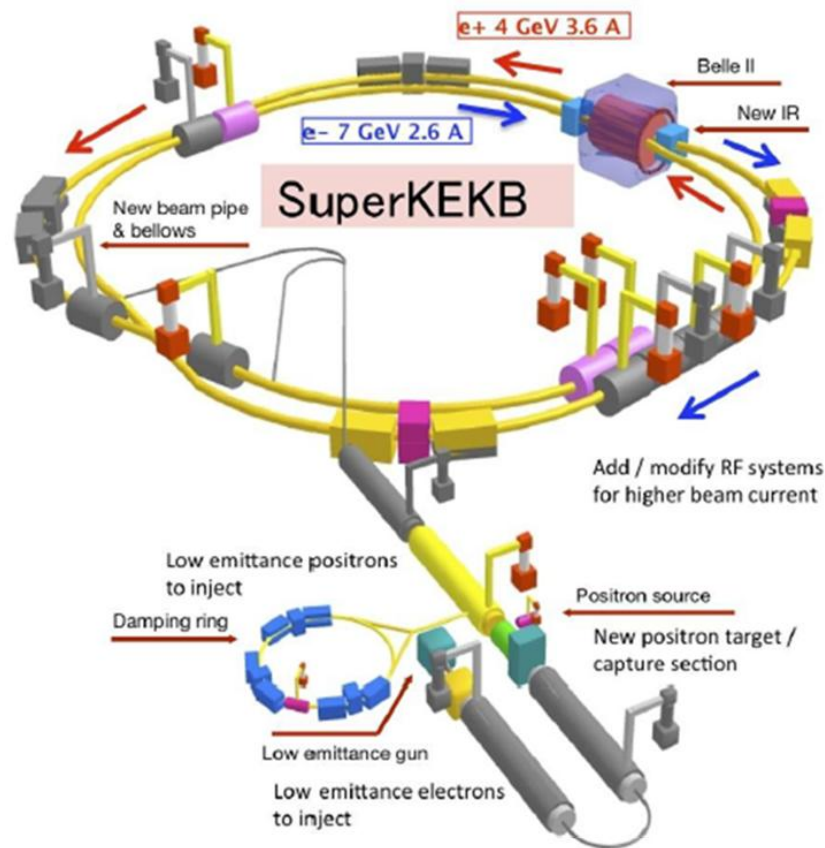


Figure 2.2: Diagram of the Future SuperKEKB

The two beam pipes are housed in the same tunnel, side by side. The two synchrotron rings are called High Energy Ring (HER) enclosing the high energy particles (electrons),

and Low Energy Ring (LER) enclosing the low energy particles (positrons). There is one place at the SuperKEKB where the two pipes intersect and the two beams collide, called the Interaction Region (IR), and surrounded by the Belle II detector. KEKB and SuperKEKB produce B-mesons at center-of-mass-energy in the Upsilon Υ ($4S$) mass region, which is an ideal energy for observation of rare events because the B-mesons are produced nearly at rest.

2.3.1 SuperKEKB Upgrades

SuperKEKB is the updated version of KEKB which means not all parts get the upgrades but only those critical for luminosity improvement.

In regard to the beam pipes, their inner surfaces will be coated with a thin layer of Titanium Nitride which helps in degassing the pipe and reducing all residual gas inside the pipes. Additionally, large antechambers are added to the arcs to help absorb X-rays from synchrotron radiation (SR), and to have larger area gas capture elements (Figure 2.3).

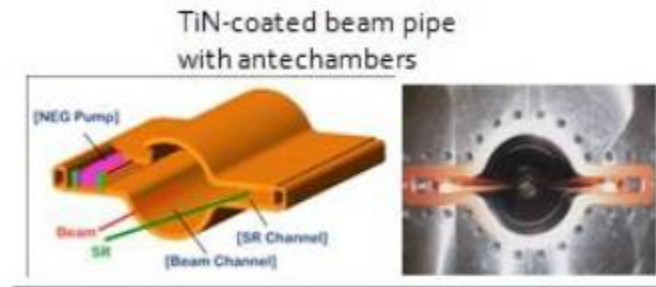


Figure 2.3: New Beam Pipe

The magnetic quadrupoles at the interaction region (IR) as well as the dipole lattice in the rings will also be upgraded, the former for stronger final focusing, the latter to reduce

the accelerator emittance parameters (defined below). This, together with higher currents, will boost the luminosity by a factor of 40 higher than that of KEKB.

One of the Interaction Region upgrades will be the Beam Pipe. Firstly, its diameter will be reduced from 20 mm at the entrance of the beams down to 9mm where the beams cross each other. It will be made out of tantalum to absorb as much as possible of synchrotron radiation and to protect the silicon detector against it. The metallic inner surfaces of the beam pipes before the interaction region will be also coated with a thin layer of gold for the same reason. The IR Beam Pipe schematic is shown in Figure 2.4.

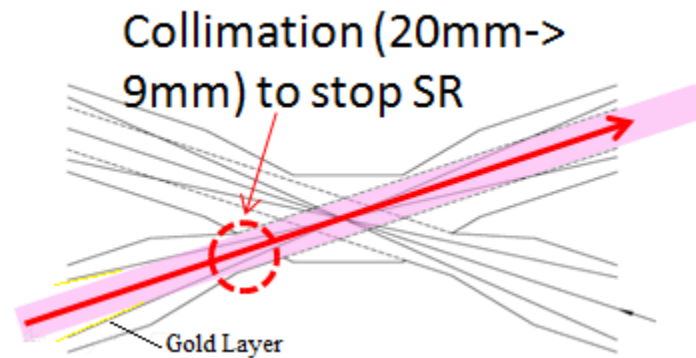


Figure 2.4: New Beam Pipe at the Interaction Region

The KEKB and SuperKEKB machine parameters are summarized in Table 1. It should be noted that the electric currents of the LER and that of the HER are almost twice the KEKB currents. The time separation between two consecutive bunches and the collision frequency at SuperKEKB can be found to be about 4ns and 250MHz, respectively.

	KEKB		SuperKEKB	
	LER	HER	LER	HER
Energy (GeV)	3.5	8.0	4.0	7.007
Beam Current(A)	1.637	1.188	3.6	2.62
Number of Bunches	1584		2503	
σ_y^* (nm)	940	940	48	63

β_y^* (mm)	5.9	5.9	0.27	0.3
σ_x^* (μm)	147	170	10	10
β_x^* (mm)	1200	1200	32	25
σ_z^* (nm)	6	7	6	5
Populations	6.4×10^{10}	4.7×10^{10}	9.0×10^{10}	6.5×10^{10}
ϵ_x (π rad-nm)	18	24	3.2	4.6
ϵ_y (π rad-nm)	0.15		0.0085	0.0132
Circumference (m)	3016			
Luminosity ($\text{cm}^{-2}\text{s}^{-1}$)	2.1×10^{34}		8×10^{35}	

Table 1: Machine Parameters of SuperKEKB and KEKB

2.3.2 LINAC of the SuperKEKB

The LINAC is the first step in the accelerator chain of the SuperKEKB system. It is shown in Figure 2.5.

This accelerator is 483m long and contains two electron guns shooting electrons into two different tubes where electron beams get longitudinally accelerated by RF cavities, where oscillating electric fields are used to accelerate the beams passing through them (Figure 2.6). RF cavities are also used in the rings to replenish the energy lost through radiation.

Electrons in one pipe continue to the end of the LINAC; others in the second pipe strike a tungsten target producing positrons with a wide momentum spread. This generates a positron beam which is broadly distributed in angle and momentum space. Positrons get collimated and accelerated in the remaining part of the LINAC through RF cavities.

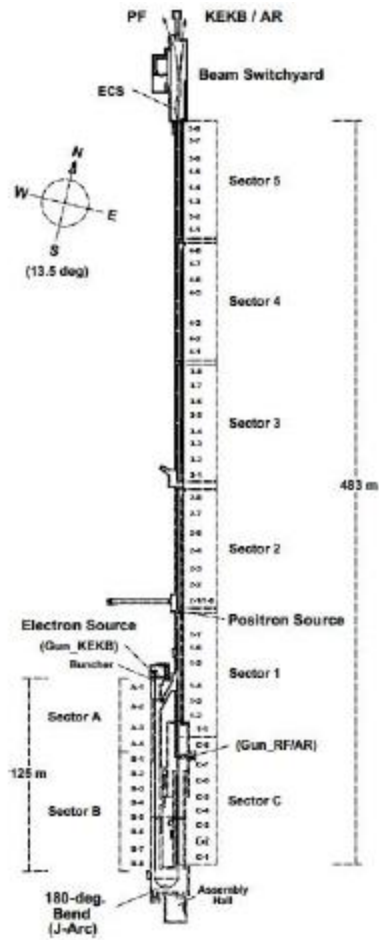


Figure 2.5: LINAC of the KEKB

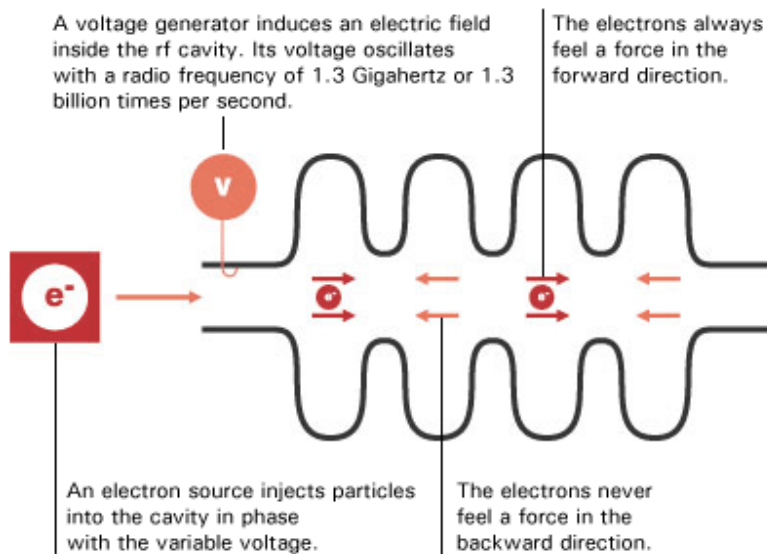


Figure 2.6: Operational Principle of RF Cavities

The beam emittance measures how well collimated a beam is. In accelerator coordinates, x is transverse in the plane of the accelerator (horizontal), y is perpendicular (vertical), and z is along the beam direction of motion. The transverse emittance components ε_x and ε_y can be expressed in terms of the rms transverse beam widths σ_x and σ_y defined as follows [11]:

$$\varepsilon_x = \sigma_x \sigma_{x'} \quad (2.1)$$

$$\varepsilon_y = \sigma_y \sigma_{y'} \quad (2.2)$$

$$\sigma_x^2 = \int (x - \langle x \rangle)^2 \rho(x, x') dx dx' \quad (2.3)$$

$$\sigma_{x'}^2 = \int (x' - \langle x' \rangle)^2 \rho(x, x') dx dx' \quad (2.4)$$

$$\langle x \rangle = \int x \rho(x, x') dx dx' \quad (2.5)$$

$$\langle x' \rangle = \int x' \rho(x, x') dx dx' \quad (2.6)$$

Where x' and y' are the derivatives $\frac{dx}{dz}$ and $\frac{dy}{dz}$ respectively; $\rho(x, x')$ represents the beam's distribution function.

The lower the beam emittance is the finer the beam size. This leads to more overlapping between the colliding beams, and eventually increases the luminosity (defined in Ch. 1, and formally defined below).

At the end of the LINAC (Switchyard), there is a series of dipole magnets called septum shown in Figure 2.7. These magnets provide a strong pulsed magnetic field that

kicks the electrons in one direction into their ring and positrons in the opposite direction into the damping ring before they get injected into their own ring for colliding.

The damping ring structure is very similar to a storage ring but smaller if compared to it. It is wrapped with a series of quadrupoles, dipoles, and RF cavities helping in collimating and accelerating the positrons. Moreover, special magnets, with alternating up and down dipoles, called wigglers, speed the rate of energy loss. After that, the positron beam becomes ready to be injected into the corresponding storage rings synchronously with the electrons but in opposite directions.

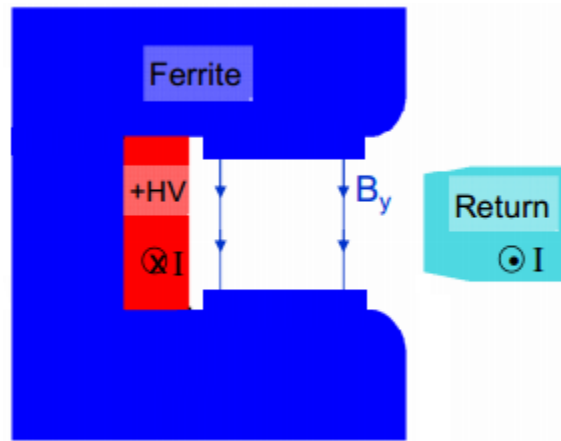


Figure 2.7: Beam Kicker Schematic

2.4 Storage Rings

A storage ring as its name suggests is a ring where particles can be stored and maintained at the same energy for a long time (few minutes to few hours). Such a ring is not perfectly circular but rather an octagon with eight curved corners. At each bend, a set of dipoles acts as a prism to bend the beam toward the next straight section (Figure 2.8).



Figure 2.8: SuperKEKB Dipole Magnet

The transfer matrix M describing the transverse motion of a charged particle inside dipoles in terms of its length l can be written as [2]:

$$M = \begin{bmatrix} 1 & l \\ 0 & 1 \end{bmatrix} \quad (2.7)$$

Where M changes the state of the charge particle say from $\begin{pmatrix} x \\ x' \end{pmatrix}$ to another state $\begin{pmatrix} x_1 \\ x'_1 \end{pmatrix}$ as follow:

$$\begin{pmatrix} x_1 \\ x'_1 \end{pmatrix} = M \begin{pmatrix} x \\ x' \end{pmatrix} \quad (2.8)$$

On the storage ring and along with dipoles, there are magnetic quadrupoles on the lattice serving as focusing and defocusing lenses to focus and defocus the beam in order to keep it within the Beam Pipe volume as shown in Figure 2.9.

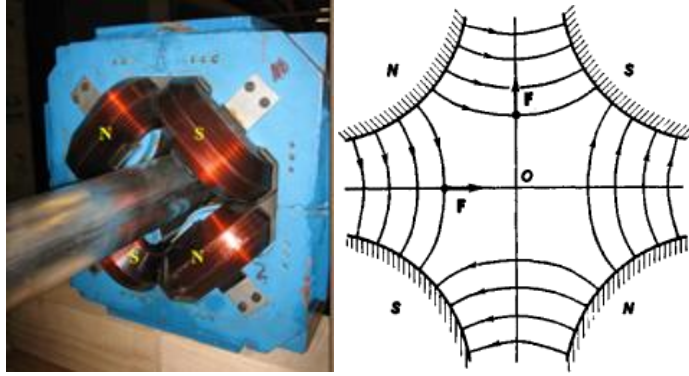


Figure 2.9: Left: Quadrupole Magnet Oriented at 45deg, Right: Magnetic Field Lines

Quadrupoles only focus in one transverse dimension and defocus in the other. One of the great pillars of accelerator technology is the fact that a triplet of alternated focusing and defocusing quadrupoles, with well chosen strength, has the overall effect of focusing (weakly) in both transverse dimensions. As such, quadrupoles act as magnetic lenses on a diverging beam, keeping it focused and inside the Beam Pipe.

The focusing scheme is shown in Figure 2.10.

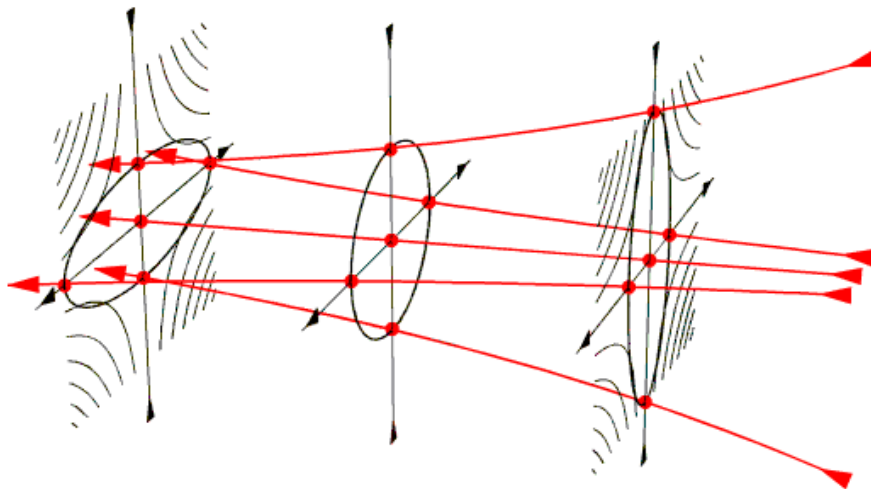


Figure 2.10: Quadrupole Focusing Principles

These magnets also affect the state of particles inside the storage ring by their own transfer matrices:

$$M_{focusing} = \begin{bmatrix} 1 & 0 \\ -\frac{1}{f} & 1 \end{bmatrix} \quad (2.9)$$

$$M_{defocusing} = \begin{bmatrix} 1 & 0 \\ \frac{1}{f} & 1 \end{bmatrix} \quad (2.10)$$

In addition to dipoles and quadrupoles, another type of magnets can be added to the lattice to correct chromatic effects, the Sextupole (Figure 2.11).

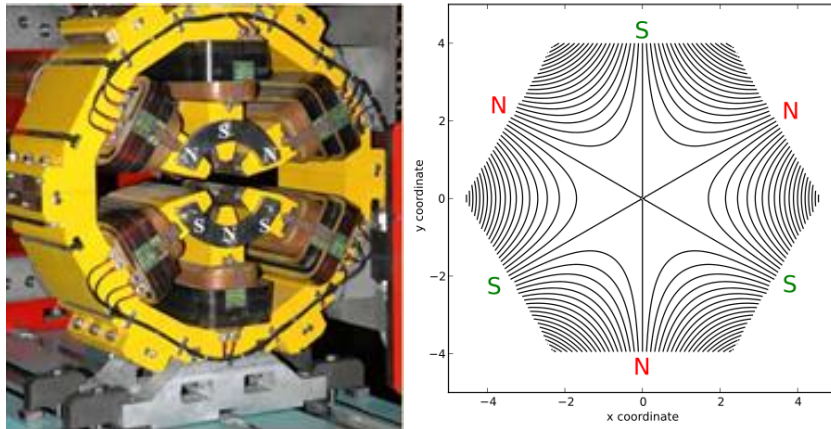


Figure 2.11: LEFT A Sextupole Design, Right: Magnetic Lines of a Sextupole

As a result, the lattice of all magnets can have a total transfer matrix equal to the multiplication of all matrices acting on the initial to obtain the final state of the particle as shown in Eq. 2.9.

Questions about the beam size, collision type, and beam diagnostics can be simply answered or understood by using a very effective tool called the large angle

beamstrahlung that will be discussed later in this chapter. However, the first question finds its answer at an accelerator whose name was already mentioned: the SuperKEKB.

2.5 Luminosity

The luminosity can be expressed in terms of the beams densities as:

$$L = f|v_1 + v_2| \int \rho_1(x, y, z, t) \rho_2(x, y, z, t) dx dy dz dt \quad (2.11)$$

Where f is the collision frequency, ρ_1, ρ_2 represents the both beams density, v_1 , and v_2 clearly represent the velocities of the beams.

The luminosity formula can be quite cumbersome, but in the special case of two equal beams in a head-on collision the integral can be easily solved to give:

$$L = \frac{N_1 N_2 f}{4\pi \sigma_x \sigma_y} \quad (2.12)$$

Where N_1 and N_2 are the beams populations, and f is the collision frequency. The best way to increase luminosity is to decrease the transverse beams dimensions σ_x or σ_y . Figure 2.12 shows the beam transverse size improvement that is expected when going from KEKB to SuperKEKB.

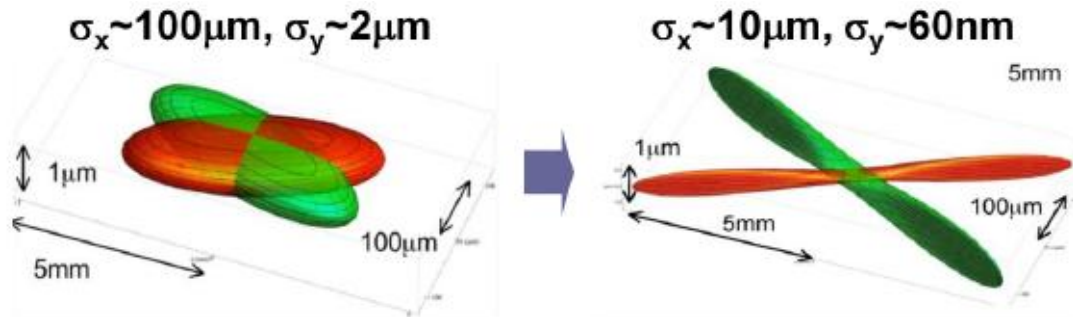


Figure 2.12: Electrons-Positrons Beams at KEKB (Left) and SuperKEKB (Right)

Compared to KEKB, at the new SuperKEKB the beams are focused much more tightly. At the same time, the new beams, only 60 nm high, may jitter due to ground motion, and have emittance growth from magnetic fringe field or magnetic drift.

The main point of our project is to provide a monitor that detects and diagnoses such effects, so that they can be corrected by small corrector magnets. Also, this device should be useful during accelerator experimental periods, called Machine Studies, when machine parameters are artificially changed in an effort to learn more about the Twiss matrix of the machine. Great importance is given to be able to observe the machine parameters at the IP directly.

2.6 The Belle II detector

For sake of completeness, a brief overview of the particle detector surrounding the IP is given. The Belle II detector is a general purpose particle detector. It contains many layers specialized in detecting particles decay vertices, momenta, velocities, and energy. Starting from inside, there is a silicon vertex detector, a drift chamber, Cherenkov Ring Imaging, electromagnetic calorimeter, and the muon chamber (which doubles also as Hadronic calorimeter) as shown in Figure 2.13.

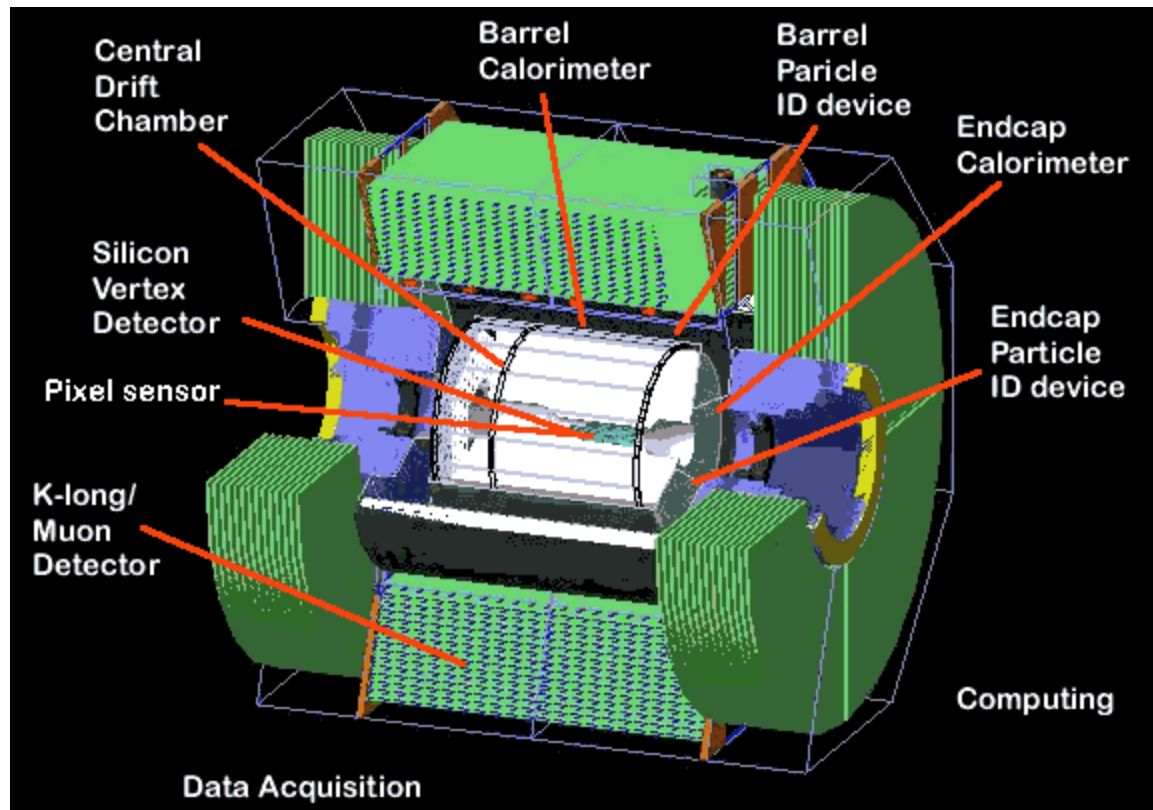


Figure 2.13: The Belle Detector

The silicon vertex layer represents the first layer of this detector and has high resolution detection. The next layer is the tracking chamber or the central drift chamber which captures and tracks various charged particles to determine their momentum and (in conjunction with the silicon vertex detector) eventually reconstruct decays' vertices.

This inner layer is encapsulated by the so-called ring imaging Cherenkov detector, and it is part of the particle identification systems. This detector measures a charged particle's velocity, and this information, together with the particle momentum, leads to identification of the particle's mass. When a charged particle enters the medium (radiator) at a speed greater than the phase velocity of light, it radiates (mainly in the UV), and the photons are measured by a photon detector.

The Cherenkov ring imaging layer of Belle II is surrounded by a layer that is designed to measure energy of penetrating particles and is called calorimeter, which measures the particle's energies. The calorimeter can also detect neutral particles.

The outermost layer of the Belle II detector is called the Barrel Muon Chamber that is designed for detecting muons as they escape the previous layers without interaction.

Although Belle and Belle II are alike in design, they differ in angular coverage (due to the different energy asymmetry of the two colliders, and the closer final focus quadrupoles), and the detectors, in particular significantly better vertex and mass resolution.

2.7 Large Angle Beamstrahlung

When the two relativistic beams cross one another they emit radiation as each beam bends the other due to their electromagnetic fields. This radiation is called beamstrahlung and can be used to monitor the beam interaction. It is somewhat similar to that of a synchrotron radiation emitted by charged particles suffering bending in a very long and strong quadrupole magnet. The only difference is that instead of a strong long magnet, a strong short magnet ($L = \frac{\sigma_z}{2\sqrt{2}} = 2mm$) is acting on the particle, thus short magnet radiation.

Short magnet radiation [12] has a much broader angular distribution than normal synchrotron radiation, which is mainly at angles of order $\frac{1}{\gamma}$ with respect to the particle direction of motion. In the case of the device presented below, detection is done at angles close to 10 mrad, where most of the machine background radiation is absent. γ is the

Lorentz factor and can be estimated by $\gamma = \frac{E}{E_0}$ to be 8000 (LER) and 14000 (HER); E is the energy of the charged particle, and E_0 is the rest energy of an electron (0.511 MeV).

Our techniques consist of designing and building the beamstrahlung detector in such a way that it helps in analyzing polarized radiation having wavelengths within the visible range (350nm to 650nm). The beamstrahlung detector parameters are determined and shown in Table 2.

	LER	HER
Polar Angle (mrad)	$9.9 \leq \theta \leq 10.4$	$7.8 \leq \theta \leq 8.2$
Azimuthal Range (rad)	$\pm \frac{\pi}{2} - 0.004 \leq \Phi \leq \pm \frac{\pi}{2} + 0.004$	
Spectral Wavelength (nm)	$350 \leq \lambda \leq 650$	

Table 2: Beamstrahlung Detector Parameters

The radiated energy emitted by a particle can be expressed in terms of the angular distribution and polarization parameters (θ and Φ) as follows [12]:

$$\frac{dU}{d\Omega} = \frac{2e^4}{\pi m^2 c^4} \gamma^4 (1 + \gamma^2 \theta^2) f^2(\theta, \Phi) \int B^2(z) dz \quad (2.13)$$

Where $f^2 = f_{\parallel}^2(\theta, \Phi) + f_{\perp}^2(\theta, \Phi)$ the sum of both polarizations; m is the electron's mass and e its elementary charge; $\mathbf{B}(z)$ is the magnetic field of the beam causing the deflection; c is the speed of light. Further,

$$f_{\parallel}(\theta, \Phi) = (1 + \gamma^2 \theta^2)^{-3} (1 - \gamma^2 \theta^2 + 2 \gamma^2 \theta^2 \sin^2(\Phi)) \quad (2.14)$$

$$f_{\perp}(\theta, \Phi) = -2(1 + \gamma^2 \theta^2)^{-3} \gamma^2 \theta^2 \sin(\Phi) \cos(\Phi) \quad (2.15)$$

$$d\Omega = \sin(\theta) d\theta d\Phi \quad (2.16)$$

These two functions along with an appropriate small angle approximation helped in simplifying the radiated energy formula and in writing simulation software to calculate

the total power for each polarization. All of that was already accomplished by Ryan Gillard in his dissertation.

The computed powers and all beamstrahlung parameters can be summarized in Table 3.

	LER	HER
Total Power (W)	1224	2033
Illumination (eV)	5×10^{10}	7.8×10^{10}
Collinear U_x/U_y	2.89	2.93
Large Angle U_x/U_y	5.21	5.37
Total Photons/Mirror	1.37×10^{10}	2.00×10^{10}

Table 3: Beamstrahlung Parameters.

Illumination refers to the visible energy intercepted by our detector.

It is evident that the idea behind designing and building such a detector is to correct all beam misalignments by reconstructing the photon fluxes and is covered in the next two chapters. The way to reduce other background is by observing beamstrahlung through a double collimation telescope. The two collimators, discussed in Chapter 3, are the extraction window and the Wollaston prism.

Beamstrahlung can be used as a tool of beam diagnostics [13]. The detector helps in collecting measurements of the power radiated in each linear transverse polarization in a way that provides a signature of the beams properties and can be compared against the calculated energy for each polarization as shown in Figure 2.14.

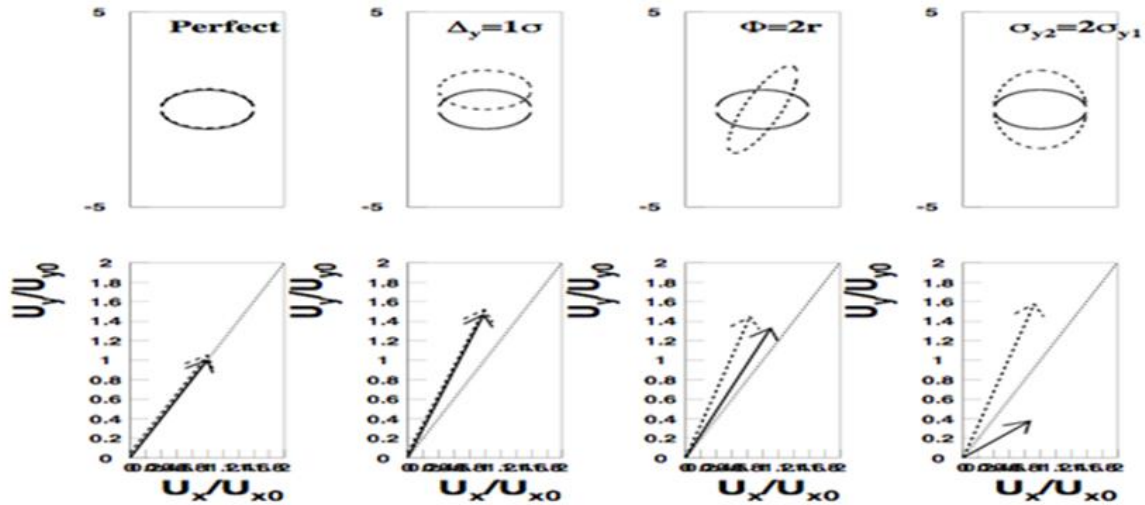


Figure 2.14: Normalized beamstrahlung Powers vs. the Collisions Types

The top-left part of the figure shows the typical case of a head on collision where the two beams (solid and dashed lines) are on top of each other (perfect) collision. Below it, the normalized powers, in x and y for each beam, are plotted as two arrows. The next one is when one beam is in a vertical offset and the beams basically miss each other diminishing luminosity. The signature is that the radiation emitted by both beams becomes y-polarized, by the same amount. Other mismatches, depicted in Figure 2.14, also produce unique polarization patterns.

From the number of the observed photons the user would obtain the integrated power received by all PMTs, then compare measurements to the theoretical ones that were computed numerically and corrections or adjustments to the beams will be made accordingly. Furthermore, the spectral analysis helps in subtracting all unexpected backgrounds by comparing data at different wavelengths.

The next chapters show the complete design of a detector that aims at answering all these beam overlap questions.

Chapter 3 : Designing the Beamstrahlung Detector

3.1 An overview on the large beamstrahlung detector:

As mentioned in the previous chapter, the beamstrahlung detector (LABM or Large Angle Beamstrahlung Monitor) is used at Belle II in SuperKEKB to detect radiation due to the interaction of crossing beams. The detector is based on extracting light from the main beam pipe, where the beams intersect, and to get this radiation into the optics box as shown in Figure 3.1. It is, basically, a narrow telescope, its acceptance limited by a double collimator, to view only a small region inside the Beam Pipe at any given time.

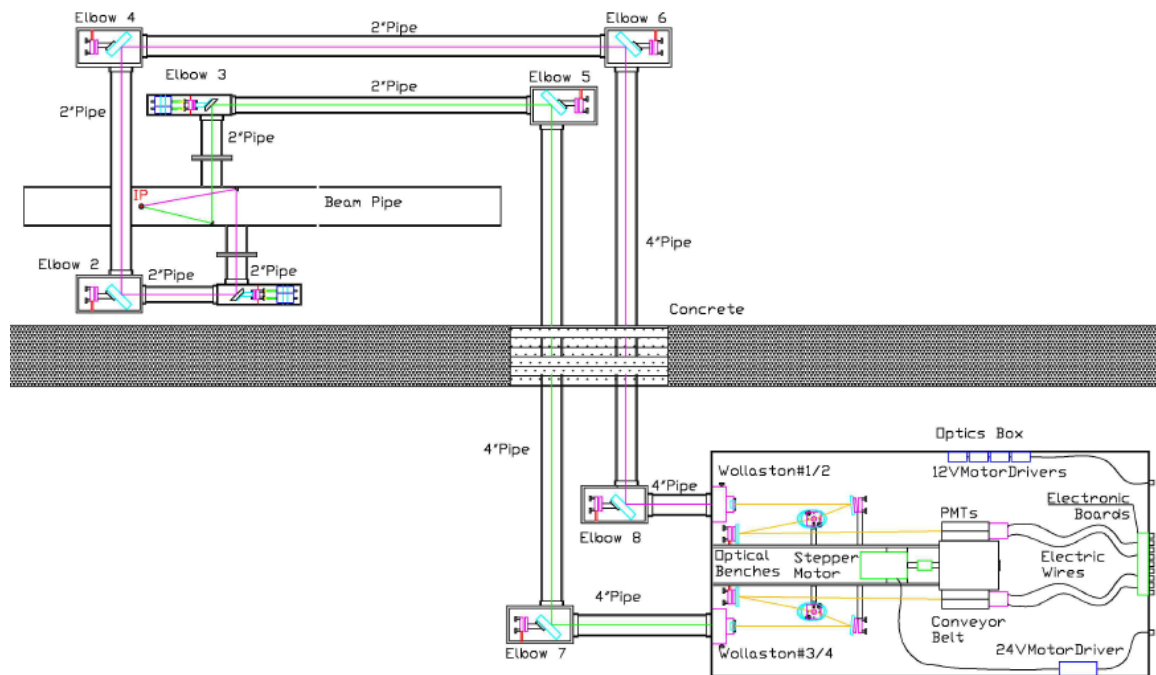


Figure 3.1: Schematic of the Beamstrahlung Detector That Will Be Used at BELLE II

The main components of the LABM are a Beam Pipe insert, produced by KEK. This object extracts light from the Beam Pipe (in vacuum) to the outside world. The next

component is the Primary Elbow, which is a remotely controlled mirror used to point the LABM to different regions inside the Beam Pipe. The next part, the Optical Channel, delivers the light to a low-radiation area and to the Optics Box. The Optics Box analyzes the light polarization and spectrum; all these parts were built at Wayne State. The electronics and Data Acquisition are the responsibility of Sinaloa and Puebla, and of University of Tabuk.

From the primary elbows, light is reflected through an Optical Path shown in Figure 3.1, consisting of aluminum tubes with other, larger “manual” elbows. Manual elbows connect two tubes of 2in and 4in or two 4in tubes. From manual elbows, radiations continue their paths all the way down through a concrete floor to a room where the optics box resides.

Finally, both beams of light get into the optics box through two windows to meet a Wollaston prism, which is a polarizer, splitting the light into linearly polarized components. Each polarized beam is guided onto a ruled diffraction grating. Once polarized light hits the grating, it gets diffracted and decomposed into its basic wavelengths that can be detected by an array of four photomultipliers carried by a conveyor belt.

The main role of the conveyor belt is to swap photomultipliers of the same array or of a different one (detailed in conveyor belt section) for calibration purposes. The optics box also contains four drivers and their 12Volts power supply for primary elbows stepper motors in addition to one 24Volt driver for the conveyor belt stepper motor. On the back of the optics box there is a circuit board with 16 channels to feed all PMTs with high

voltage and to get signal from PMTs through electric wires. From outside, the circuit board has 16 sockets allowing the user to connect them to 16 digital counters as well as sockets for the motors drivers.

3.2 Beam pipe and its components

The Beam Pipe is an 8cm (3.15in) titanium pipe, in which beams circulate in high vacuum. To get the wavelengths of interest outside, two Beryllium mirrors of $2 \times 2.8\text{mm}^2$ each are placed away from each other by 6.2cm inside the beam pipe at 45° with respect to the Beam Pipe axis.

The two Beryllium mirrors are small in size to limit RF heating and noise (about 30 Watts at nominal conditions, the mirrors are water cooled). One ramification is that diffraction effects are not negligible, but also they act as the first collimator in a double collimator scheme (the Wollaston prism is the other collimator). On the beam pipe and across from mirrors, there are two windows of 8mm diameter made of fused silica, through which the reflected radiation escapes the beam pipe. Each window is mounted on a flange which connects mechanically to the LABM (Figure 3.2).

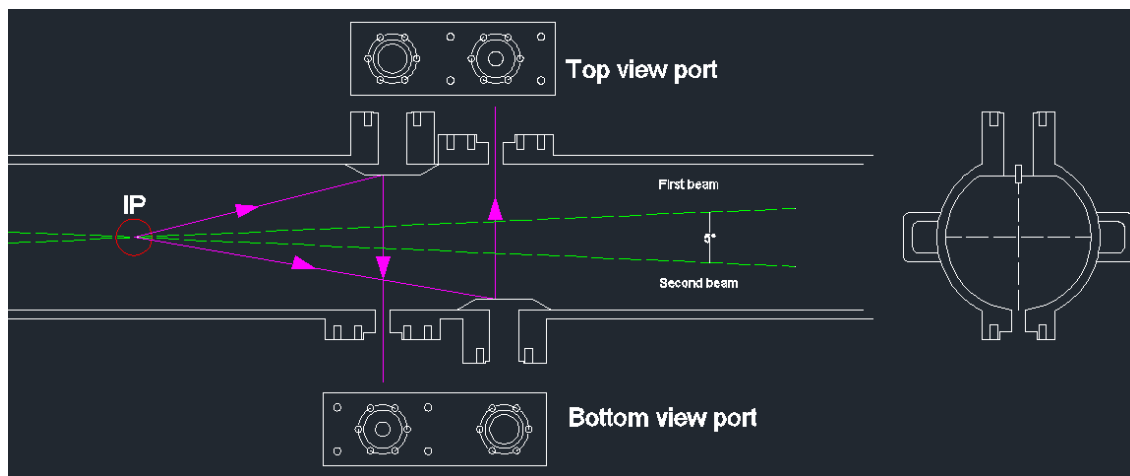


Figure 3.2: LABM Light Extraction Element in the Beam Pipe.

3.3 Before Primary Elbow

Since primary elbows support connections between one inch tube and another of different size mainly 1.5in, they have to have two different aluminum tube adapters. The tube adapters are made out of two identical aluminum pieces of $\frac{1}{2}$ in thickness and $2.5 \times 2.5 \text{in}^2$ each and can be easily mounted on the elbow. One of the plates has a circular aperture with a threading diameter of 1.9393in, and it can be placed on the front of the elbow via screws as shown in Figure 3.3.

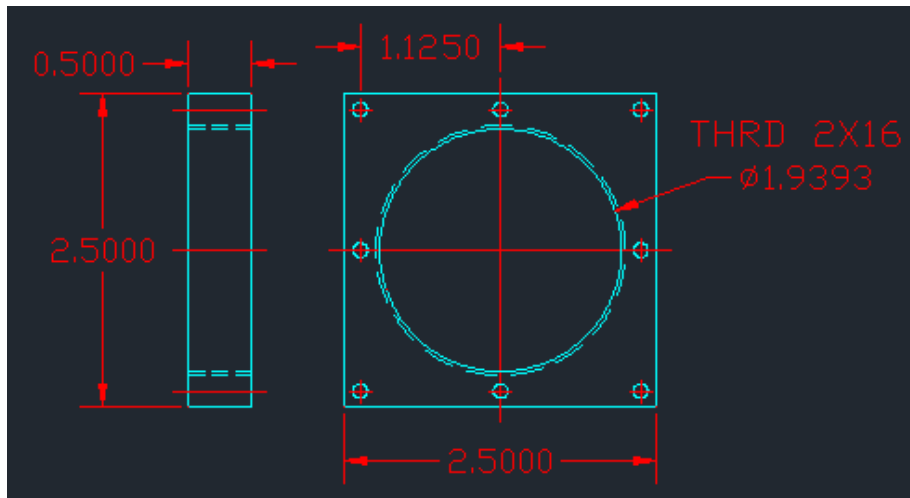


Figure 3.3: The Front Adaptor Tube That Connects Primary Elbow to the Beam Pipe adapter.

The other one however has a circular aperture of 1.1811in, and can be placed on the top of the elbow via screws. It is made in a special way so that it assures the connection between primary elbow and the aluminum pipe through four set screws on the one side. On the other side, the aluminum tube was machined as a solid piece having a plate shape allowing the tube to be connected to the main beam pipe as shown in Figure 3.4.

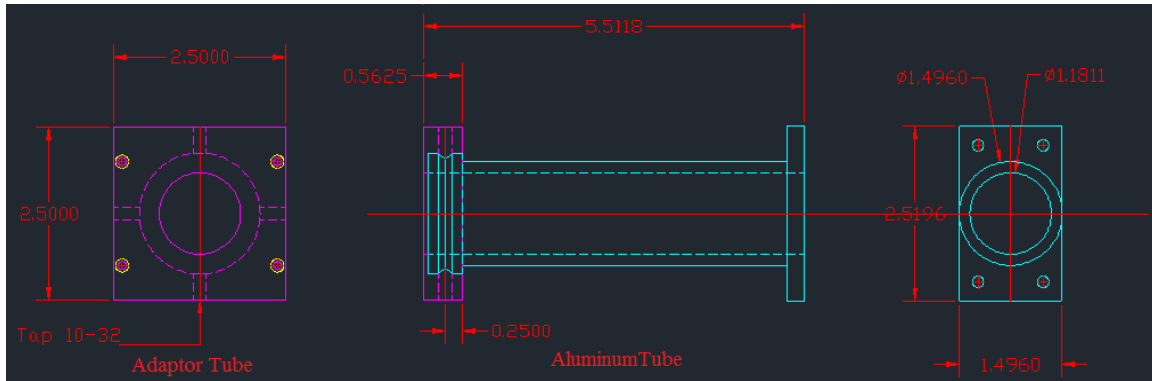


Figure 3.4: Primary Elbow Top Adaptor (left), Aluminum Tube (middle)

The finished adapter connecting the primary elbow the beam pipe is picture in Figure 3.5.



Figure 3.5: The Primary Elbow to Beam Pipe Connector

This adapter tube has a small round window of 0.5in diameter with a holder allowing some other tools, such as an LED strip or an optical fiber transmitting light to inside the adapter, to be inserted in for preliminary test as shown in Figure 3.6.

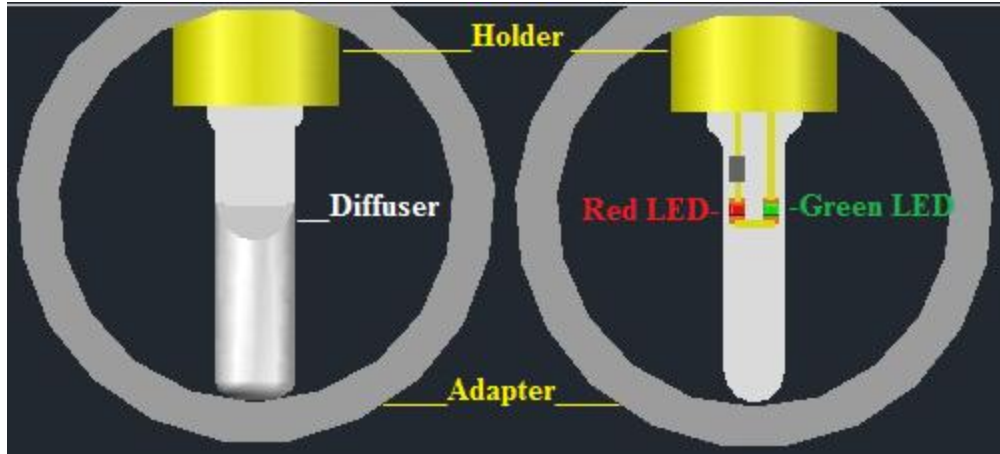


Figure 3.6: L-R Diffuser and LED Strip at the Center of Adapter Tube

The diffuser receives light from outside through an optical fiber and diffuses it in all directions helping in testing elements alignment and PMTs. The LED strip has two LEDs of different colors mainly red and green. The latter not purely chromatic, but they have some bandwidths spread including the intended one that the optics box was originally made for. This tiny tool has the same role as the diffuser but with more intense light with some specific wavelengths, and will serve to visually align the Optical Channel.

3.4 Primary Elbow: Purpose, Components Design, and Production

The first elbow in the Optical Channel is the Primary Elbow. It is the first element to be directly connected to the view port on the beam pipe. As stated earlier, this device points the LABM in different directions. It is located in a high radiation zone that cannot be accessed; therefore, the mirror inside the elbow has to be remotely controlled. Also, having two identical view ports, one at the top and one at the bottom of the Beam Pipe, requires two primary elbows on either side, four in total.

A technical difficulty in building this device was that the mirror control system that was usually made out of plastic. Angular orientation is driven by two screws pushing and pulling at opposite points along a diameter of the mirror. The motion of the screws changes the distance between the two points of contact, which is accommodated by the plastic stretching. Because plastic cannot be used in this environment, square brass rods were used, which can move along the axels.

A primary elbow comes out to be a $2.5 \times 2.5 \text{in}^2$ black anodized and finished aluminum box of 8in long and $\frac{1}{4}$ in thick to protect all components inside it. It is designed in a compact way so that it contains small sized components like: an elliptical flat mirror, a 45° mounting adaptor, a mirror mount and its studs, two square brass rods, two stepper motors and their mount, a circular window on one of its sides, and finally a back cap as depicted in Figure 3.7.

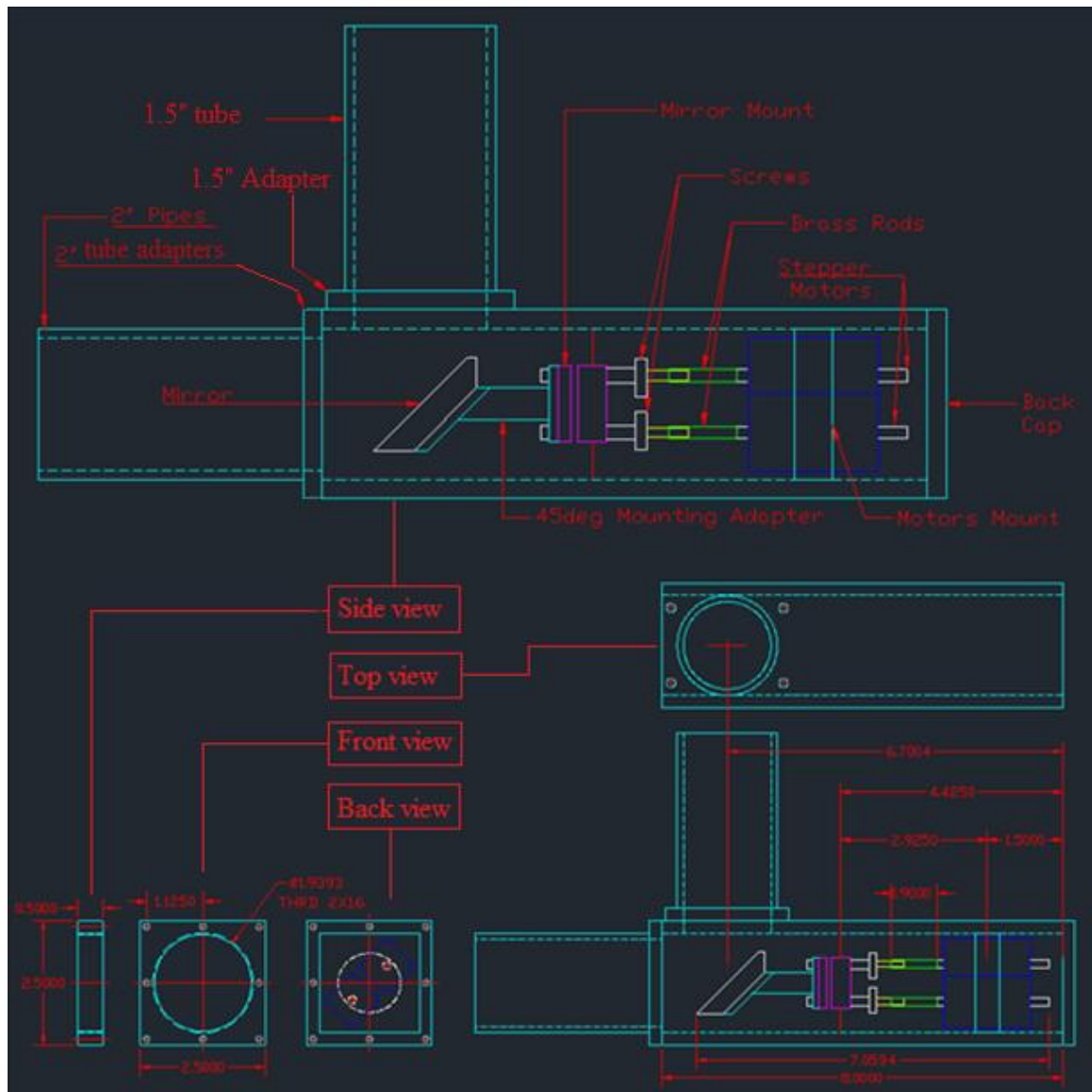


Figure 3.7: Primary Elbow Design and Its Constituents.

3.4.1 The Primary Mirror

It is located inside the primary elbow and it is the mirror where the second reflection takes place after the beryllium mirror inside the Beam Pipe. It is the eye that allows looking at different radiations areas inside the beam pipe. It is an elliptical flat mirror with 0.875in and 1.237 in minor axis and major axis, respectively. The mirror is oriented at 45 degrees and is coated with a UV-enhanced aluminum layer on its first surface to

avoid light attenuation in the medium of the mirror. The mirror is mounted on a post through a small aluminum disk of 1in in diameter and $\frac{1}{4}$ in thickness having a tapped hole at its center and is being glued to it such that the center of the disk is aligned with that of the reflecting face as depicted in Figure 3.8.

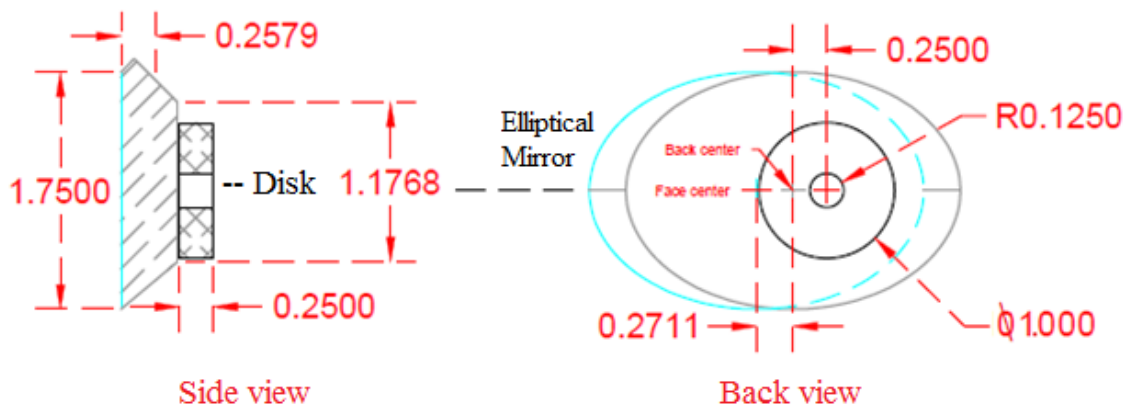


Figure 3.8: An Elliptical Primary Mirror and Its Mounting Disk

The picture also shows that the aluminum disk can be glued to the mirror at an offset about its thickness from the center of the back elliptical face. The technique of determining where to glue the disk consisted of laying down the mirror on its back and tracing it on a piece of paper. Cutting all unnecessary parts helps in folding it symmetrically in both directions. After determining the center of the ellipsoid, the later was translated by exactly the thickness of the aluminum disk ($\frac{1}{4}$ in) where the center of the disk should be.

3.4.2 The 45⁰ Mounting Adapter:

The primary mirror can be held at 45 degrees from a $\frac{1}{2}$ in diameter post by using an easy-to-use aluminum adapter of 1" offset to hold any component as shown on the right

of Figure 3.9. A socket head cap screw for the $\frac{1}{4}$ in counter bore allows the mounted component to be rotated and fixed in position in the 45° plane if necessary.

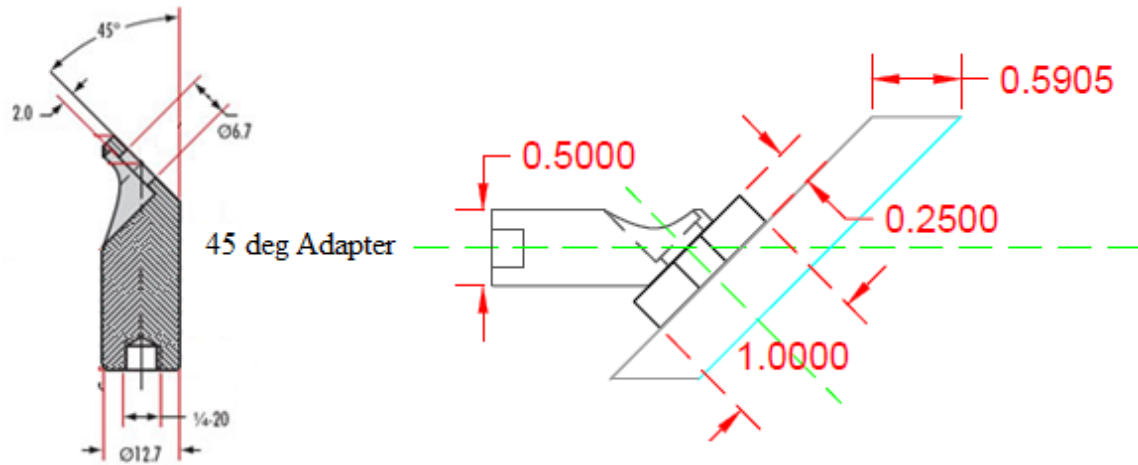


Figure 3.9: 45deg Aluminum Adapter (left) With the Mirror (right)

3.4.3 Mirror Mount and Its Studs:

The mounting adapter can be mounted on a 1in mounting surface having four identical and tapped holes of a black anodized aluminum miniature straight mirror mount shown in Figure 3.10.

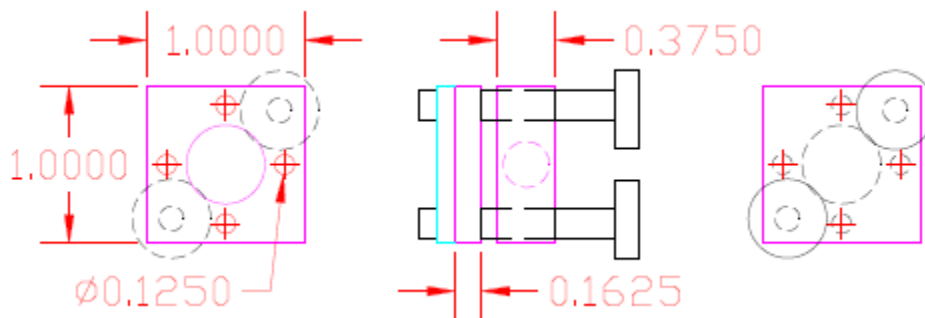


Figure 3.10: Mirror Mount Schematics

The mount includes two fine resolution angular adjustment screws offering the mounting surface two degrees of freedom at a rate of 0.015in per turn. It also has on its

four sides four tapped holes to allow the mount to be installed inside the elbow. To get the mounting surface back to its original position, the mount is also provided with a stiff spring joining the installed part and the mounting surface. Moreover, the mount can be installed and maintained centered with the elbow by using two long screws that go through two studs as shown in Figure 3.11.

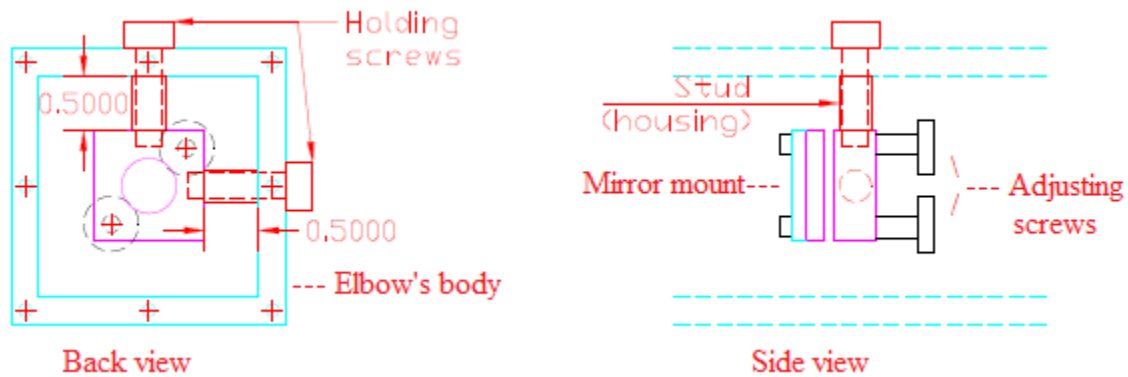


Figure 3.11: Mirror's Mount Connection to the Primary Elbow

3.4.4 Square Brass Rods:

Because the mount was designed for manual control, some new designs must be invented to make a mechanical connection between stepper motors and screws. The axel of the stepper motor and the diameter of the screw have different sizes, 0.157in and $\frac{1}{2}$ in, respectively. Therefore, to make the screws compatible or controllable by the stepper motor, a square piece of brass as big as that of the axel size was glued on the screw at its center. Then the square brass rod encloses the motor axel and the square piece of brass that is being glued to the screw.

When the motor rotates, the brass rod rotates with it turning the screw backward or forward and, thus, the square piece smoothly slides inward or outward from the brass rod

with no friction as shown in Figure 3.12. Note that intersection length between the cubic piece and the brass rod is $\frac{1}{4}$ in which is enough for adjusting the mirror. Typically, each turn pushes inward or outward the mounting surface by 0.015in. Thus, the intersection distance requires $\frac{0.25 \times 1}{0.015} = 16$ turns which is of course more than enough to center the mirror.

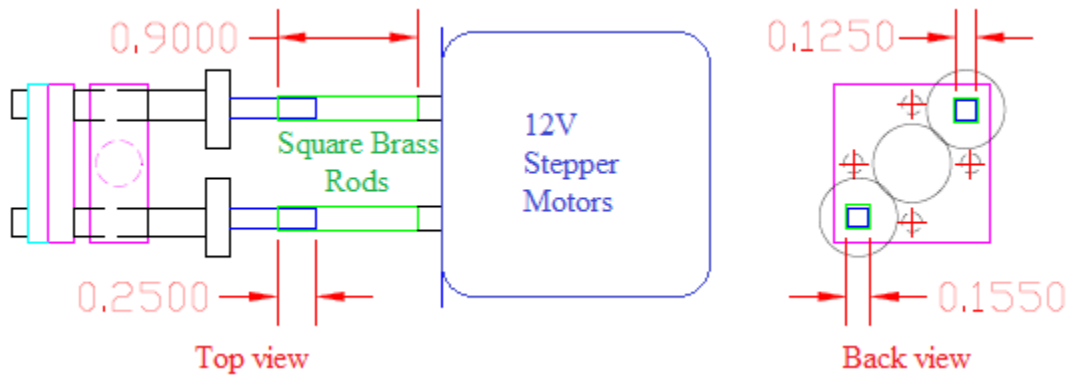


Figure 3.12: Square Brass Rods Schematics.

3.4.5 Stepper Motors and Their Mount:

As detailed in the previous paragraph, there are two stepper motors inside each primary elbow, one per screw. The stepper motors used in primary elbows are all identical, with size $0.8 \times 0.8 \text{in}^2$ and axel diameter of 0.157in (Figure 3.13). Each stepper motor is powered by a 2A, 12V driver. The low power is sufficient since the torque needed to rotate a screw is not large.



Figure 3.13: 12V-2A Electric Motor Design.

The motors need a mount to hold them diagonally inside the elbow as shown in Figure 3.13. The mount of $2 \times 2 \text{in}^2$ and $\frac{1}{2}$ in thickness has two square windows of $0.8 \times 0.8 \text{in}^2$. Each window is provided with a tiny screw that can be tightened in to hold the stepper motor in the specified place. On the outside of the mount, there are two pin holes designed so that two pins can be easily inserted in and taken out to attach and detach the mount to and from the elbow, respectively. The reason for using pins and not screws is so that the motors do not get jammed before they operate. Notice that the motors are to be held diagonally because the mount's screws are diagonally positioned on the mount as shown in Figure 3.14.

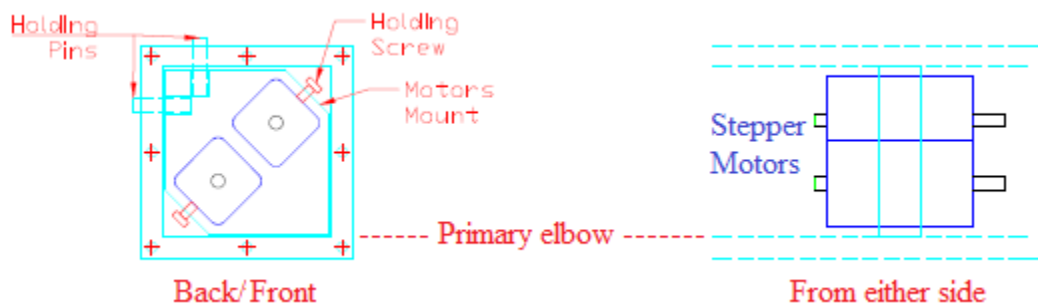


Figure 3.14: Mounting the Motors on Their Mount inside Primary Elbow.

3.4.6 Circular Window:

This window was designed to allow inspection of the brass rods system during assembly. It also allows the user to manually control the mirror for a preliminary testing by rotating the mount screws as shown in Figure 3.15.

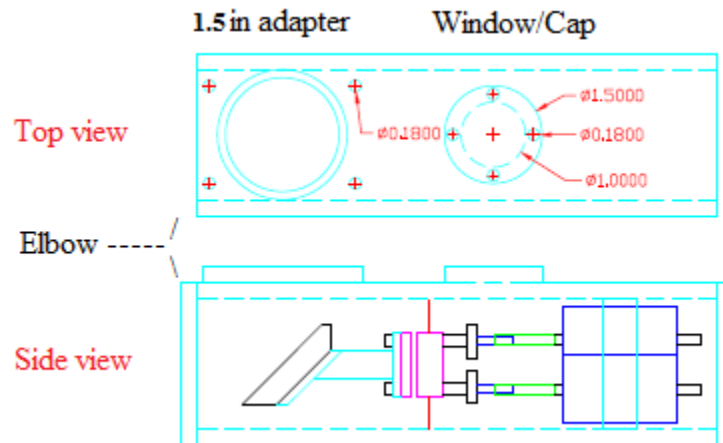


Figure 3.15: A Primary Elbow and Its Circular Window to Viewing the Brass Rods

3.4.7 Back Plate:

It is an aluminum plate of $\frac{1}{4}$ in thickness and 2.5×2.5 in and is used to cover and protect the elbow from the back. It has a $\frac{1}{2}$ in hole allowing the cables of the stepper motors to get outside the elbow (Figure 3.16).

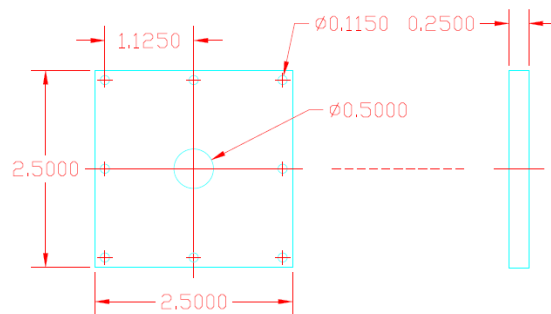


Figure 3.16: Back Plate That Covers a Primary Elbow and Allows Motors Wiring

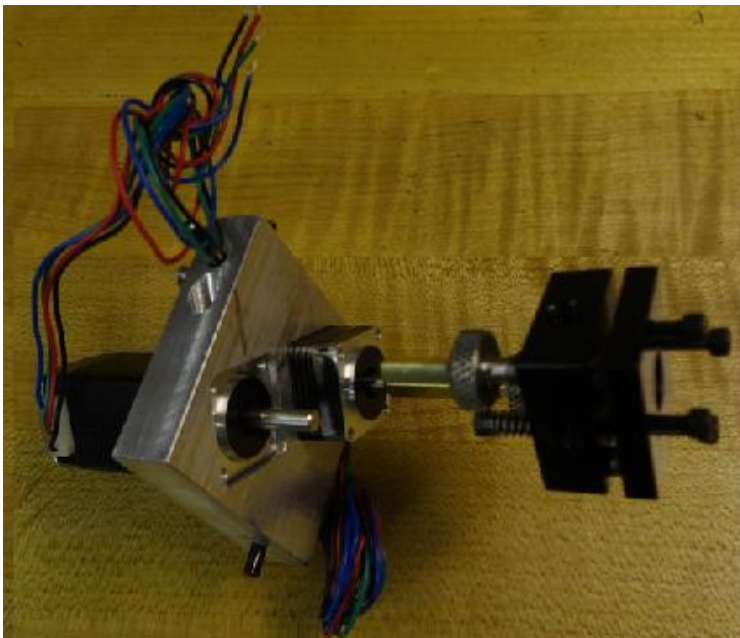
3.4.8 Primary Elbows Production and Hardware:

A finished primary elbow is depicted in the following picture (Figure 3.17).



Figure 3.17: Primary Elbow

Each of the stepper motors inside a primary elbow can be driven by a 12V driver shown in Figure 3.18. Because drivers receive signals from a computer through a serial port via a RS-232 cable, up to sixteen drivers can be daisy-chained at the same time through one serial port reducing the number of wires significantly.



R356 Stand Alone control/
drive + encoder



Figure 3.18: A 12V Driver Used to Control a Stepper Motor

The driver can be accessed and controlled from a Windows terminal where the terminal should be set to its regular setup: 9400 baud rate, 8 bits, no parity and handshaking, and 1 stop bit. Each driver has a hexadecimal coding spindle switch allowing the user to select the desired address. Testing the codes and controlling stepper motors will be explained in the next chapter.

3.5 Piping

These are all pipes and tubes connecting different elbows from the main beam pipe all the way to the optics box; there are two different types of them, 2in and 4in pipes. All 2in pipes connect to the Primary Elbow. The 2in pipes are used just in region where the beam pipe is. As light travels farther inside the pipes, the alignment is more uncertain and 4in pipes are used (Figure 3.1). The light path through all pipes and tubes from the view ports to the optics box is about 8.5(11) meters long for the upper (lower) window. The 4in pipes will have baffles of the same size to block all internal reflections.

3.6 Manual Elbows Design, Production, Sandblasting and Anodizing

The manual elbow was designed in a similar way that a primary elbow was, but with several differences. The mirrors in manual elbows are aligned manually and once, during installation. Also, they are made out of 0.125in thick aluminum plates that can be joined together via screws or welded together.

Manual elbows are also designed so that at the front, between the tube adapter and the body, there is a slit allowing a 1mm diaphragm to fit in. The diaphragm is a thin piece of aluminum that has a small hole at its center and can be inserted allowing the collimation

of light. Diaphragms of different holes sizes can be used not only to collimate light, but also to adjust manual mirrors and guide light at the center of the tubes. The first manual elbow in each Optical Channel adapts to the 2in pipe coming from the Primary Elbow (Figure 3.19), while all other elbows connect to 4in pipes.

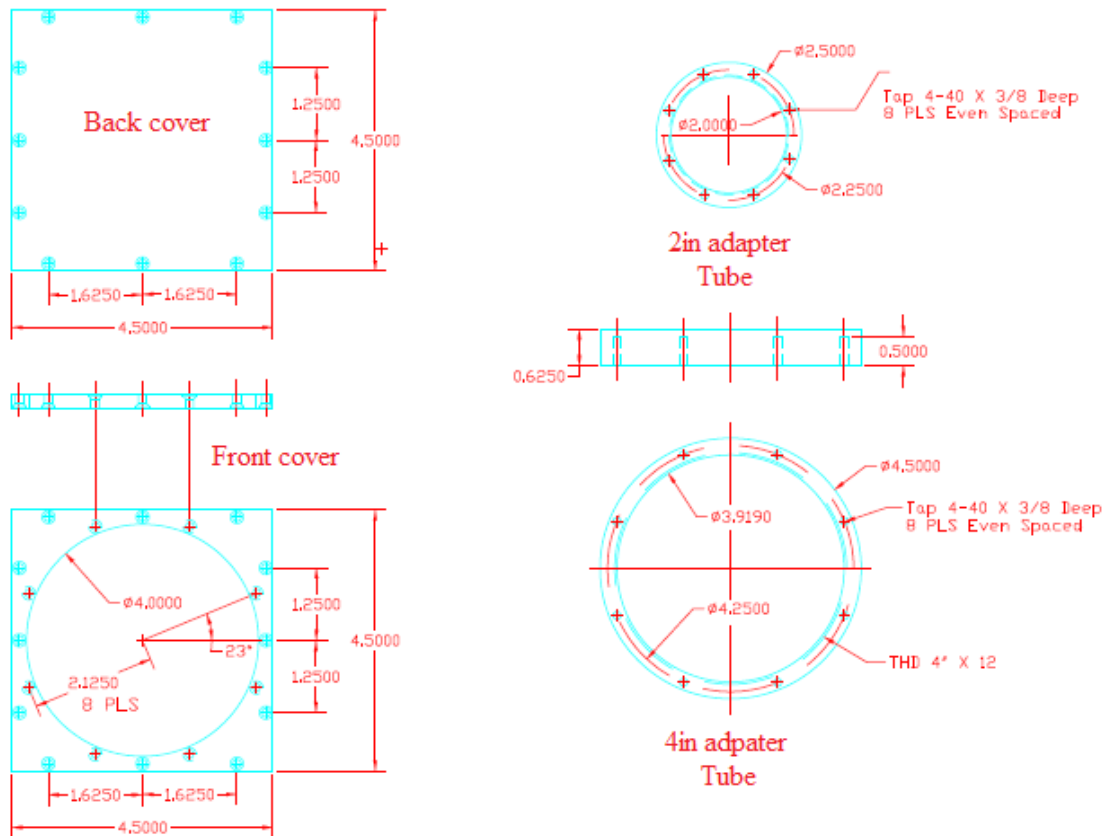


Figure 3.19: Back, Front cover, and Two Different Adapter Tubes That Can be Mounted on The Front of a Manual Elbow.

Manual elbows have bigger mirrors (1.875in minor axis and with mirror mounts of $1.5 \times 1.5 \text{in}^2$) that are made in the same way the primary mirrors were. The $1.5 \times 1.5 \text{in}^2$ mounts can be found in many places in the detector including the Optics Box. Such elements must be mounted on straight mounts as portrayed in Figure 3.20. Only two

screws are used to hold the mount to the elbow's body to make dismounting the mirror easier especially during first time system assembly.

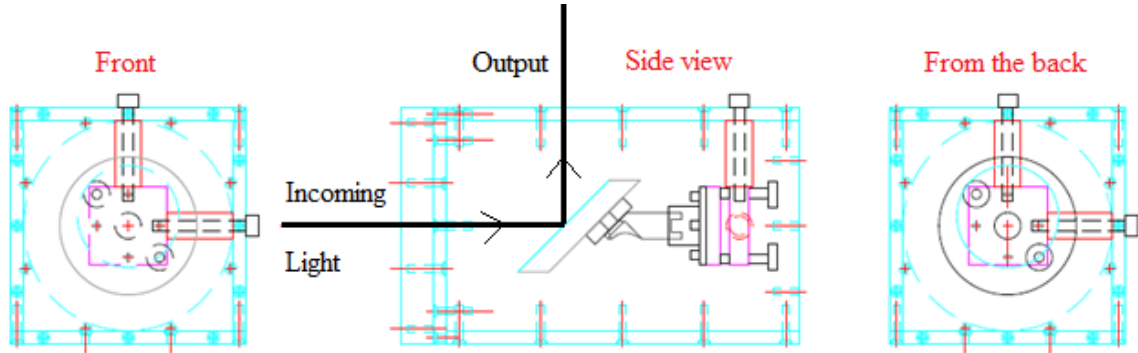


Figure 3.20: An Elliptical Flat Mirror on a Mount inside a Manual Elbow Reflecting Light

Because square pipes of $4 \times 4 \text{in}^2$ dimensions are not commercially available, these boxes were machined and made by welding aluminum pieces together. As a result, the aluminum becomes dirty and needs to be sandblasted. Thus, all manual elbows were cleaned and their surfaces were made rough through sandblasting so that they can be easily anodized as shown in Figure 3.21.

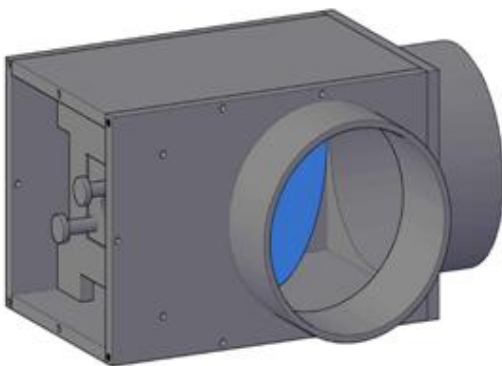


Figure 3.21: A Sandblasted Manual Elbow (Left), A Black Anodized Finished Elbow (Right)

3.7 Optics Box

The optics box is the core of the LABM, an enclosure of $(18 \times 24 \times 44)$ in³ made out of 0.125in black anodized aluminum plates. It is located at the end of the Optical Channel. It is designed to include and protect all other optical elements including Wollaston prisms, reflecting mirrors, ruled diffraction gratings, prisms-lenses arrays, a conveyor belt, arrays of photomultiplier tubes (PMTs) and their mu-shields, and two electronic circuit boards, as shown in (Figure 3.1). Two optics boxes, one for each beam, were produced. Each Optics Box observes both upper and lower viewports, and is composed of two Optical Benches (Figure 3.22).

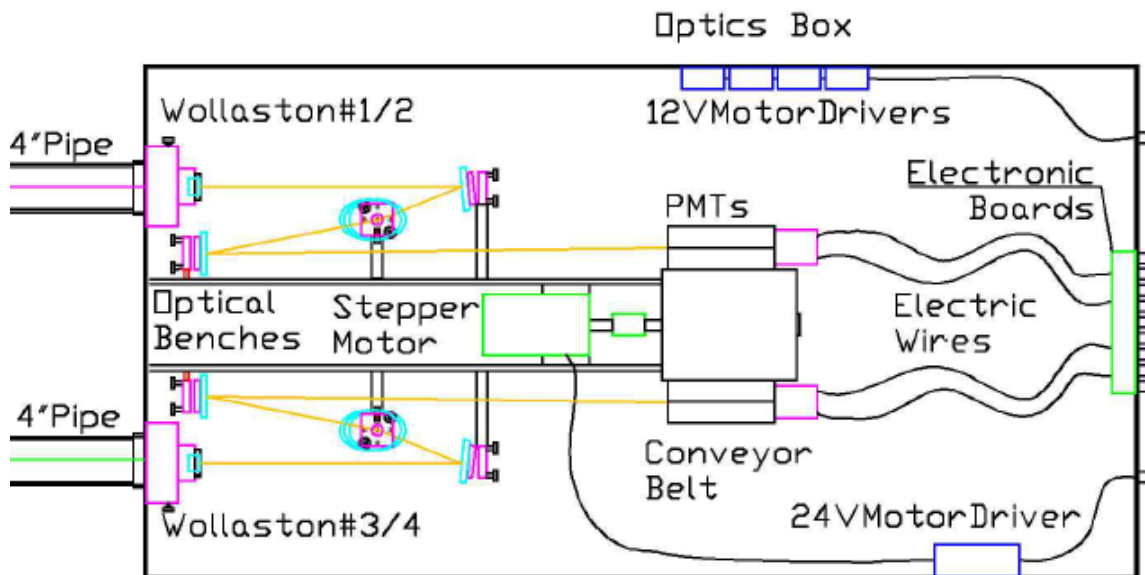


Figure 3.22: The Optics Box and Its Constituents, Side View.

The front view of the Optics Box, showing the two entry windows for the radiation are shown in Figure 3.23.

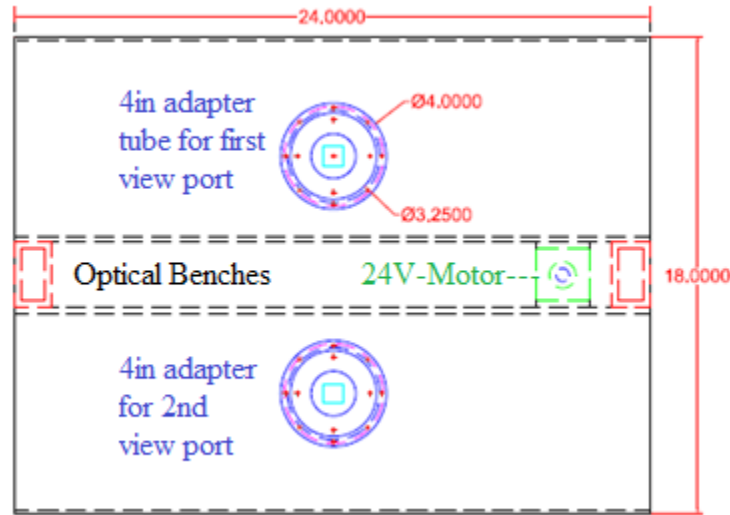


Figure 3.23: Front View of Optical Box

3.7.1 Wollaston Prisms

The first optical element, located at the very entrance of the Optics Box, is a Wollaston prism. Wollaston prisms provide polarization information about any incoming not polarized beam as depicted in Figure 3.24. A Wollaston consists of two identical prisms glued to one another base to base. The prisms used in this detector are $\frac{3}{4} \times \frac{3}{4} \times \frac{1}{2} \text{in}^3$. They are encased in a manual precision rotator that can be locked into position after alignment.

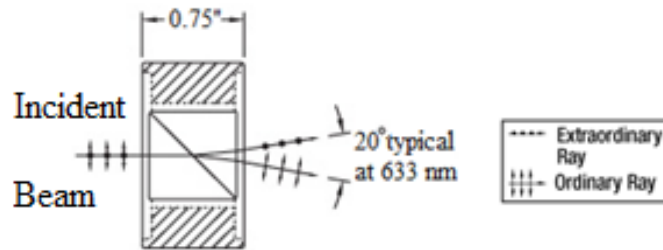


Figure 3.24: Wollaston Prism Splitting One Beam into Two Orthogonally Polarized Beams.

The Wollaston prism is also called the beam polarizer or splitter because it splits all incoming non-polarized light into two orthogonally polarized beams, one along the x and another along the y. The polarization parallel to the mid-plane is also called the extraordinary one; the other one is called the ordinary polarization. Both prisms are mounted on the inside of the front of the Box (Figure 3.25).

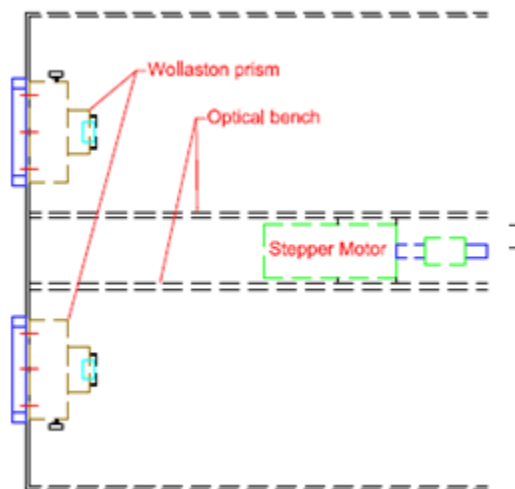


Figure 3.25: In This Optics Box Side View Wollaston Are Symmetrically Installed on the Front

3.7.2 Ruled Diffraction Gratings

Ruled diffraction gratings are used to decompose a polychromatic beam of light into its component wavelengths. These gratings are used because they, unlike all other types of gratings, have the highest intensity in the first order peak. Because the first peak angle depends on wavelength, optimal efficiency is obtained while spreading the light in angle according to the grating formula:

$$m\lambda = d[\sin(\theta) \pm \sin(\theta')] \quad (3.1)$$

Where m is the order of diffraction, λ is the diffracted wavelength, d is the grating constant which can be calculated out of the number of grooves of the grating, θ and θ' are the incident and the diffracted angles, respectively.

A ruled diffraction grating can be depicted in Figure 3.26 and the investigation of gratings efficiencies were done and reported in Chapter 4.

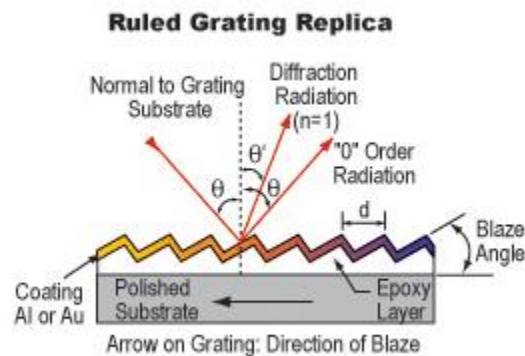


Figure 3.26: Ruled Diffraction Grating Schematic and Angle Definition.

To choose a diffraction grating that meets all diffraction specifications, the number of grooves per millimeter and blaze angle which determine the specific wavelength at maximum efficiencies (400nm to 800nm) according to the formula given in equation

(3.1) must be carefully chosen. The efficiency of such a grating can be determined at the nominal frequencies from the efficiencies plots shown in Figure 3.27.

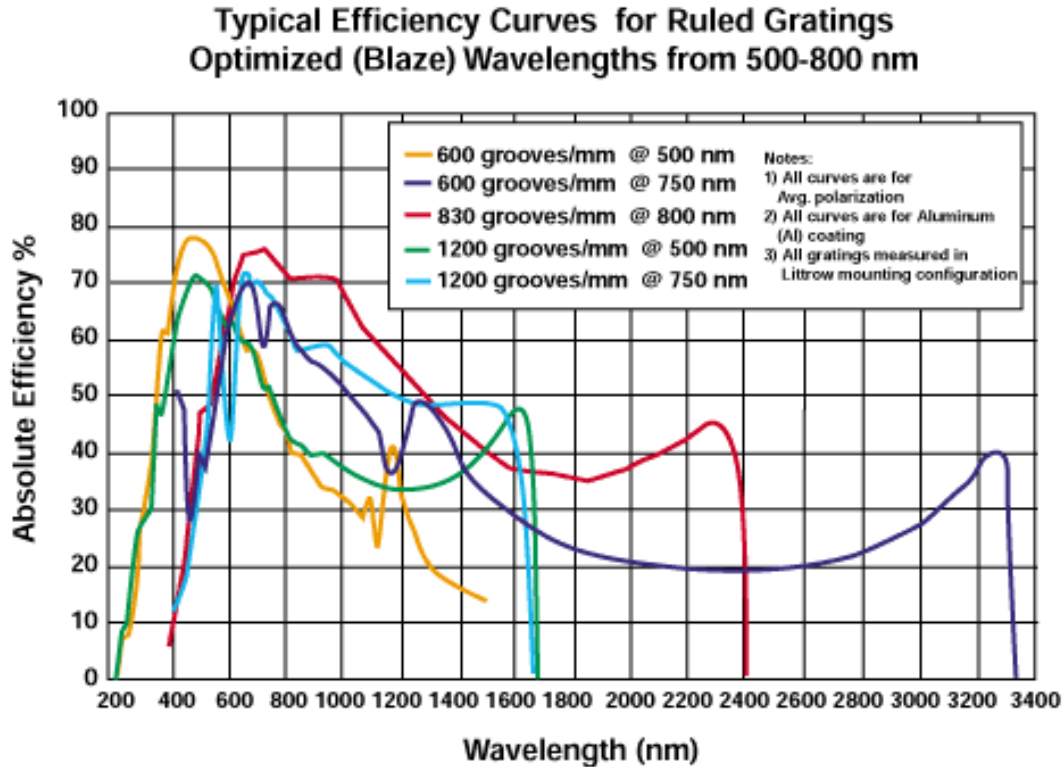


Figure 3.27: Efficiency Curves for Ruled Gratings at Various Wavelengths

It is clear that from the above a ruled grating with 600grooves/millimeter would be the best option due to its maximal efficiency (78%).

In regard to the size of the grating, $2 \times 2 \text{in}^2$ was chosen. The beam size ($0.8 \times 0.8 \text{mm}^2$) could be contained in a smaller grating, but it is desirable to contain also diffraction fringes. All ruled gratings are mounted on a straight $1.5 \times 1.5 \text{in}^2$ manual mount that is fixed on the Optical Bench via screws as shown in Figure 3.28. The mount position can be adjusted, facilitating alignment.

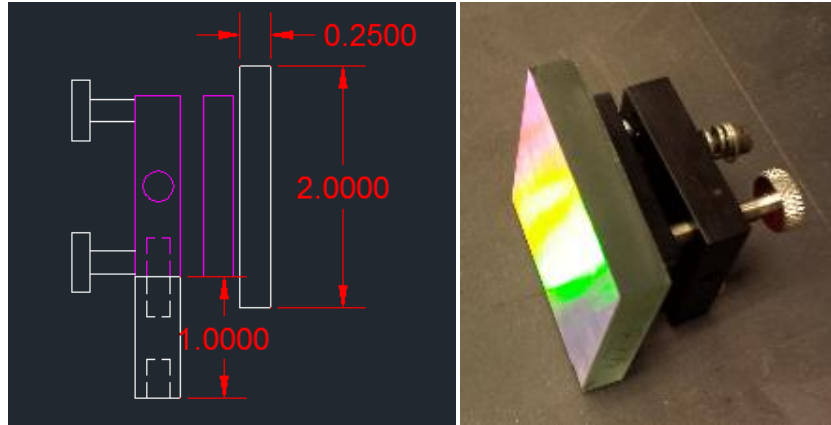


Figure 3.28: Left: 600 Grooves/mm Ruled Diffraction Grating Design, Right: Photo of Gratings/Mount Assembly.

3.7.3 Optical Benches

Each Optics Box contains two Optical Benches, one per viewport. Each Optical Bench is divided into two symmetric parts, each analyzing one polarization component. Each part contains one ruled diffraction gratings, two identical reflecting mirrors, and one set of four different prism-lens light collectors. The Benches are separated by a distance of 3.9375in allowing the stepper motor of the conveyor belt to rest in between them. Reflecting Mirrors are used to reflect light inside the optics box from the Wollaston prisms toward the gratings and to change the reflection plane from that of the prism to that of the gratings.

Gratings have to be coplanar with photomultipliers carried by the conveyor belt. As the ruled gratings were chosen to have high efficiency in the frequency domain, also mirrors have to be chosen the same way. Mirror efficiency measurements are reported in Chapter 4. All mirrors have the same size of 1.875in and 2.652in minor and major axis, respectively, and the same coating (UV enhanced aluminum) as the Optical Channel

mirrors. For fine adjustment purposes, they are mounted on $1.5 \times 1.5 \text{ in}^2$ manually movable mount which is mounted on a post of $\frac{1}{2} \text{ in}$ diameter being fixed on the optics bench through screws as shown in Figure 3.29.

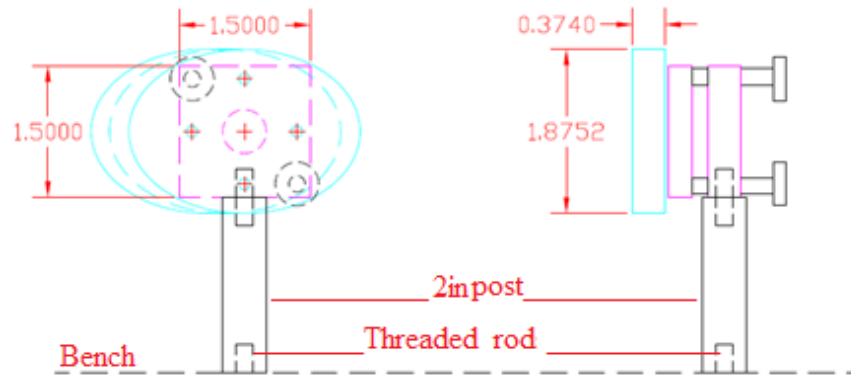


Figure 3.29: Elliptical Mirror Mount.

Positions as well as orientations of mirror are critical and were chosen so that a polarized beam after two reflections on the mirrors hits the diffraction grating and gets decomposed. The positions shown on the schematic are not random, but rather were picked by a computer program estimating all possible positions on a lattice and shown in Figure 3.30.

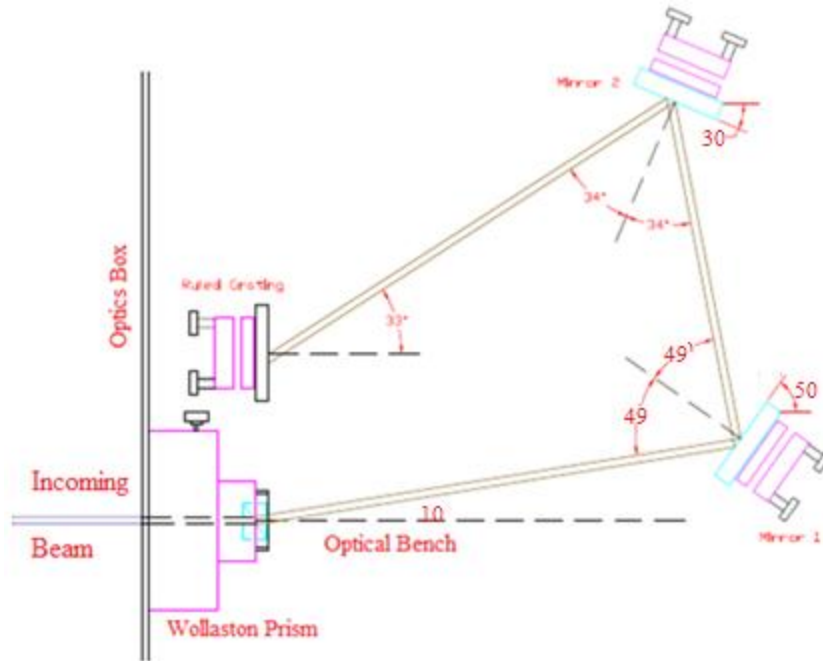


Figure 3.30: Half Optical Bench Schematics.

3.7.4 Light Collectors Motivation, Design, and Failure

The idea behind inventing light collectors was to accumulate all diffracted bandwidths of light coming from the gratings and have them focused at one point located at the front of photomultipliers so that they can receive all diffracted wavelengths within the same packet. A light collector is a 5in long dark object that has a truncated shape at 5deg angle from inside where four reflecting surfaces are placed as depicted in Figure 3.31.



Figure 3.31: A Light Collector from Side (Left) and Front (Right) Views

The aperture in the front is a square window of 8.43cm^2 through which a bandwidth of light can get inside the light collector. The back window however is a small square window of 0.16cm^2 allowing light, after being collimated, to get out through it after multiple reflections inside the light collector. Thus, in front of each grating there was an array of four light collectors to focus light of different frequency ranges.

Table 4 shows the optimal frequency range received by each light collector.

Light Collector Top	#1	#2	#3	#4
Frequency range (nm)	650 – 585	597- 498	510 - 410	419 – 350
Light Collector Bottom	#5	#6	#7	#8
Frequency range (nm)	350 - 422	410 - 513	499 - 600	588 – 650

Table 4: Eight Light Collectors and Their Corresponding Bandwidths

Light collectors tested poorly; as a result, they were replaced.

3.7.5 Prisms-Lenses system:

Since light collector failed, an optical correction piece was designed using prisms and lenses glued together. It is obvious that a prism with a proper angle can be used to align the rays parallel to its base. Then a lens focuses the rays into a small spot on the PMT. Thus, the problem was with what prism's angle(s) and what focal distance should be considered. Regarding the focal distance, the chosen focal length is 15cm since the PMT is 12.5 cm away (incomplete focusing is obtained, but the PMT longevity will improve when light is somewhat spread out on the photocathode) as shown in Figure 3.32.

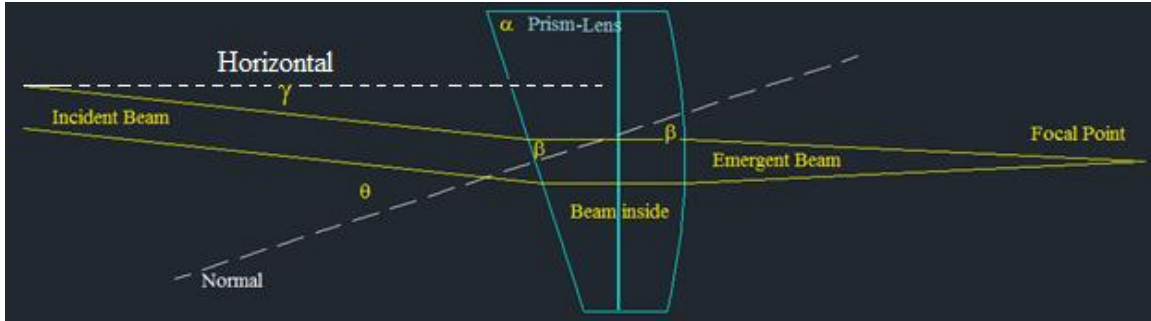


Figure 3.32: Light Path through a Prism-Lens Optical System

The diagram shows the incidence angle (θ) of a beam at the air-prism interface, the refracted angle (β) inside the prism of an angle (α), (γ) is the refracted angle given by the ruled diffraction grating with respect to the horizontal, and finally the emerging beam being focused at the converging lens focal point located at 15cm away as mentioned earlier.

The above schematic facilitates using Snell's law to determine the prism's angle as follows with n_1 is the index of refraction of air and n_2 is that of the prism.

$$n_1 \sin(\theta) = n_2 \sin(\beta) \quad (3.2)$$

But $\beta + \alpha = \frac{\pi}{2}$; Equation (3.2) becomes:

$$n_1 \sin(\theta) = n_2 \cos(\alpha) \quad (3.3)$$

Since γ is known and from the geometry of the problem, θ can be expressed in terms of γ and α as follows:

$$\frac{\pi}{2} - \theta + \gamma + \pi - \alpha = \pi \quad (3.4)$$

$$\theta = \frac{\pi}{2} + \gamma - \alpha \quad (3.5)$$

Substituting θ back in Equation (3.3):

$$n_1 \cos(\gamma - \alpha) = n_2 \cos(\alpha) \quad (3.6)$$

$$n_1 \cos(\gamma) \cos(\alpha) + n_1 \sin(\gamma) \sin(\alpha) = n_2 \cos(\alpha) \quad (3.7)$$

$$\sin(\alpha) = \sqrt{(1 - \cos^2(\alpha))} \quad (3.8)$$

$$(n_1 \cos(\gamma) - n_2) \cos(\alpha) = -n_1 \sin(\gamma) \sin(\alpha) \quad (3.8)$$

$$(n_1 \cos(\gamma) - n_2)^2 \cos^2(\alpha) = n_1^2 \sin^2(\gamma) (1 - \cos^2(\alpha)) \quad (3.10)$$

$$\cos^2(\alpha) (n_1^2 \cos^2(\gamma) + n_2^2 - 2n_1 n_2 \cos(\gamma) + n_1^2 \sin^2(\gamma)) = n_1^2 \sin^2(\gamma) \quad (3.11)$$

$$\cos(\alpha) = \frac{n_1 \sin(\gamma)}{\sqrt{n_1^2 + n_2^2 - 2n_1 n_2 \cos(\gamma)}} \quad (3.12)$$

Where $n_1 = 1$ and $n_2 = 1.55$. Finally and after all substitutions and solving for the prism's angle alpha:

$$\alpha = \cos^{-1} \left(\frac{\sin(\gamma)}{\sqrt{1 + 1.55^2 - 2 * 1.55 \cos(\gamma)}} \right) \quad (3.13)$$

Because each ruled grating is intended to diffract each polarized light into four different wavelengths (Red-Green-Blue-UV), four different incidences would be obtained and four different prisms are required and used along with the same converging lens since all PMTs are located in the same plane.

Solving the formula obtained in (3.13) for different diffraction angles and for both polarizations at different wavelengths, results of typical prisms angles can be tabulated in Table 5.

Wavelength $\lambda(\text{nm})$	Parallel/Perpendicular Polarization	
	γ (deg)	$\alpha(\text{deg})$
350	10.3	72.4
405	6	79.3
431	4	82.7
500	-0.8	88.6
532	-3.3	84
635	-10.5	72.1
650	-11.6	70.6

Table 5: Various Prisms Angles vs. Different Angles of Incidence

To replace the useless light collectors, two sets of four different prism-lens optical elements of angles 72, 75, 82, and 90 degrees can be determined from the above table satisfying the requirements and receiving all four bandwidths mentioned in previous the section.

The maximal polarized efficiencies of the prism-lens can be theoretically calculated using Fresnel equations [14] at different interfaces the new element separating indices of same magnetic permeability μ of:

$$t_{\parallel} = \frac{2n_1 \cos(\theta_i)}{n_1 \cos(\theta_i) + n_2 \cos(\theta_t)} \quad (3.14)$$

$$t_{\perp} = \frac{2n_1 \cos(\theta_i)}{n_1 \cos(\theta_t) + n_2 \cos(\theta_i)} \quad (3.15)$$

Where θ_i and θ_t represent the incidence and the refracted angle at an interface between two media of respective index of refraction n_1 and n_2 . It should be noted that

only the refracted relative amplitudes t_{\parallel} and t_{\perp} are recalled because only the polarized transmitted efficiencies would be points of interest.

The transmission coefficients at an interface in both cases can be written as:

$$T_{\parallel} = \frac{n_2 \cos(\theta_t)}{n_1 \cos(\theta_i)} |t_{\parallel}|^2 \quad (3.16)$$

$$T_{\perp} = \frac{n_2 \cos(\theta_t)}{n_1 \cos(\theta_i)} |t_{\perp}|^2 \quad (3.17)$$

The transmission coefficients become after using the new variables ρ and m defined below:

$$\rho = \frac{n_2}{n_1} \text{ and } m = \frac{\cos(\theta_t)}{\cos(\theta_i)}$$

$$T_{\parallel} = \rho m |t_{\parallel}|^2 = \frac{2}{m + \rho} \quad (3.18)$$

$$T_{\perp} = \rho m |t_{\perp}|^2 = \frac{2}{1 + \rho m} \quad (3.19)$$

Referring to Figure 3.32 and from the final expressions of both transmission coefficients, calculations can be performed four times (4 prisms) at four different interfaces: Air-Glass (A-G), Glass-Glue (G-GL), Glue-Glass (GL-G), and finally Glass-Air (G-A). The index of refraction of glue is 1.56.

Solving equation (3.2) for the incidence angle at the first interface of each prism assuming that the refracted ray normally strikes all other interfaces, Table 6 shows all necessary calculations:

Prism Angle	θ_i (deg)	Interface								Transmittance(%)	
		$A - G$		$G - GL$		$GL - G$		$G - A$		T_{\parallel}	T_{\perp}
		ρ	m	ρ	m	ρ	m	ρ	m		
86	6.207	1.55	1.003	1.006	1	0.994	1	0.645	1	91.0	90.8
84	9.324		1.008		1		1		91.1	90.8	
75	23.651		1.054		1		1		91.9	89.8	
72	28.619		1.083		1		1		92.4	89.2	

Table 6: Total Transmitted Coefficient of All Prisms-Lenses

Only the total transmittance is shown in the table since it can be easily shown to be equal to the multiplication of all transmittance coefficients at all interfaces.

As explained previously, these prisms allow light to internally strike the lens normally so that all rays converge towards the focal point of the likely lens and eventually to the corresponding PMT as shown in Figure 3.33.

The dashed lines of different colors represent the ideal incident diffracted rays off the ruled diffraction gratings on both sides of the optical bench. Notice the symmetric structure of both sides' components which compatible with that of the PMT's on the conveyor belt as detailed in the next section.

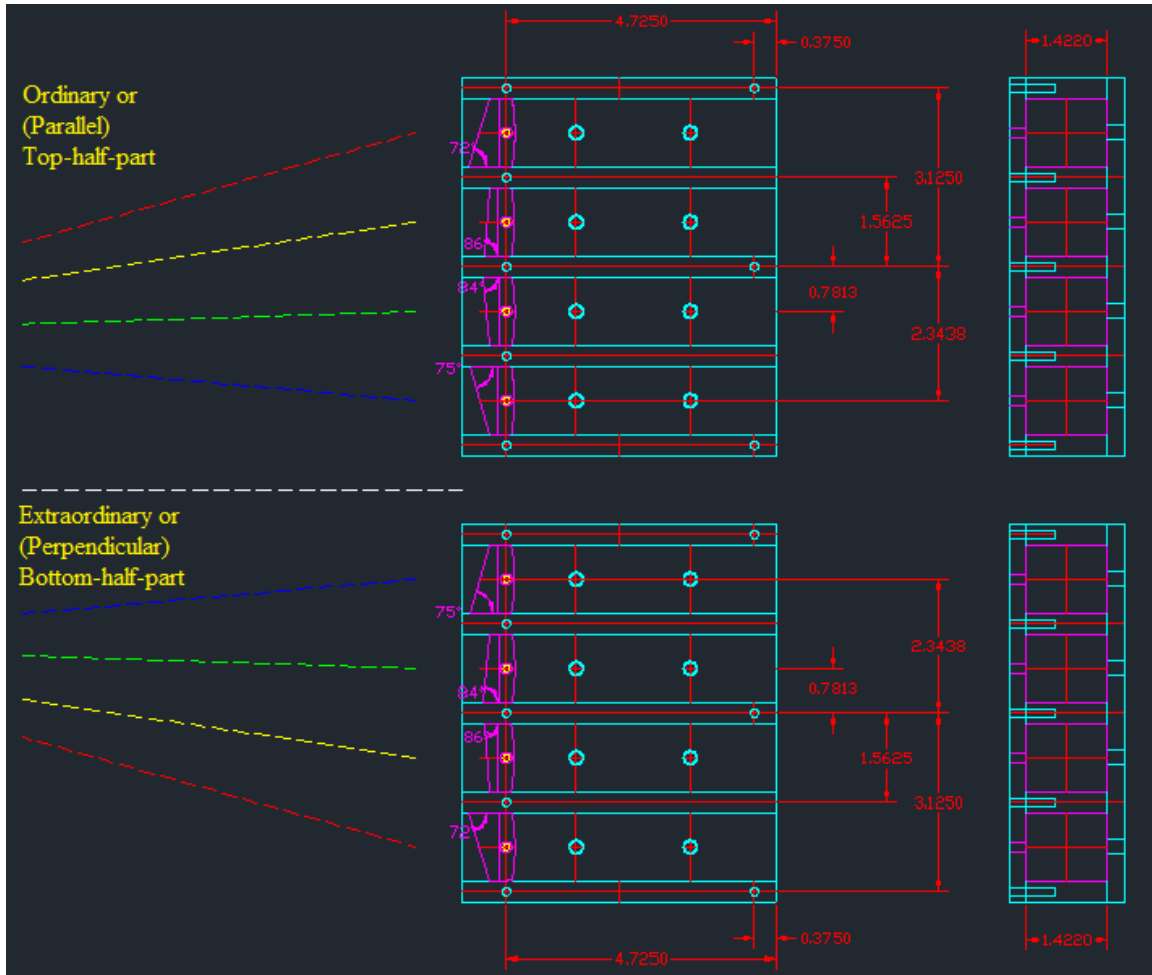


Figure 3.33: Array of 8 Prisms-Lenses Collection Mounted in Their Frames and Facing PMTs

3.7.6 Conveyor belt and its stepper motor

The purpose of the conveyor belt is to allow online swapping of the PMTs, to obtain precise relative efficiency measurements. The stepper motor is a 24V-2A stepper motor. The conveyor belt has 5in width. This conveyor belt dimensions were chosen that way because it needs to carry sixteen photomultipliers, each observing a viewport, as depicted in Figure 3.34.

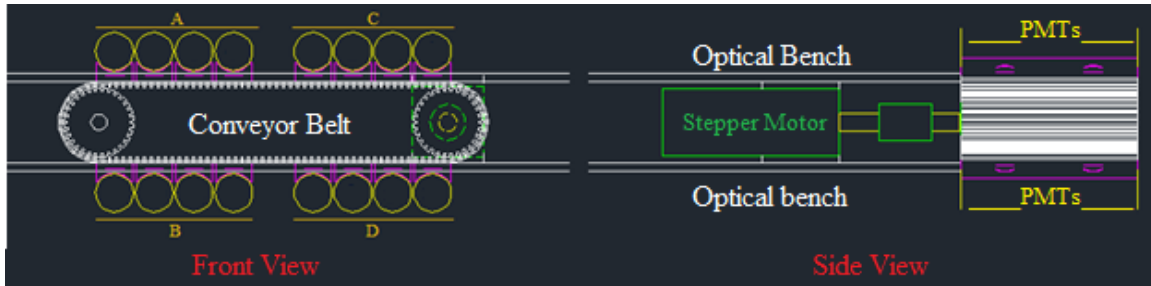


Figure 3.34: Front and Side Views of Conveyor Belt Carrying 16 PMTs

The eight photomultipliers on top in Figure 3.33 observe the top Optical Bench, four each for the x and y-polarization (A for x-polarization and C for y of the top view port). Likewise, the set of eight at the bottom is for the other Optical Bench (B for x-polarization and D for y of the second view port). The conveyor belt, when rotated by the stepper motor which is remotely controlled via computer, moves all PMTs around giving all possible measurements of x and y polarizations of the same beam and/or different beams, yielding a matrix of measurements that can be used to measure relative efficiencies. All PMTs can be calibrated and characterized inside the Box.

This conveyor belt is controlled by a PC through a serial port. The controller has a memory that saves programs in it, and it can be accessed from a Windows terminal. To view the programs saved into the memory or to run a control program, a protocol must be followed as it was tested (explained in Chapter IV).

3.7.7 Photomultipliers Definition and Applications

A PMT is a glass tube. On the face receiving the light, it has a very thin (few atoms) cesium compound layer coated inside it; as it gets illuminated by an incident photon, it emits one electron via photoelectric effect, with probability of 20% or lower ($3e^{-}$),

towards the facing anode or dynode as shown in Figure 3.35. The inside of the PMT is held at vacuum.

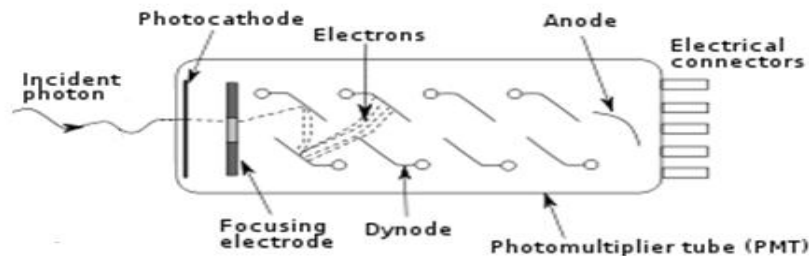


Figure 3.35: Photomultiplier and Photoelectric Effect Principle

The first dynode, struck by an electron with kinetic energy of order 100 eV, will emit on average about 3 electrons. The phenomenon continues from one dynode to the next, which results in a significant electric current on the last anode in the order of milliamperes (mA). Since the electron trajectories inside the PMT are sensitive to magnetic fields, the photomultiplier should be covered with a high permeability material. This is called μ -shielding. Because the current or signal obtained by a PMT is still difficult to detect, it could be amplified before discrimination and counting.

3.7.8 Electronics and Back plate

This piece of hardware has two roles: one to cover the box from the back, and two to support the electronic board that is consisted of amplifiers, discriminators, high voltage sockets, and output terminals for counting. The electronics is being developed in Mexico. Here only the back panel, which brings HV cables in and signal cables out, is discussed and shown in Figure 3.36.

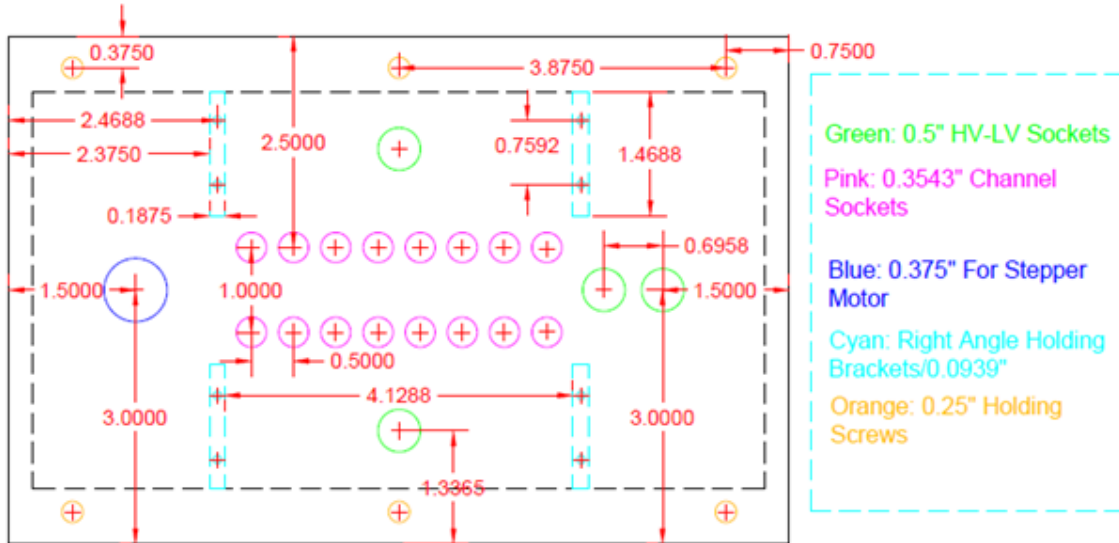


Figure 3.36: Design of the Back Panel.

The back-panel also feeds through the stepper motor cable. This produced back panel shown in Figure 3.37 will be embedding all electronics from Mexico and replacing the old electronics.

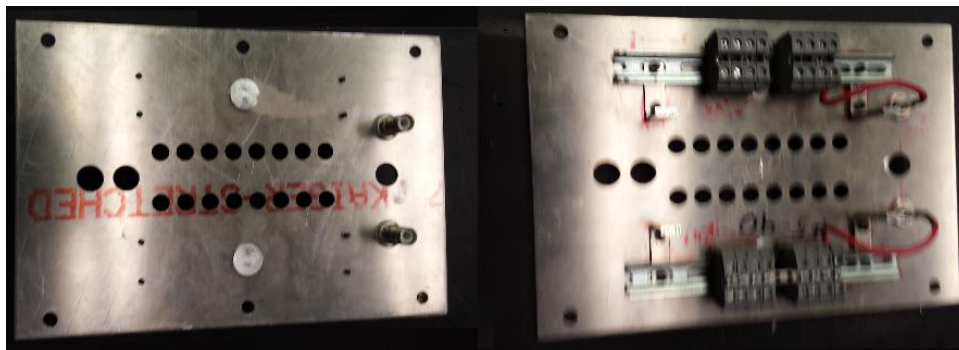


Figure 3.37: High Voltage Sockets (Left) and Rails (Right) on the Back Plate

3.8 The Old Electronics Setup

The old electronics setup consists of a high voltage power supply to power up 8 PMTs at a time, 8-channel amplifiers of gain 10 each, discriminators where signal

selections take place, and digital readouts to visualize the number of photon counts. The crate and its component are shown in Figure 3.38.

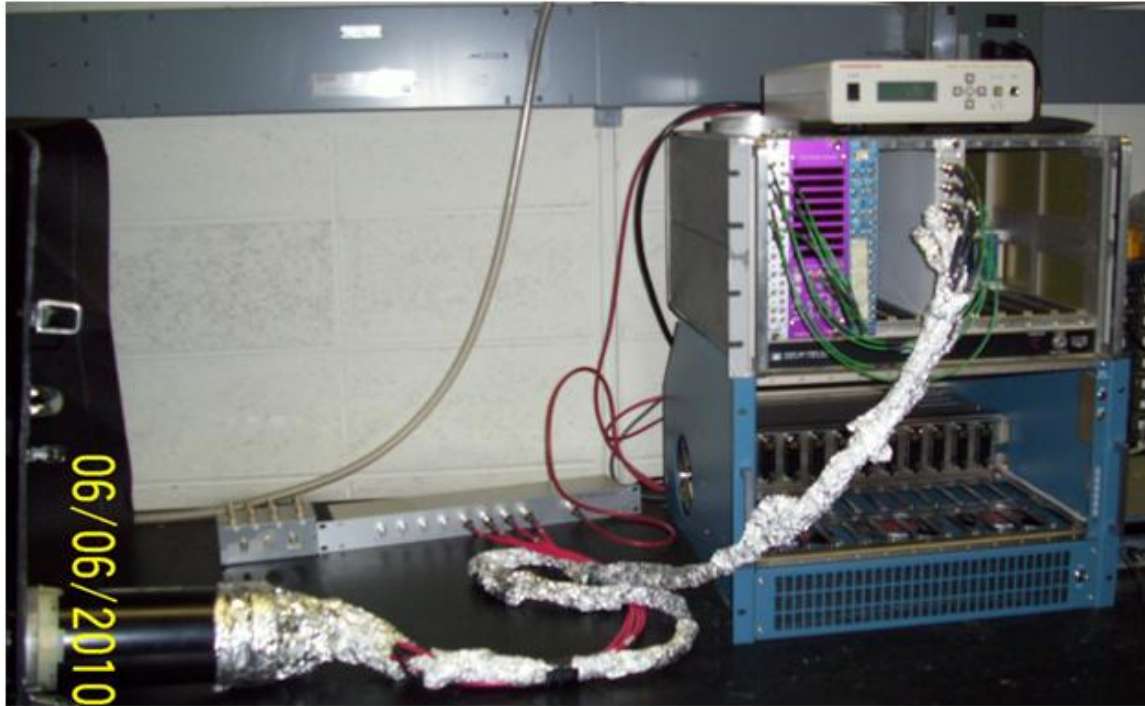


Figure 3.38: Electronic setup

This setup played a big role in this research because it was used many times in performing all tests including PMTs' calibrations and characterizations. PMTs Characterization means determination of the dark noise or the background signal of each photomultiplier when there is no light inside the box.

Fortunately, the box was built to be dark enough and the background signal was measured by each PMT. However, calibration means determination of the PMT spectral response, plateau and operational voltage well as the threshold voltage of each PMT. Spectral response means studying how each photomultiplier acts at different frequencies of light.

3.9 Anodized Aluminum Box

Finally, all produced components and elements can be mounted inside the big optics box and would be enclosed and ready for use after testing as it will be explained in the next chapter. The real and final detector then looks like the one depicted in the below picture (Figure 3.39).



Figure 3.39: Anodized Assembled Optics Box Containing All Optical Components

Chapter 4 : Tests and results

4.1 Introduction

All drawings were approved, parts were produced, and components including mirrors of different sizes, ruled diffraction gratings, and Wollaston prisms were bought from different sources. This Chapter details the measurement of efficiencies of the various optical components, to be used for determination of the overall detector efficiency and spectral response.

4.2 Optics Box Composites Testing

All component were tested using a unique setup consisted of three different laser diodes (red of 632nm, green of 532nm, and purple of 405nm), two polarizers in series, a beam splitter, and two photometers as shown in Figure 4.1. The 50/50 beam splitter allows monitoring of the laser intensity, which fluctuated sometimes.

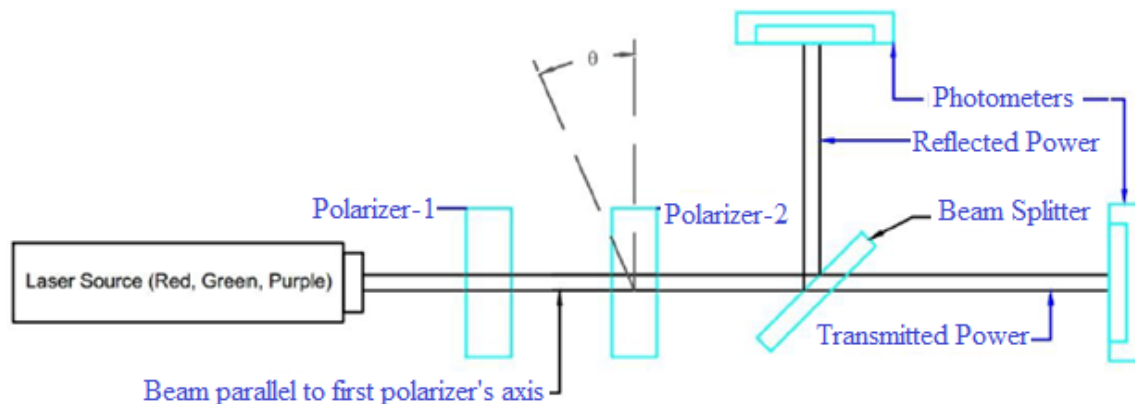


Figure 4.1: Setup Used to Test Optical Components Using Three Different Sources of Light

The two-polarizer arrangement can be understood by looking at the plots of Figure 4.2, which was obtained with a single polarizer. The red and purple laser appear to be made of mostly one main oscillator, whereas the green laser exhibits more, unequal oscillators resulting in a complex polarization pattern, but no laser is as unpolarized as needed for the uncertainties needed in these measurements, which should be better than 1%.

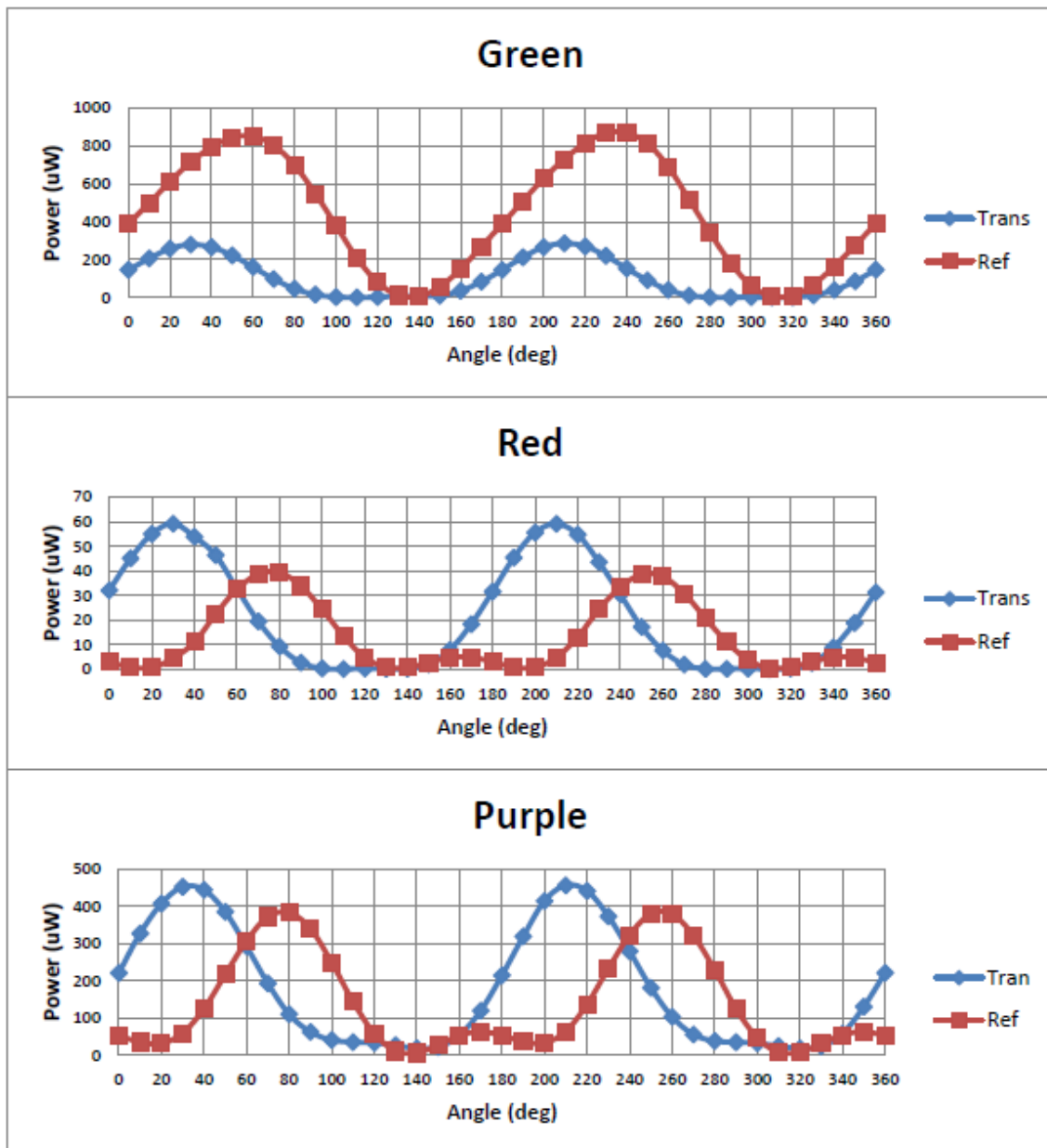


Figure 4.2: Reflected and Transmitted Powers of Two Daughter Beams at Different Frequencies as a Function of one Polarizer's Angle.

The first polarizer eliminates the structures in Figure 4.2, effectively allowing transmitted light that appears to originate from a single oscillator. The second polarizer, then, produces a sinusoidal intensity as a function of the two-polarizer's relative angle, θ

$$I(\theta) = I_0 \cos^2(\theta) \quad (4.1)$$

Where I_0 and I are respectively the intensities of light before and after second polarizer.

4.3 Wollaston Prisms

Characterization of Wollaston prisms means measuring polarizations efficiencies, and angles of emergence. This can be done by replacing the beam splitter of the previous stage by a Wollaston prism and by placing two photometers such that they measure the powers of the beams as shown in Figure 4.3.

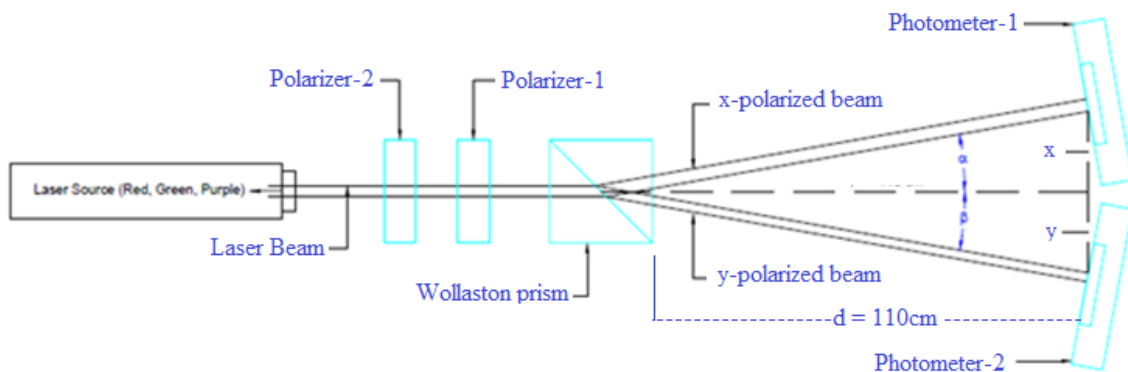


Figure 4.3: Wollaston Prism's Characterization Setup

With this setup, four identical Wollaston prisms were tested and deviation angles of each prism were investigated by measuring the vertical distances of both polarized

beams. Then, deviation angles were computed through the tangent inverse function of the vertical position of the corresponding polarizations (x and y) to the horizontal separation distance ($d = 110\text{cm}$) between prism and sensors as shown in Table 7. The angles α_i and β_i in the table represent the parallel and perpendicular deviation of both polarizations.

Ang(deg)	Wollaston							
Meas. Values	W_1		W_2		W_3		W_4	
	α_1	β_1	α_2	β_2	α_3	β_3	α_4	β_4
Purple	10.08	11.41	10.05	11.39	10.08	11.41	10.08	11.44
Green	9.57	10.78	9.57	10.76	9.57	10.76	9.55	10.73
Red	9.39	10.46	9.39	10.46	9.39	10.51	9.39	10.46
Theor. Values	α_1	β_1	α_2	β_2	α_3	β_3	α_4	β_4
Purple	10.12	11.24	10.12	11.24	10.12	11.24	10.12	11.24
Green	9.57	10.58	9.57	10.58	9.57	10.58	9.57	10.58
Red	9.36	10.33	9.36	10.33	9.36	10.33	9.36	10.32
Percent Difference (%)								
Purple	0.381	1.55	0.630	1.328	0.381	1.551	0.381	1.774
Green	0.004	1.89	0.004	1.653	0.004	1.654	0.260	1.416
Red	0.415	1.269	0.415	1.269	0.415	1.757	0.415	1.269
Average of Percent difference (%)								
Avg Blue	0.97		0.98		0.97		1.08	
Avg Green	0.95		0.83		0.83		0.84	
Avg Red	0.84		0.84		1.09		0.84	

Table 7: Measured Angle Spread of Four Wollaston Prisms at Different Wavelengths

The table also shows that all four prisms are actually identical to less than 0.1%.

From the below plots (Figure 4.4), it can be seen that the prism generates some chromatic dispersion. For example, in the upper beam red rays will be located in the bottom, green rays in the middle, and purple rays in the top of the beam. In the lower (extraordinary) beam the reverse is true. This difference is propagated through the optical

chain, leading to angular spreads (after the grating) slightly different from the theoretical values due to the grating alone.

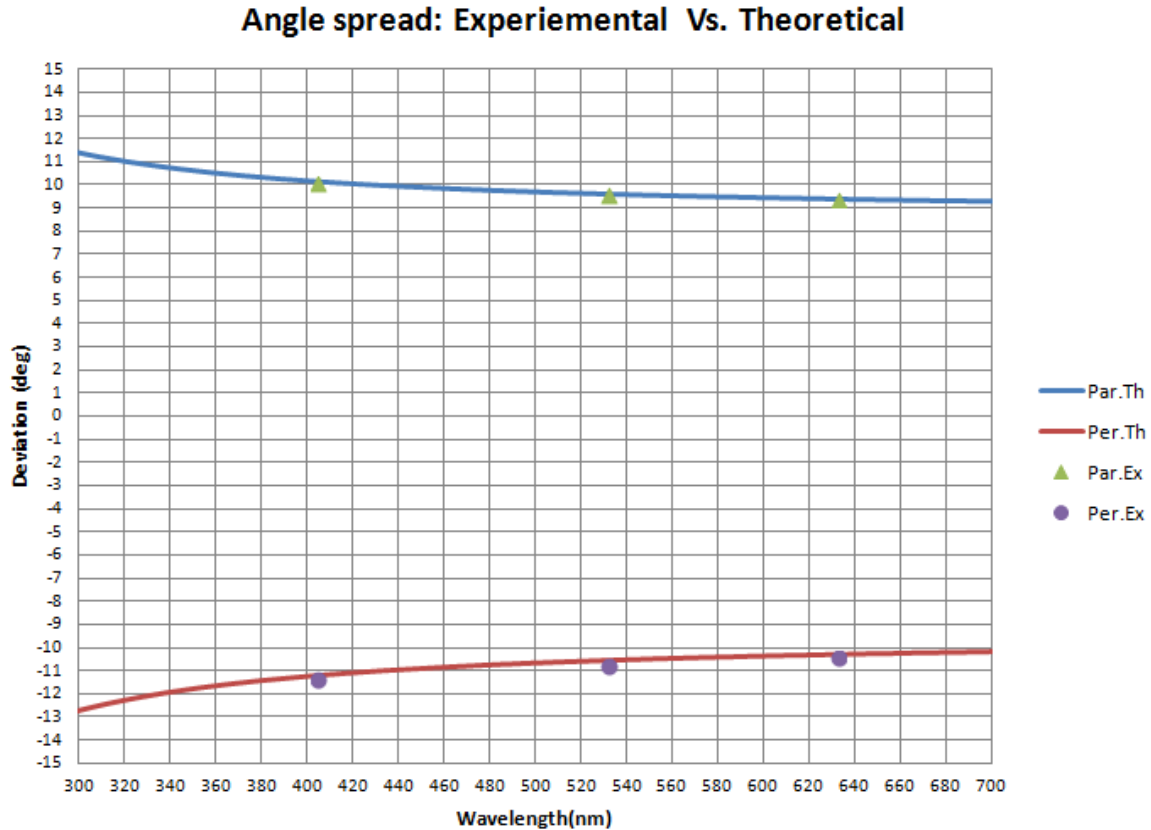


Figure 4.4: Beam Angular Deviation by Wollaston Prism vs. Wavelength

To measure the efficiency of a Wollaston or any optical element, the power of the incoming beam needs to be measured. Such an optical element's efficiency can be tested against each polarization and then the average efficiency can be estimated by averaging both results.

With the described setup, the power of the incoming beam (upfront of the element under test which is the Wollaston in this case) was measured using a photometer as

shown in the upper part of Figure 4.5. Another photometer was used to measure the transmitted power out of it as shown in bottom part.

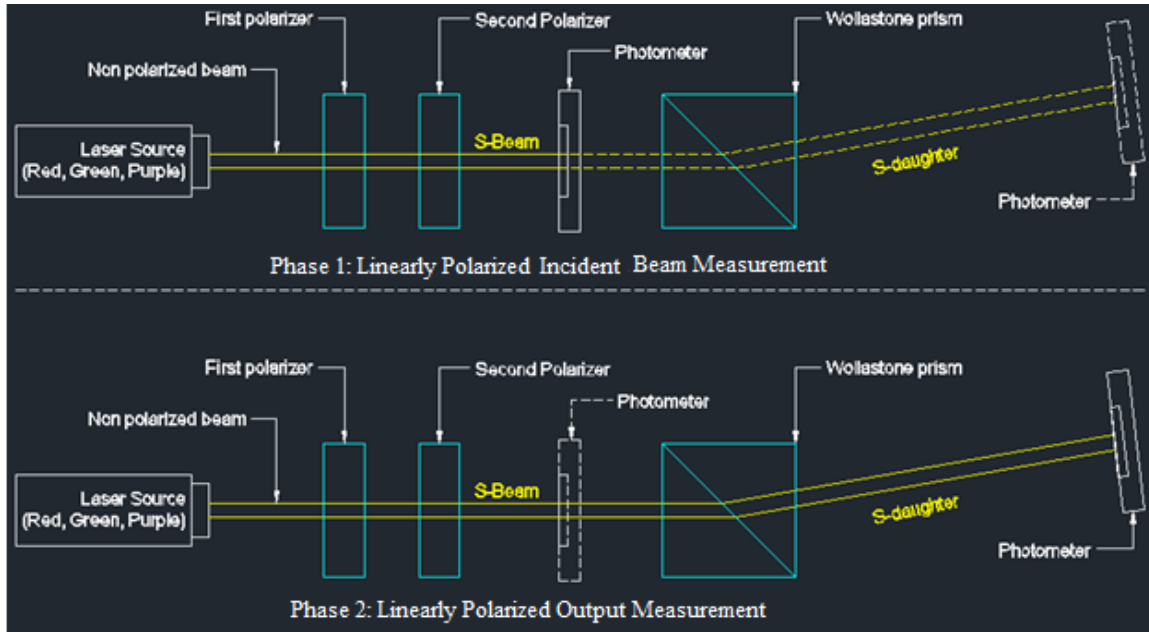


Figure 4.5: Schematic of Measuring Incoming (Upper) and Output Beams (Bottom)

The diagram only shows how the efficiency of such a prism can be determined under parallel polarization. The same technique was used to measure the other efficiency by rotating both polarizers 90deg from their original orientations to make sure a perfectly perpendicular polarization was obtained. In this case the P-daughter beam (not shown) will be reversed and received by the photometer being displaced down. Both efficiencies were recorded to provide the plots shown in Figure 4.6.

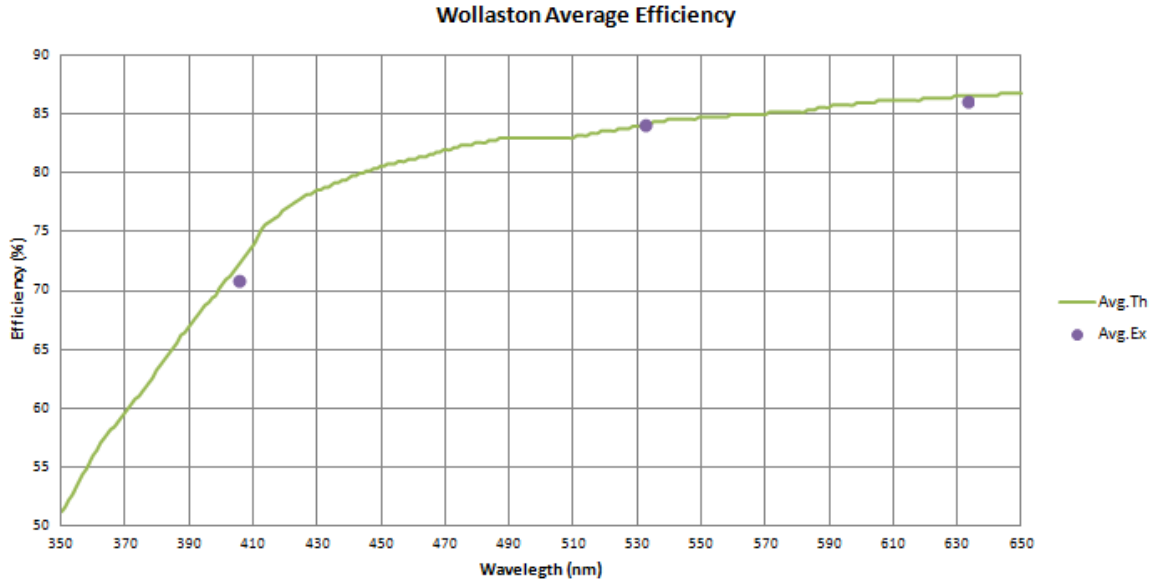


Figure 4.6: Wollaston Average Efficiency as a Function of Wavelength.

The above plots are for one Wollaston prism that was tested at different frequencies and different polarization angles. They also show that the average efficiency of a prism is obviously frequency dependent. Additionally, It was noted that that the average efficiency difference of a Wollaston between polarizations is about 1% which can be considered unaffected by the polarization type as Table 8 shows.

Wave-length (nm)	Parallel Polarization			Perpendicular Polarization			Average Eff(%)
	Input (uW)	Output (uW)	Eff (%)	Input (uW)	Output (uW)	Eff (%)	
405	1770	1260	71.19	1750	1235	70.57	70.88
532	1590	1345	84.59	1570	1315	83.76	84.17
633	441	382	86.62	481	413	85.86	86.24

Table 8: A Wollaston Efficiency Behavior vs. Polarization and Frequency

Also, when this prism was replaced by another one, similar results were obtained and the average efficiency versus wavelength was computed and tabulated in Table 9.

Wollaston	Red (%)	Green (%)	Violet (%)
W_1	85.07	82.79	71.14
W_2	84.55	81.88	70.72
%difference	0.61	1.09	0.59

Table 9: Two Wollaston Average Efficiencies vs. Frequency

Where W_1 and W_2 denote the two Wollaston prisms that were randomly chosen and tested. From the table, we show that two Wollaston are very similar to a percent difference of about 1% as the table shows. Hence, all prisms are identical and have the same efficiency at the corresponding frequency.

4.4 Elliptical Flat Mirrors

The efficiencies tests of gratings and mirrors were done using the same setup once against the ordinary beam and another against the extraordinary one. As usual, the second polarizer must be rotated so that identical power outputs were obtained at 45deg.

This method was performed twice to test the mirror against both polarizations. In this experiment two photometers were used: one facing the transmitted light another measuring the reflected light through the mirror; the other way around was also performed. The mirror was also mounted on a rotary station allowing a large domain of incidence varying from 5 to 85° at an increment of 5 degrees as shown in Figure 4.7.

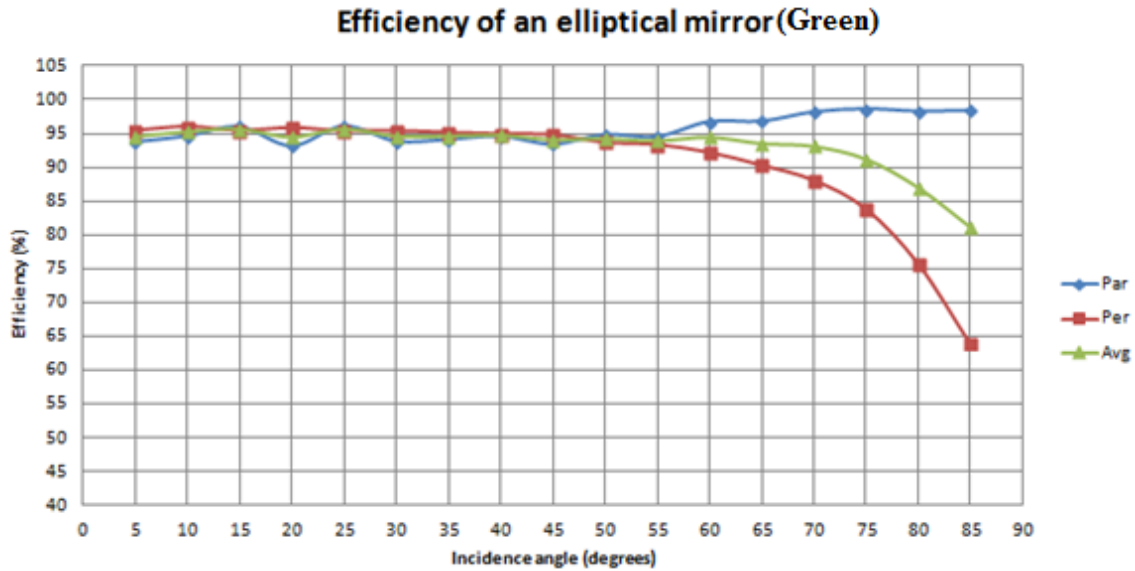


Figure 4.7: Elliptical Mirror's Efficiency vs. Incidence Angle

Illuminated by a green source, the average efficiency of such a mirror can be estimated to be about 94% for all angles less than or equal to 55 degrees which is accountable since the two reflecting mirrors inside the optics were to be oriented with respect to the incident beam at 30° and 50° , respectively. Others inside the elbows are at 45° . Above 55° , the mirror's reflectance changes significantly as angle increases: reflectance decreases under extraordinary and increases under ordinary polarization as shown above.

Knowing that the nominal orientation of mirrors would be about 45° , the mirror's polarized efficiency can be plotted at 45° against wavelength and then compared to the theoretical values calculated at the same angle. Both data can be plotted and shown in Figure 4.8.

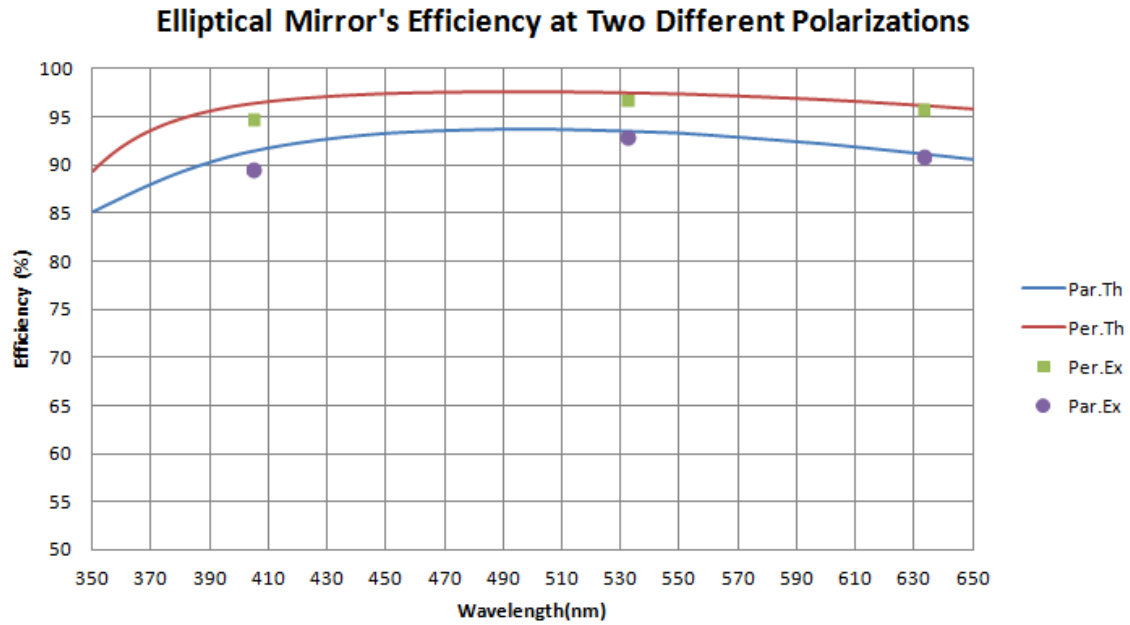


Figure 4.8: Polarized Efficiency of an Elliptical Mirror as a Function of Wavelength.

As expected, from the plots one would infer that such a mirror has a frequency dependent efficiency that is also changing from a polarization to another. The average efficiency of the mirror can also be plotted against various laser colors and shown in Figure 4.9.

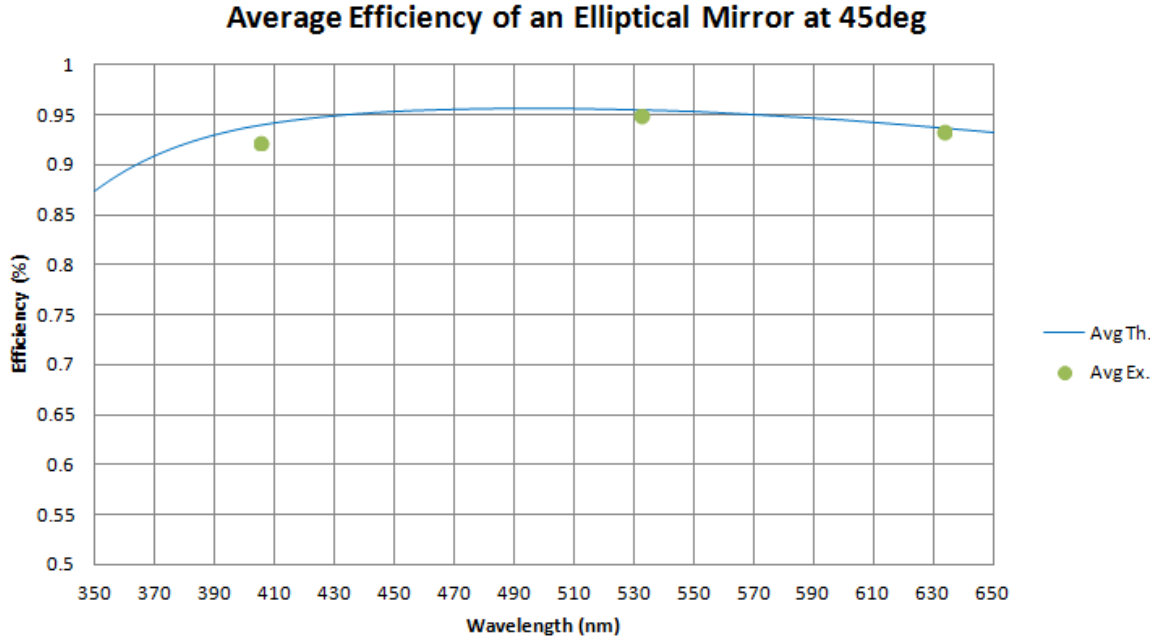


Figure 4.9: Elliptical Mirror Average Efficiency

After determining the efficiency of one elliptical mirror, three other mirrors were placed in the setup one at a time; measurements were taken under two different polarizations and average efficiency of each was calculated at different frequency and tabulated in Table 10.

Mirrors (45 deg)	Eff. Red (%)	Eff. Green (%)	Eff. Violet (%)
a ₁	93.12	94.99	92.82
a ₂	93.12	94.96	92.82
b ₁	93.12	94.97	92.82
b ₂	93.13	94.97	92.82

Table 10: Efficiencies of Multiple Elliptical Mirrors Using Three Different Sources

Where a₁, a₂, b₁, b₂ are just labels being placed on the mirrors to distinguish them. It can be concluded that all mirrors are in fact identical up to less than 0.1% difference.

Since all mirrors inside manual elbows are made similar to those inside the optics box but oriented at 45° , they should have an average efficiency of 93% each.

With the efficiency of each elliptical mirror being well determined, the total power reflected through five elliptical mirrors (four inside manual elbows and one inside primary elbow) and received by the Wollaston can be defined as:

$$P_w = (\epsilon_{Avg})^n P_0 \quad (4.2)$$

P_w , ϵ_{Avg} , and P_0 denote the power received by a Wollaston prism, the average efficiency of an elliptical mirror, and the initial power after the beryllium mirror inside the beam pipe. The n^{th} exponent in the equation is due to the fact that light suffers n outside reflections inside elbows and losing power. The integer n varies from a view port to another depending on the number of elbows ($n = 5$ and $n = 7$ for top and bottom view ports, respectively).

When light gets to the Wollaston prism, its power gets split into two with different efficiencies $\epsilon_{w\perp}$, $\epsilon_{w\parallel}$. After the Wollaston, the two daughter beams continue and meet two elliptical mirrors on their ways to the grating causing the presence of another exponent of two in the power expressions defined in equations 4.3 and 4.4, accordingly.

$$P_{G\parallel} = (\epsilon_{m\parallel})^2 \epsilon_{w\parallel} P_w = (\epsilon_{m\parallel})^2 \epsilon_{w\parallel} (\epsilon_{Avg})^n P_0 \quad (4.3)$$

$$P_{G\perp} = (\epsilon_{m\perp})^2 \epsilon_{w\perp} P_w = (\epsilon_{m\perp})^2 \epsilon_{w\perp} (\epsilon_{Avg})^n P_0 \quad (4.4)$$

$P_{G//}$, $P_{G\perp}$, $\epsilon_{m//}$, and $\epsilon_{m\perp}$, represent the parallel and the perpendicular powers received by the ruled diffraction gratings as well as the mirror efficiencies found at different polarizations.

4.1 Ruled Diffraction Gratings

In a similar way, the ruled diffraction grating's efficiency can be determined at different frequency and plotted as shown in Figure 4.10.

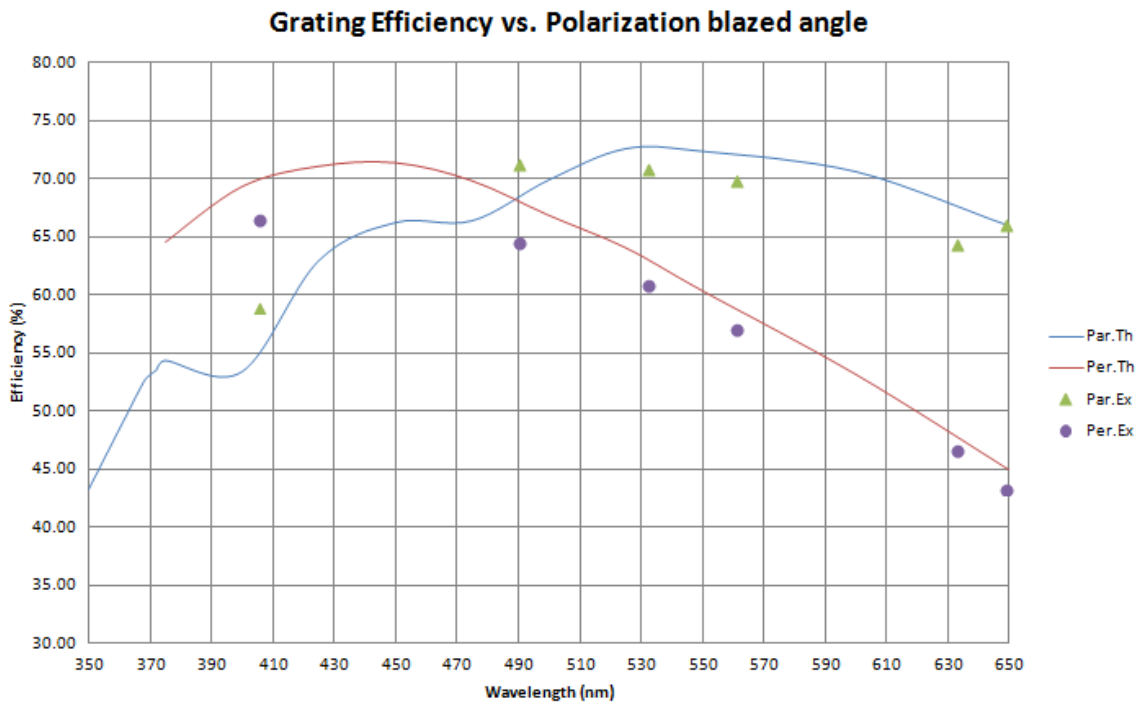


Figure 4.10: Grating Efficiency Curves for Both Polarizations.

Since all diffraction gratings are located inside the optics box where they receive either S-polarization or P-polarization, the average efficiency of such a grating was not needed to be determined. In a similar way, multiple gratings were tested and results were tabulated in Table 11. G1 and G2 denote for grating#1 and grating#2 respectively.

Perpendicular	Eff. Red (%)	Eff. Green (%)	Eff. Violet (%)
G1	47.78	60.65	69.65
G2	47.73	60.58	69.58
Parallel	Eff. Red (%)	Eff. Green (%)	Eff. Violet (%)
G1	57.70	65.05	70.16
G2	57.62	65.00	70.00

Table 11: Two Identical 600grooves/mm Gratings Efficiencies

As the table shows, the two gratings are very similar to a less than 0.1% and their efficiencies significantly change as the wavelength changes. From Fig. 4.10, it is evident that there are some unresolved issues in the grating efficiency which will be investigated in the next month.

The diffracted powers after the gratings can be then estimated by using the following formulas:

$$P_{f\parallel} = (\epsilon_{Gf\parallel}) (\epsilon_{m\parallel})^2 \epsilon_{w\parallel} (\epsilon_{Avg})^n P_0 \quad (4.5)$$

$$P_{f\perp} = (\epsilon_{Gf\perp}) (\epsilon_{m\perp})^2 \epsilon_{w\perp} (\epsilon_{Avg})^n P_0 \quad (4.6)$$

The new parameters introduced in these equations are $\epsilon_{Gf\perp}$, $\epsilon_{Gf\parallel}$ which represent the efficiencies after the gratings at different frequencies and different polarizations. The reminders, $P_{f\perp}$ and $P_{f\parallel}$, represent the polarized power emitted through each individual wavelength on each side of the optical bench.

4.2 Light Collectors

Light collectors were designed to collect light, spread out by the grating, into individual PMTs. They were designed and produced, but they failed testing and were replaced.

The measured light efficiency as a function of the light angle with respect to the collector axis is shown in Figure 4.11. Because collectors are at an angle of up to 10 degrees with respect to the incident light, this solution was discarded.

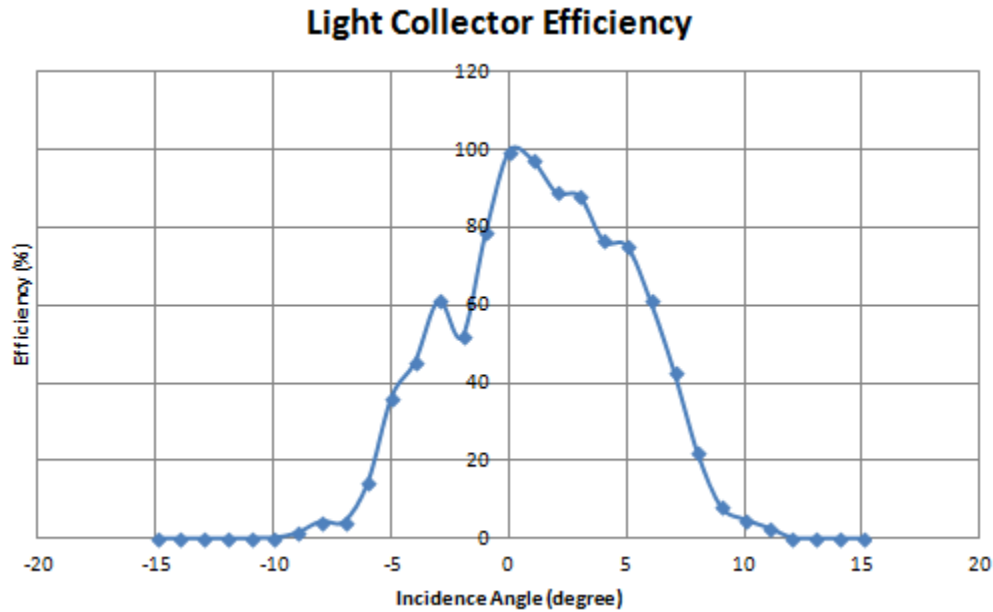


Figure 4.11: Efficiency of a Light Collector vs. Incidence Angle

The simplest explanation for the low efficiency is depicted in Figure 4.12. At larger angles, repeated reflections make the light angle larger and larger, until it exceeds 90 degrees and is reflected back instead of being transmitted.

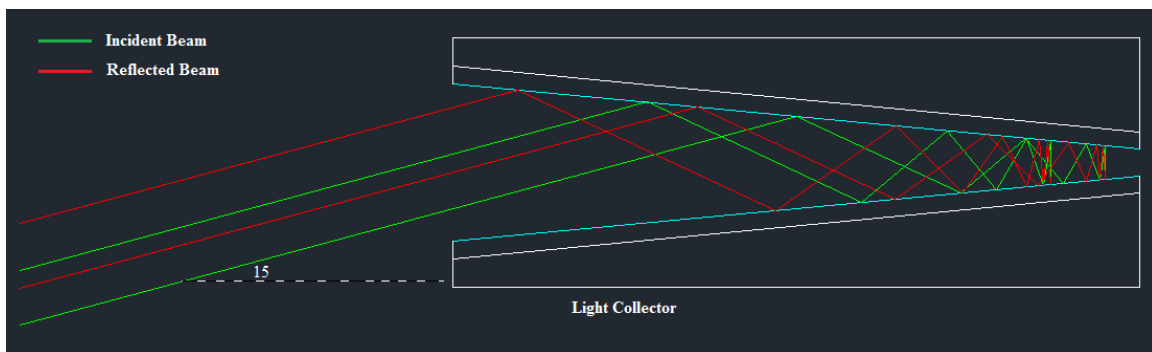


Figure 4.12: Light Paths inside a Light Collector at an Angle of 15 degree

It is clear from the diagram that the green incident beam after many reflections inside the light collector never escapes but rather reflected back (red lines). As a result, the light collectors were replaced by optical pieces consisting of a prism glued to a converging lens, as explained in Chapter III.

4.3 Prisms-Lenses Arrays

Since a new component was invented and made at Wayne State University, careful measurements needed to be collected and studied in order to validate and deny the use of such elements. This was done by using the same procedures as before and always under two orthogonal polarizations but at different angles of incidences that meet those in Table 6. Measurements were taken, reported and plotted in Figure 4.13.

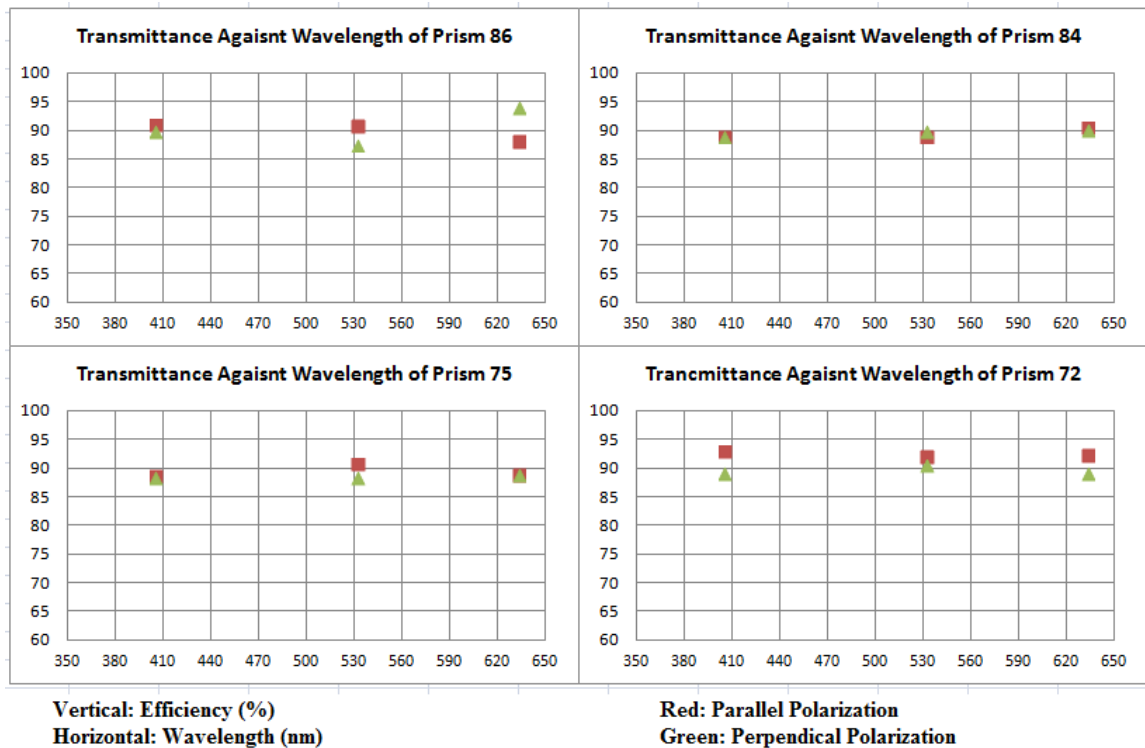


Figure 4.13: Prisms Efficiencies at Different Wavelengths

The charts show that the polarized efficiency of each prism is almost uniform indicating that they are frequency independent at least at the corresponding incident angles mentioned before. Before comparing the measured transmission coefficients against the theoretical ones, all polarized efficiencies of prisms were tested at the corresponding solid angle of the diffracted light given by the grating as Table 12 shows.

Prism	Parallel Polarization		Perpendicular Polarization	
	Eff at Max. Incidence	Eff at Min. Incidence	Eff at Max. Incidence	Eff at Min. Incidence
86	89.8	89.8	90.9	90.0
84	90.1	89.6	89.0	90.1
75	88.9	88.5	89.0	88.8
72	89.1	89.7	92.5	92.8

Table 12: Polarized Prisms Efficiencies within the Expected Light Cone

It is clear that efficiency does not change within the maximal and the minimal angle of the light cone striking the corresponding prism that is presumably oriented in properly in the array (see Fig. 4.25). Therefore, the average polarized transmission coefficient compared to that obtained in Table 6 of each prism is tabulated in Table 13.

Prism Angle	Experimental Coefficients (%)		Theoretical Transmittance (%)		Percentage Difference (%)	
	T_{\parallel}	T_{\perp}	T_{\parallel}	T_{\perp}	Par.	Perp.
86	90.45	89.8	91.0	90.8	0.6	1.1
84	89.85	89.55	91.1	90.8	1.4	1.4
75	88.9	88.7	91.9	89.8	3.2	1.2
72	92.65	89.4	92.4	89.2	0.3	0.2

Table 13: Experimental Coefficients vs. Theoretical

All data in the table confirm what is initially obtained in Fig. 4.13 and, therefore, the theoretical values can be accounted.

Referring to Fig. 3.33 especially after the prisms-lenses arrays, the expression of the power received by each PMT differs from one to another and can be calculated out of equations (4.5) and (4.6) as follows:

$$\begin{pmatrix} P_1 \\ P_2 \\ P_3 \\ P_4 \end{pmatrix}_{\parallel} = (\epsilon_{m\parallel})^2 (\epsilon_{w\parallel}) (\epsilon_{Avg})^n (\epsilon_{Gf\parallel}) P_0 \begin{pmatrix} t_{72} \\ t_{86} \\ t_{84} \\ t_{75} \end{pmatrix}_{\parallel} \quad (4.7)$$

$$\begin{pmatrix} P_4 \\ P_5 \\ P_6 \\ P_7 \end{pmatrix}_{\perp} = (\epsilon_{m\perp})^2 (\epsilon_{w\perp}) (\epsilon_{Avg})^n (\epsilon_{Gf\perp}) P_0 \begin{pmatrix} t_{75} \\ t_{84} \\ t_{86} \\ t_{72} \end{pmatrix}_{\perp} \quad (4.8)$$

Where the left matrices in both equations represent the PMT of parallel and perpendicular arrays respectively. The t terms in both matrices on the right side of the above equations denote the parallel and the perpendicular transmission coefficients of such prisms-lenses. Also note the mirror pattern of the prisms in this configuration.

The major loss of power then occurs at the arrays of prisms-lenses for a significant reason. The ruled gratings diffract the polarized beams illuminating the whole domain (350nm to 650nm) including the prisms-lenses as well as the gaps between them. Consequently, some of the wavelengths will be missed and cannot be detected by the PTMs arrays located after the prisms-lenses arrays (see Figure 4.25).

4.4 PMTS Testing and Calibrations

PMTs have efficiencies varying by as much as 20%, because the photocathode layer is several atoms thick, and manufacturing variations exist. The counting rate of a PMT as

a function of voltage shows a “plateau”, or flat region, between regions of steep rises. It is customary to operate the PMT at the plateau mid-point. The first round of tests involved the determination of the plateaus of our PMTs. The electronic setup consisting of a crate containing amplifiers, signal discriminators, and visual scalars was shown in Figure 3.38.

It can be obviously noted that all signal cables taken from the PMTs were wrapped with tin foil to reduce undesirable noise. Additionally, a large dark Faraday cage (black wooden box being wrapped with tin foil) was built to contain all PMTs and a light diffuser, which could be illuminated by ambient light, a laser or Mercury lamp from the outside, or not illuminated for dark noise measurements as shown in the Figure 4.14. The distance between the light diffuser and the PMTs was about ten feet, and the PMT array was about $5 \times 5 \text{ in}^2$, so that all PMTs were illuminated by the same light intensity to high accuracy.



Figure 4.14: Wood Prototype Detector Built in 2010

There are three variables in this test: the voltage supplied to the PMTs, the signal amplification, and the discrimination of threshold. The latter two are related as a doubling of the amplification and doubling of the threshold produces the same counting rate.

Data were taken over a period of ten seconds, and the amplification gain was held fixed at 10. After recording dark noise for each PMT, a small pin hole was made to allow ambient light to get through and strike a frosted piece of glass facing the PMTs. The uniformity of the light diffused by the frosted glass was tested by moving the PMT array by amounts exceeding the size of the array. Then, the high voltage power supply was changed at decrement of -50V from -1100V to -1450V. Counts were recorded and plotted at different threshold voltages from 20mV to 40mV with an increment of 5mV after each recording as shown in Figure 4.1.

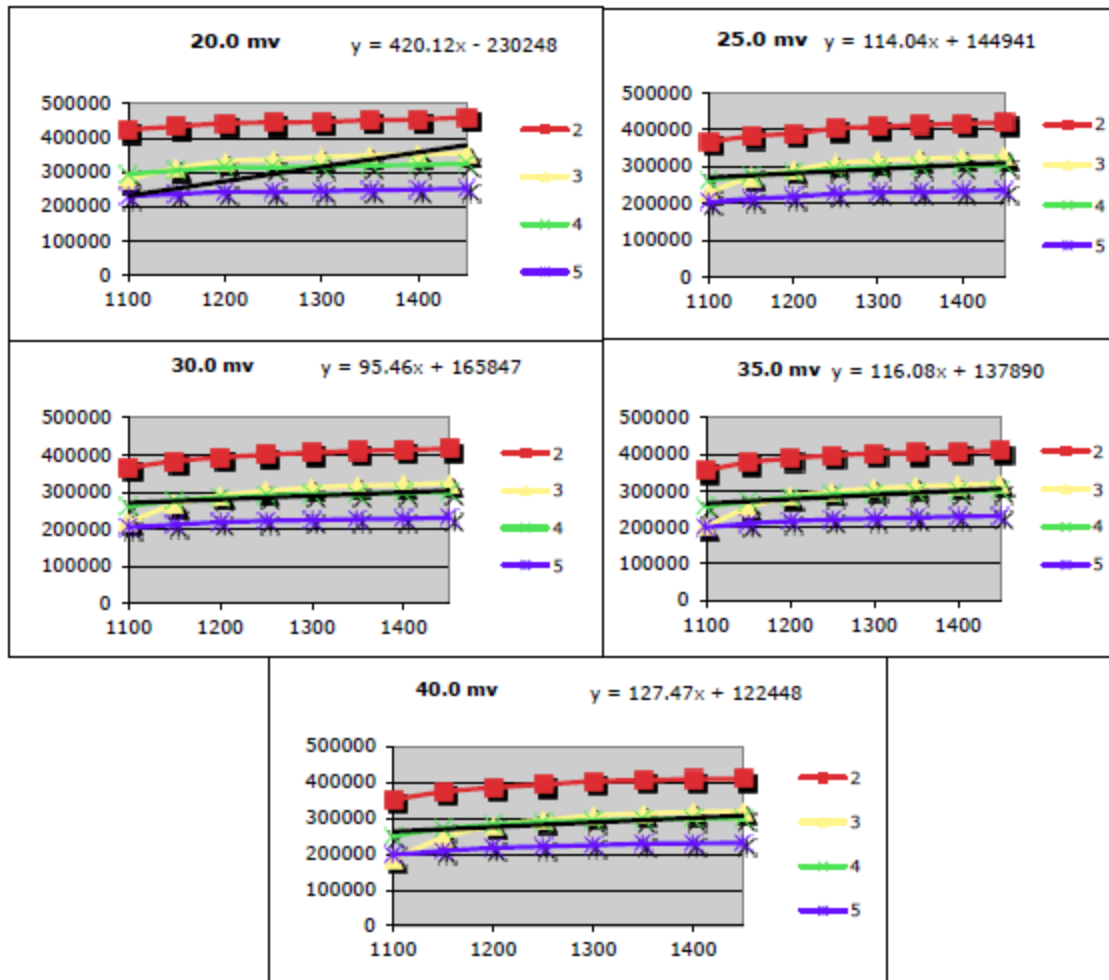


Figure 4.15: PMTs Counts at Different High Voltages and Different Thresholds

From the graphs, 30mV is the best threshold selection because it corresponds to the smallest inclination (slope = 95.46) of the best fit line. Additionally, it is evident that -1350 V is in the flat part of the curve for all PMTs. It was decided that all PMTs would operate at -1350 V, which is also a safe voltage as the PMTs are rated -1500 V only. The choice of one threshold and one voltage also simplifies the electronics and HV distribution system.

The relative efficiency of each PMT can be derived immediately from Figure 4.15, where a 20% relative efficiency variation is visible. However, it was found that the relative efficiencies of PMTs depend on the counting rate. This is normal, the PMTs are connected to a voltage divider in the PMT socket with overall resistance of tens of $M\Omega$. The overall RC of the circuit is significant and also varies significantly. Because PMTs and sockets will be mixed during shipment and assembly in Japan, it was decided that relative efficiency calibration would happen only at KEK with assembled detectors.

The spectral sensitivity of each photomultiplier tube was determined. This was done by selecting 30mV, -1350V high voltage, and using different filters ($340 \pm 26\text{nm}$, $482 \pm 35\text{nm}$, and $562 \pm 40\text{nm}$) to allow these specific wavelengths to get through the hole and eventually seen by PMTs.

The wavelength dependent plateaus are shown in Figure 4.16. It can be concluded that all PMTs have the same spectral response. It was decided that spectral differences between PMTs would be neglected as a source of error. This experiment confirmed tests of a similar apparatus at CESR.

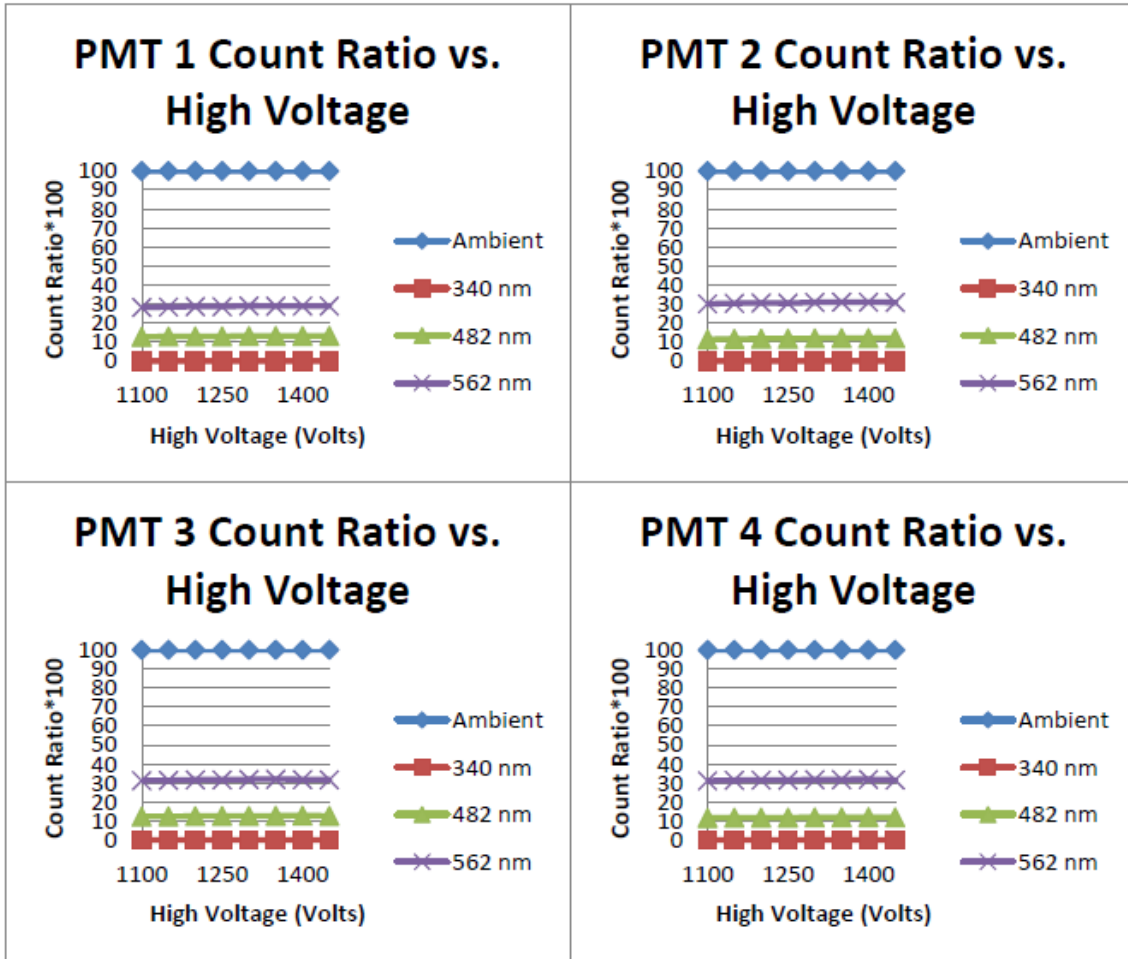


Figure 4.16: Spectral Responses of Four Different PMTs vs. High Voltage

4.5 Conveyor belt tests and controls:

As mentioned in chapter III, the conveyor belt was designed to swap photomultipliers, and it can be driven by a controller that listens to a PC's serial port. The conveyor belt carries 16PMTs, eight on either side. Therefore, the driver can be programmed with a maximum of 14 programs. Twelve programs were required to place a PMT at places of all other sixteen's with almost 120 measurements in total as presented in Table 18. These programs played a big role in calibrating and characterizing all PMTs due to the substantial amount of data that can be obtained.

Program 1UP (1) VS=100 (2) VR=6000 (3) DIS=-8000 (4) MA (5) END	2→1 Measures 12 PMTs	Program 3UP (1) VS=100 (2) VR=6000 (3) DIS=-24000 (4) MA (5) END	4→1 Measures 8 PMTs	Program AD/CB (1) VS=100 (2) VR=6000 (3) DIS=-100000 (4) MA (5) END	1→9 Measures 16 PMTs
Program 1DWN (1) VS=100 (2) VR=6000 (3) DIS=8000 (4) MA (5) END	1→2 Measures 12 PMTs	Program 3DWN (1) VS=100 (2) VR=6000 (3) DIS=24000 (4) MA (5) END	1→4 Measures 8 PMTs	Program AB/DC (1) VS=100 (2) VR=6000 (3) DIS=-60000 (4) MA (5) END	1→13 Measures 8 PMTs
Program 2UP (1) VS=100 (2) VR=6000 (3) DIS=-16000 (4) MA (5) END	3→1 Measures 10 PMTs	Program AC/DB (1) VS=100 (2) VR=6000 (3) DIS=40000 (4) MA (5) END	1→5 Measures 8 PMTs	Program CD/BA (1) VS=100 (2) VR=6000 (3) DIS=60000 (4) MA (5) END	5→9 Measures 8 PMTs
Program 2DWN (1) VS=100 (2) VR=6000 (3) DIS=16000 (4) MA (5) END	1→3 Measures 10 PMTs	Program CA/BD (1) VS=100 (2) VR=6000 (3) DIS=-40000 (4) MA (5) END	5→1 Measures 8 PMTs	Program ZERO (1) VS=100 (2) VR=6000 (3) DIS=0 (4) MA (5) END	Any→0 Measures 16 PMTs

Table 14: Twelve Necessary Programs to Interchange PMTs Locations

In the first column, program 1UP is written to shift all PMTs on one side of the box one place up and the other ones on the other side one place down. In other words, 1UP moves the second PMT of the same array to the place of the first (2→1) allowing the user to take 12 measurements from both sides at once. However, 1DWN does exactly the opposite of 1UP and shift PMT number two down and replace it by PMT number one.

A couple of acronyms need to be explained: in the first line of each program where VS (starting velocity) is set to 100 is simply to rotate the stepper motor starting with a frequency of 100Hz. In the second line, however, VR = 6000 stands for operating speed which is in this case 6KHz. This can be changed as well to speed up or down the motor, but it was found the moderate speed that all PMTs can be moved by without having their cables entangled should be set at 6000Hz.

DIS in the third line stands for the absolute distance or the number of steps that the conveyor belt would move or rotate from with respect to the original position assumed to be at zero. For example, say in the previous run the driver was told to move $DIS = 2000$ and now the driver is told to move $DIS = 5000$. What happens is that the driver will rotate the motor by only $3000 = (5000 - 2000)$ steps.

The last two commands are MA and END, which directly follow the main code in the program, stand for master absolute operation and end of program, respectively. Other commands are as important as the discussed ones because they allow the user to change or edit a line without erasing or rewriting the whole program. For instance, the “edit” command followed by the program’s name allows editing the program. When editing is done, the user can save the program by typing “S” followed by “Y/N” (yes or no). Finally, the “run” command followed by the program’s name executes whatever code in the called program is written.

It is essential to mention that the 24V stepper motor comes with a driver that comes with an instruction manual. Fortunately, the pieces of codes and commands that can be commonly used to control the motor in case of the beamstrahlung detector are pretty straightforward. The commands that were tested are shown in Table 14.

In addition to the programs listed in the above table, a thirteenth program was added and intended to be used and edited whenever needed using the protocols mentioned above. With this extra program every single position can be mapped by just editing the program and adding to it the appropriate code.

4.6 Primary Elbow Control

The 12 volts stepper motors used in primary elbows are not complicated like those used for the conveyor belts. They are very compact and can be controlled through a serial port from a windows terminal. These small motors are very sensitive and therefore a

special technique of testing needed especially because these devices are controlling the primary mirrors that are directly looking inside the main beam pipe.

Thus, to test a stepper motor, a very long path light had to be taken into considerations; a distance of 100 feet was sufficient. A laser source was shining the mirror inside through the center of one of the two inch tubes connected to primary elbow. Then, a graphing piece of paper was placed at 100feet across from the elbow so that the laser source was hitting the center of the grid. Finally, different protocol commands were sent to stepper motors in order to determine the algorithm to which the primary mirror is correlated.

It was found that as a motor rotates clockwise or counterclockwise 360degrees, it pushes inward or outward the mounting surface by 0.015in. It was also noticed that to tilt the mirror a degree in either direction, a 1000-step command needs to be sent to the corresponding motor. A command like `"/1A1000R"`, for example, rotates the motor addressed "1" by 1000steps. The "R" letter though stands for "run" and is used to execute the code, and it should be used in after each code.

The code above can be used to drive the motor in the clockwise direction. To drive it in the opposite direction which can be done unlike the 24V ones, polarity needs to be changed and then the same code can be executed. As an example, `"/1F0R"` sets the polarity of the motor addressed "1" default and `"/1F1R"` to flip polarity.

4.7 Wiring

After all motors tests, it is still good to recall that all small motors can be daisy chained together since they receive their signals from the same serial port. Of course, all

motors have to have addresses different from each other otherwise they receive the same command.

Unlike small motors, the 24V motors cannot be connected to the same serial port because both drivers are set to the same address. Otherwise, a digital multiplexer or a selector should be used to send the control commands to the corresponding motors.

4.8 Electronics Cards

There are two electronic cards one for each box and are intended to be replacing all outside old electronics including the huge crate, eight channels discriminators, and amplifiers. These cards were not tested at Wayne State University, but they were tested at Mexican institutions that made these boards and are part of the Belle II collaboration.

4.9 Aligning Manual Elbows and Mirrors Adjustments

In the Optical Channel of a top (bottom) view port there are four (six) manual elbows and one motorized elbow used to guide light from the beam pipe down to the Optics Box resulting in an overall number of five (seven) reflections. There are two ways to connect an elbow, shown in Figure 4.17.

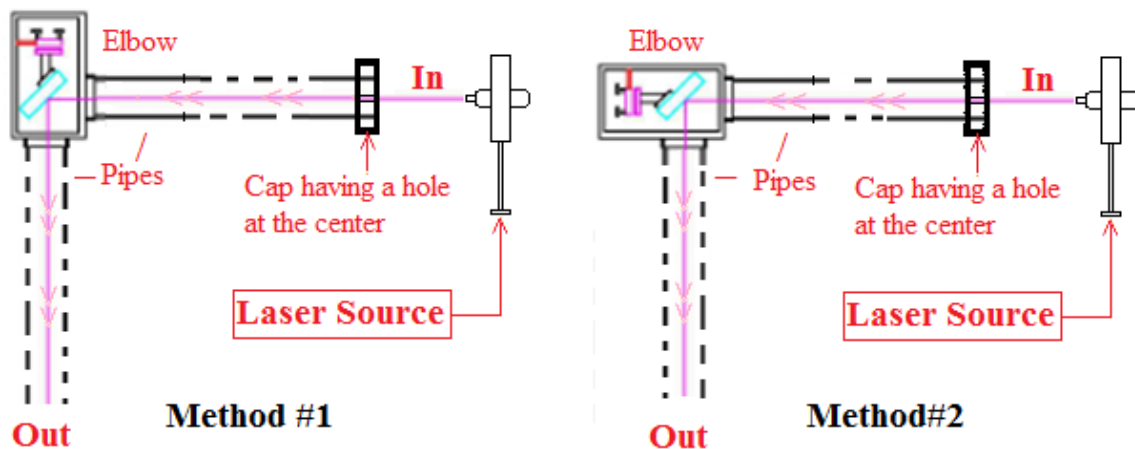


Figure 4.17: Two Ways of Connecting Pipes and Elbows in an Optical Channel.

The difference is that in the second method (Fig. 4.17, right), the laser beam illuminates the controlling back panel. During final testing, it was found that it is simple and efficient to center the laser visually, with the mirror removed (Figure 4.18).

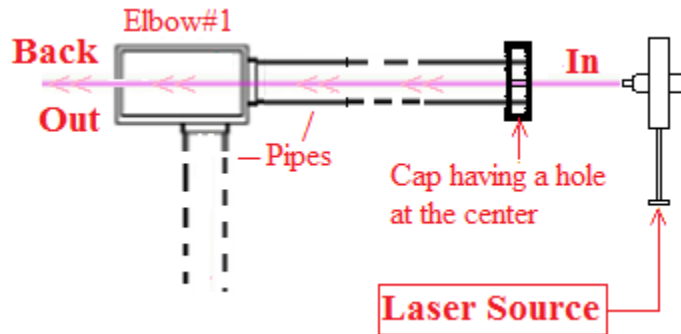


Figure 4.18: Laser Alignment Intermediate Step.

Then the mirror is reinstalled and oriented so that the laser beam strikes the next mirror in the center (Figure 4.19). This simple protocol allows fast, easy and accurate alignment of the Channel, a must for a device which will be disassembled several times in the course of its lifetime. This protocol is not possible if the laser beam cannot be visually located.

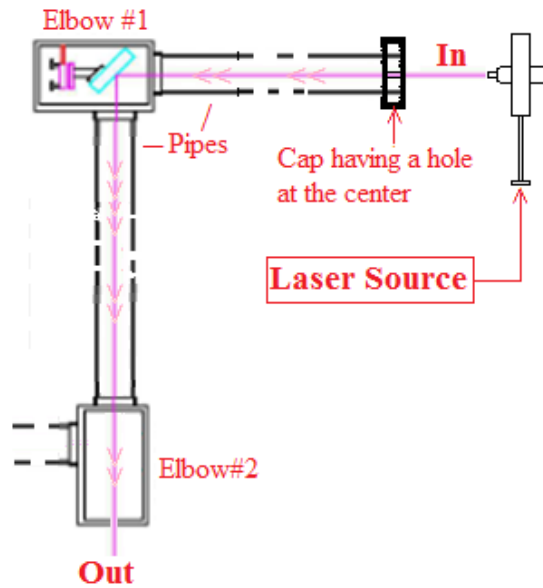


Figure 4.19: Next Step in Alignment Procedure.

4.10 Wollaston Prism alignment

When light reaches the Wollaston Prism, it gets split into two linear polarizations as explained before. The Wollaston prism splits light in its reference frame according to its orientation angle, which is a potential source of error.

Aligning the prism can be done by using a plumb line. Knowing that the center of the Wollaston prism is about 3.25" from the optical bench, a plumb line can be placed at the same distance while the Optics Box is level. Now the Wollaston prism can be rotated or adjusted so that the two beams of light hit the plumb line at two different spots in the vertical plane as shown Figure 4.20.

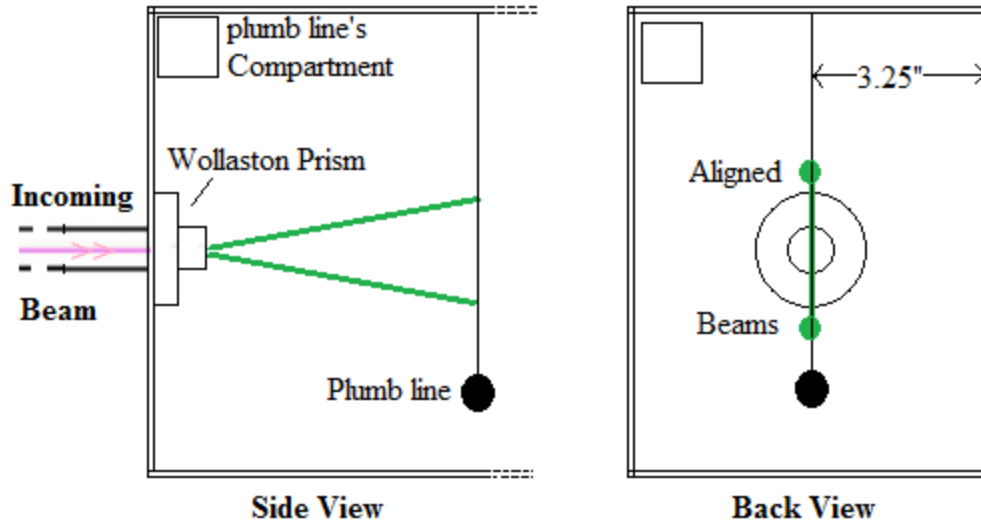


Figure 4.20: Two Views of a Plumb Line Used to Align a Wollaston

The whole path was also tested against other different light sources including red and green and spots of light were obtained on the Wollaston prism as shown in Figure 4.21.

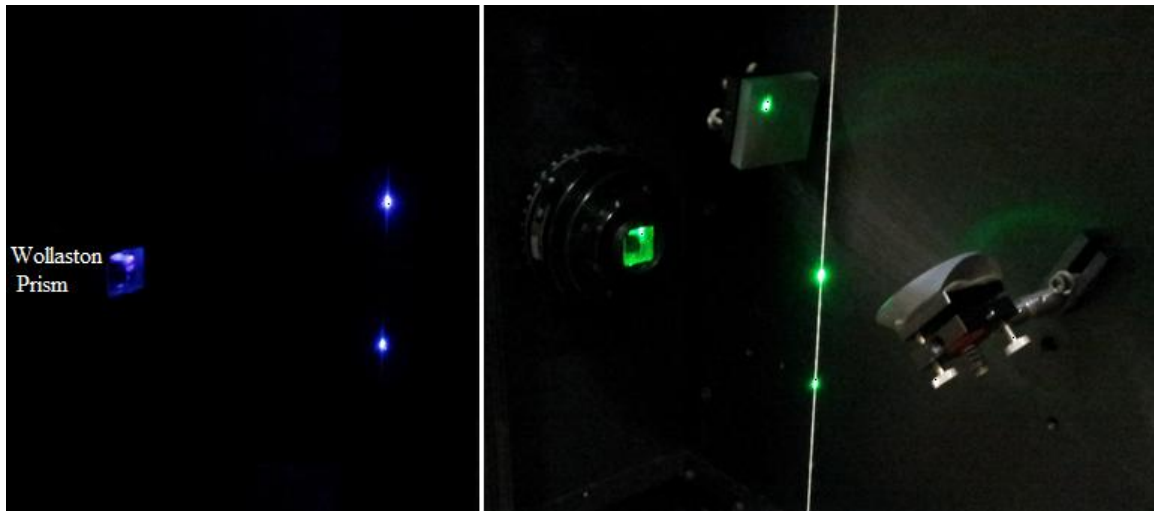


Figure 4.21: Left: Purple Laser Spots on a Plumb Line inside the Optics Box. Right: Green Laser Spots on a Plumb Line inside the Optics Box.

Getting the prism aligned is the first priority. The resulting split laser beams are then used to align everything else inside the Optics Box.

4.11 Polarization Tests

These tests are done for the purpose of determining the transmission efficiency of the prism. In Fig. 4.2, it was noted that the raw polarization of the green laser is complex. Using the technique of combining sources (explained in the next section) imposes both outputs to be differently polarized which caused the unlikely polarized beams to get split into one ordinary and another extraordinary as they reach the Wollaston and shown in Figure 4.22.

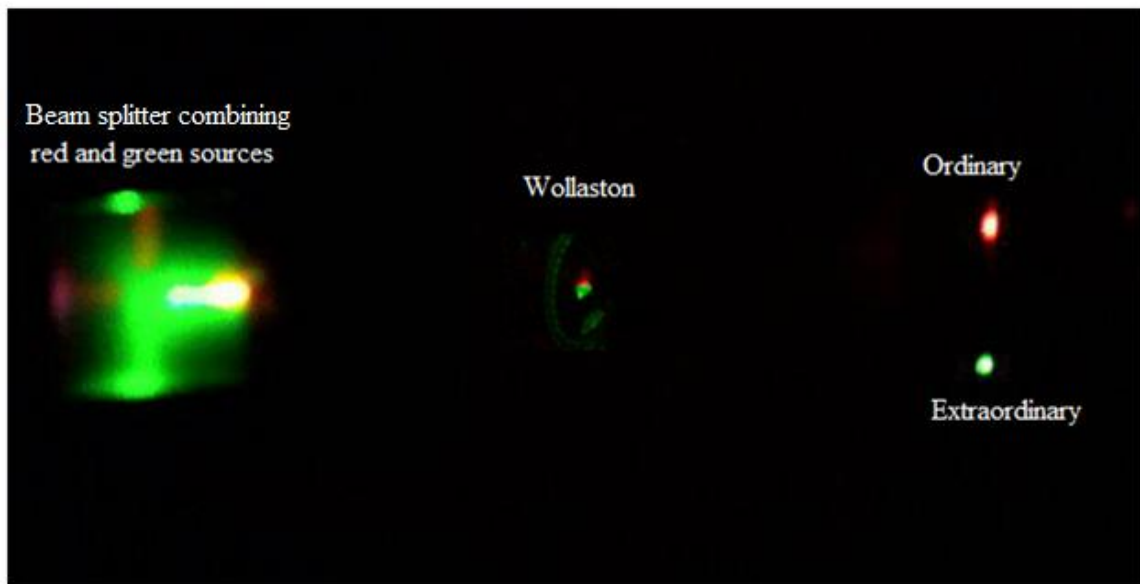


Figure 4.22: Green-Red Different Polarized Incoming Beams Striking a Wollaston

From the picture, it can be inferred that the red beam was ordinary or horizontally polarized, and the green beam was vertically or extraordinary polarized; otherwise, one would observe two green-red spot with a small separation in between on each side (see next section).

4.12 Mirrors and Grating Alignments

In previous parts, a monochromatic laser source of purple light was used to make all necessary alignments. In this part and because gratings diffract light according to its wavelengths, a combination of three different laser sources of light (red, green, and purple) was used. Another reason for choosing such a combination is to obtain something similar or close to “white-like” light so that after diffraction on the grating the different spots of different colors should hit the intended places of the prisms-lenses arrays.

The technique of combining colors not only allowed in aligning elements, but also in the investigation of placing all mirrors and gratings inside the box according to numbers obtained by computer programs. The question is how could lasers get combined and how precise is this?

The “white-like” laser can be then obtained by combining three different laser sources with the aid of two beam splitters. First, one of the lasers, say the green, must be aligned using the techniques explained in an early section in this chapter so that light gets to the Wollaston prism. Then, two identical beam splitters, placed close to one another, intercept the green light without preventing light from reaching the Wollaston prism. Using a polarized source in this case cannot work because it will be dead as soon as it hits the second beam splitter.

Note that in the case of non polarized sources, one would obtain two reflected parts of green through both prisms with 90° each with the respect to the transmitted part. Now, a red laser source can be added so that its rays strike the first splitter. Finally, a purple source can be added such that it shines up the second splitter. Necessary alignments and

fine adjustments are required to make all emerging lights on top of each other and thus a “white-like” source was generated as shown in Figure 4.23.

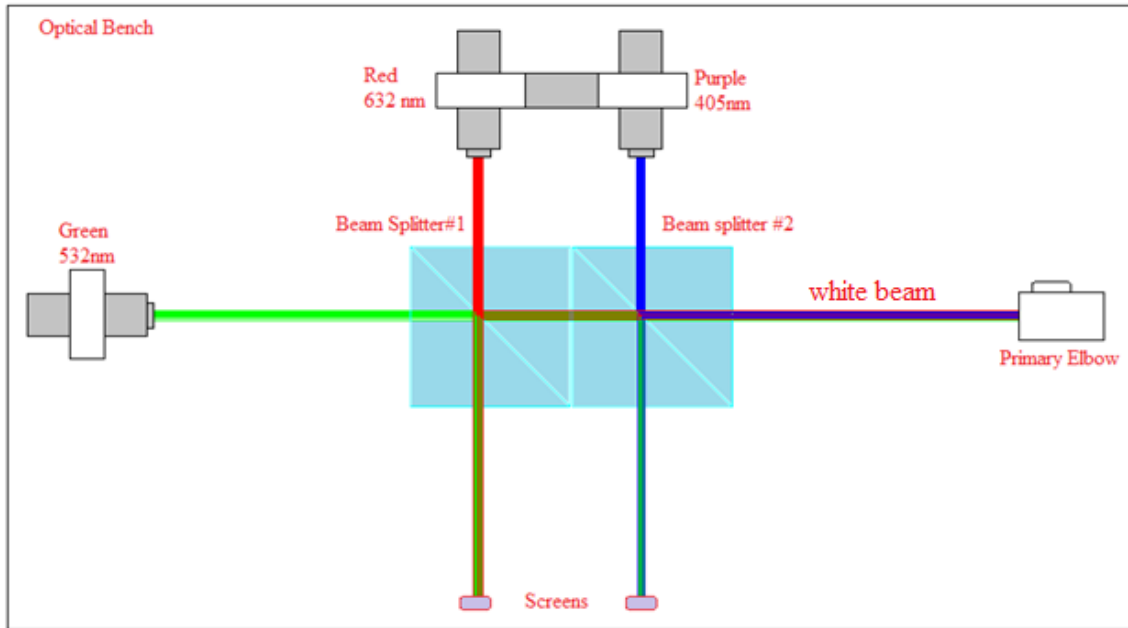


Figure 4.23: Combination of Three Different Sources Schematic

The phenomenon of obtaining a white source may seem to be straightforward, but in fact it is experimentally complicated. Complications start when you try to get three dots of different profiles on top of each, but it is still achievable. Once it is obtained, light gets to the Wollaston prism which splits it into two beams. The Wollaston now separates out the lights from each other by a small amount according to their wavelengths according to Table 7 and as shown in Figure 4.24.

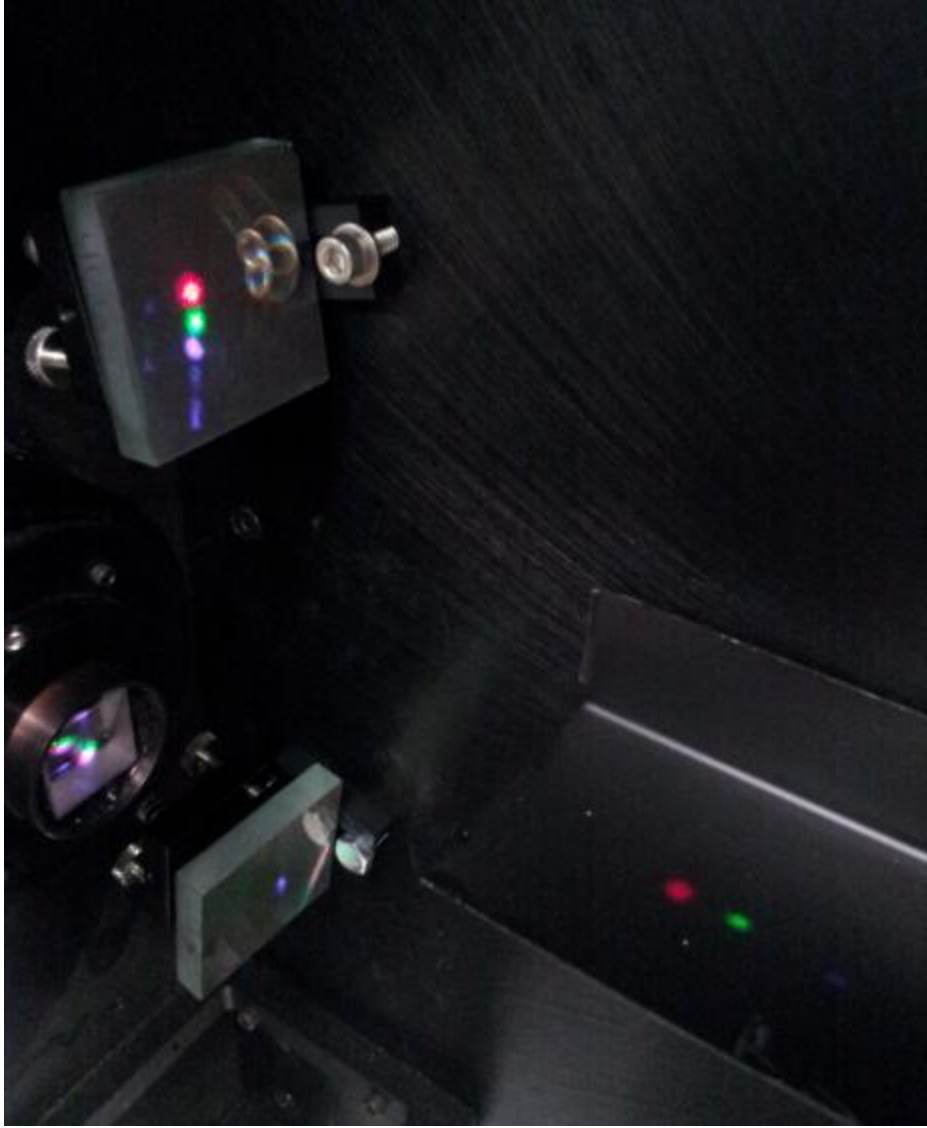


Figure 4.24: White-Like Laser's Separation through the Wollaston

It should be noted from the picture that a Wollaston prism splits light differently according to their wavelength where one would observe three different dots (purple, green, and red). Moreover, from the picture one can see that there is a partition between the two parts of the box where the 0th order peaks hit from both sides to prevent light from crossing from one side to another as shown in the picture.

This technique of separating colors not only helped in proving theoretical results, but also in aligning all reflecting mirrors and gratings that are inside the optics box. Tweaking a couple of screws and making sure that only 1st order peaks of each diffracted light are hitting the appropriate positions as shown in Figure 4.25 are met.

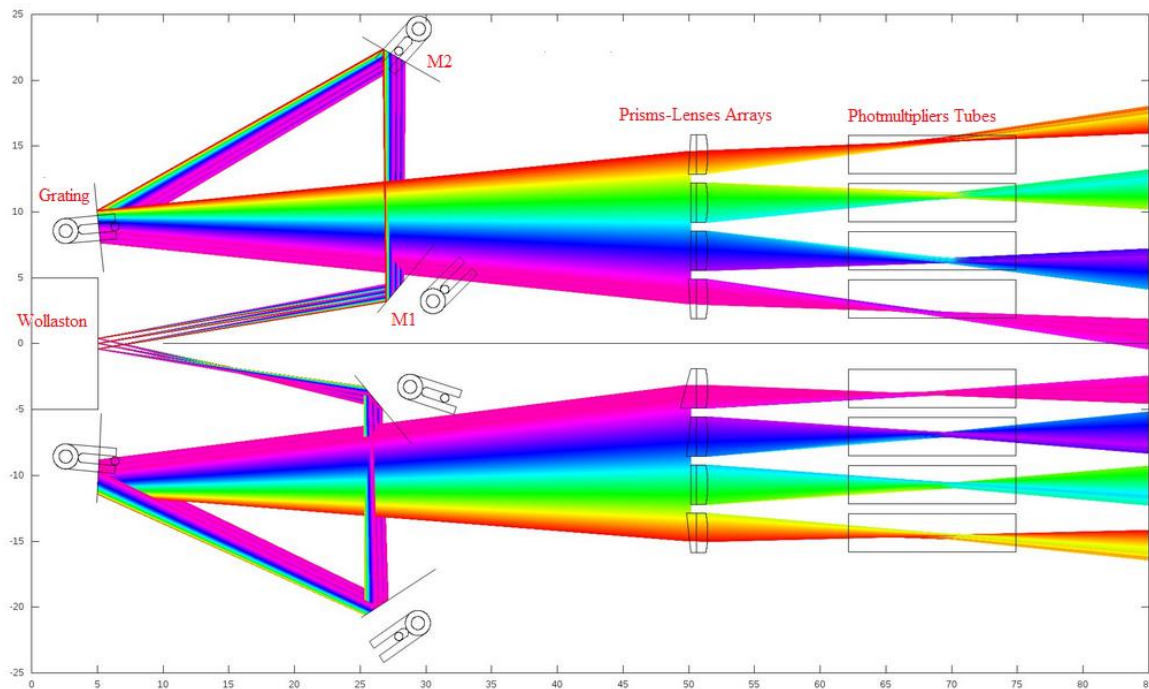


Figure 4.25: Simulated Optimized Positions and Angles Orientations of Multiple Elements of Optics Box.

Alternatively, a very intense strong white light source was used outside the box and located at the same line of sight with the Wollaston prism. Two square spots of light were observed on the gratings and rainbows were obtained on the prisms-lenses arrays of both sides. With this being done, the PMTs were removed and a screen (plain paper) was placed behind the arrays and located where the optimized location of the center of each PMT is. This was done to double check alignment and whether the arrays are collecting lights at the expected locations or not.

Chapter 5 : Conclusion

Designing and building such a detector is as important as discovering new physics. The flux of the newly discovered particles can be then studied out of the cross section that is in turn related to luminosity. Therefore, to increase the particles production rate the luminosity needs to be increased as well. This consists of beams diagnostics followed by a correct beam focusing in order to achieve a perfect collision. The beams diagnostics can be achieved by using the beamstrahlung technique. This detector collects data from the spectral decompositions of many different view ports, allowing us to compare them against each other and to match what is obtained to what was calculated or computed.

What was achieved in this research was that two large angle beamstrahlung boxes were produced and completely tested for validation. They are now ready to be shipped and installed for a real data collection at the SuperKEKB which will run for the first time in 2015.

REFERENCES

- [1] N. Cabibbo, *Physical Review Letters* 10 (12): 531533 1963
- [2] S. L. Glashow, *Nucl. Phys.* 22:579, 1961
- [3] S. Weinberg, *Phys. Rev. Lett.* , 19: 1264, 1967
- [4] A. Salam, *Elementary Particle Theory*, N. Svartholm, ed., Stockholm: Almqvist and Wiksell, 1968
- [5] D.J. Gross, F.Wilczek, *Phys. Rev. Lett*, 30:1343, 1973
- [6] H.D. Politzer, *Phys. Rev. Lett*, 30:1346 1973
- [7] M. Kobayashi and T. Maskawa, *Progr. Theor, Phys.*, 49: 652-657, 1973
- [8] L. Wolfenstein. *Physical Review Letters* 51(21): 1945, 1983.
- [9] C. Amsler *et al.*; Doser, M.; Antonelli, M., *Physics Letter B*, 667: 1-1340, 2008.
- [10] J. Beringer *et al.*; Arguin, J.-F.; Barnett, R.M., *Physical Review D* 80(1): 1-1526[162] 2012.
- [11] S.Y.Lee, Accelerator Physics, 3rd ed. (Word Scientific, New Jersey, 2012).
- [12] R. Coisson, *Phys. Rev. A* 20, 524, 1979.
- [13] G. Bonvicini, D. Cinabro, E. Luckwald, *Physical Review E* 59, 4584, 1999.
- [14] J.D. Jackson, Classical Electrodynamics, 2nd ed. (Wiley, New York, 1975).

ABSTRACT**USING LARGE-ANGLE BEAMSTRAHLUNG TO DETECT AND DIAGNOSE
POORLY COLLIDING BEAMS FOR LUMINOSITY OPTIMIZATION**

by

HUSSEIN A. FARHAT**August 2014****Advisor:** Dr. Giovanni Bonvicini**Major:** Physics**Degree:** Doctor of Philosophy

The large-angle-beamstrahlung is a very effective technique that can be used to monitor two crossing beams. Monitoring the beams helps in analyzing and studying the beams profiles allowing beams adjustments and eventually leading to a perfect beams collision. The perfect beam collision results in a higher luminosity; as a result, a high particles production rate and new physics can be discovered.

AUTOBIOGRAPHICAL STATEMENT

Name: Hussein A. Farhat

I was born in Tyre, Lebanon on March 20th of 1977. I received my Bachelor Degree of Education majoring in General Physics from the Lebanese University, Faculty of Science, First Branch in August 2002. I came to the United States of America in July 2007 as a Green Card holder. I entered the graduate program at Wayne State University in September 2009. I had the honor of joining the High Energy Physics group under Professor Giovanni Bonvicini's supervision in May 2010. I received my Masters of Science in Physics in May 2012 while continuing my research. During this time, I received the US Citizenship in October 2012.